Vibrational and Rotational Energy Relaxation in Liquids

Petersen, Jakob

Publication date:
2012

Document Version
Publisher's PDF, also known as Version of record

Vibrational and Rotational Energy Relaxation in Liquids

Jakob Petersen

Preface

This thesis has been submitted to the Department of Chemistry at the Technical University of Denmark in partial fulfillment of the requirements to obtain the PhD degree. The work presented here was carried out in the period from March 2009 to May 2012 under the joint supervision of Klaus B. Møller and Niels E. Henriksen. The thesis presents the computational methods used in the various studies and the obtained results, which are reported in summarized form in four papers of which one is accepted and two are to be submitted for publication in peer reviewed journals, and one is in preparation:

1. **J. Petersen**, N. E. Henriksen, K. B. Møller, *Validity of the Bersohn-Zewail Model beyond Justification*, Accepted for publication in Chem. Phys. Lett. (2012)
   http://dx.doi.org/10.1016/j.cplett.2012.05.022
2. J. H. Lee, M. Wulff, S. Bratos, **J. Petersen**, L. Guerin, J.-C. Leicknam, Q. Kong, J. Kim, K. B. Møller, H. Ihee, *Filming the Birth and Vibrational Relaxation of a Molecule in Solution with X-rays*, To be submitted to Science
   http://dl.dropbox.com/u/38111126/i2ccl4.pdf
3. **J. Petersen**, K. B. Møller, R. Rey, J. T. Hynes, *Ultrafast Librational Relaxation of H_2O in Liquid Water*, To be submitted to Phys. Chem. Chem. Phys.
   http://dl.dropbox.com/u/38111126/h2o.pdf
4. **J. Petersen**, K. B. Møller, R. Rey, J. T. Hynes, *Rotational Relaxation in Liquids: Polar versus Nonpolar Liquids*, In Preparation

Acknowledgements

First of all I would like to thank my supervisors Klaus B. Møller and Niels E. Henriksen for giving me the opportunity to carry out a PhD project at the Department of Chemistry and for helping me in advancing my academic skills. In the winter of 2010–2011 I had the pleasure of visiting Rossend Rey, Universitat Politécnica de Catalunya. During my stay in Barcelona the studies of rotational relaxation in liquids were initiated in joint collaboration with James (Casey) T. Hynes, University of Colorado, Boulder. I gratefully acknowledge the intensive and enlightening collaboration with Rossend and Casey. Several international collaborators have been involved in the project on vibrational relaxation of I_2 in CCl_4, and I would like to thank all of them. The Danish National Research Foundation and the Niels Bohr Foundation are gratefully acknowledged for financial support. Last but not least I would like to thank my office mates Thomas Kuhlman and Asmus Dohn for their exceptionally thorough proofreadings of the thesis.

Jakob Petersen

May 31, 2012

Abstract

Vibrational and rotational energy relaxation in liquids are studied by means of computer simulations. As a precursor for studying vibrational energy relaxation of a solute molecule subsequent to the formation of a chemical bond, the validity of the classical Bersohn-Zewail model for describing the intramolecular dynamics during photodissociation is investigated. The apparent agreement with quantum mechanical calculations is shown to be in contrast to the applicability of the individual approximations used in deriving the model from a quantum mechanical treatment. In the spirit of the Bersohn-Zewail model, the vibrational energy relaxation of I_2 subsequent to photodissociation and recombination in CCl_4 is studied using classical Molecular Dynamics simulations. The vibrational relaxation times and the time-dependent I-I pair distribution function are compared to new experimental results, and a qualitative agreement is found in both cases. Furthermore, the rotational energy relaxation of H_2O in liquid water is studied via simulations and a power-and-work analysis. The mechanism of the energy transfer from the rotationally excited H_2O molecule to its water neighbors is elucidated, i.e. the energy-accepting degrees of freedom of the surrounding solvent water molecules are identified.

Resumé

Vibrationel og rotationel afkøling i væsker studeres med computer simuleringer. Som optakt til at studere vibrationel afkøling af et opløst molekyle efter dannelsen af en kemisk binding undersøges gyldigheden af Bersohn-Zewail modellen, som beskriver den intramolekylære dynamik i fotodissociation ved brug af klassisk mekanik. Den gode overenstemmelse med kvantemekaniske beregninger vises at være overraskende set i lyset af anvendeligheden af de individuelle tilnærmelser, som indgår i udledningen af modellen udfra en kvantemekanisk beskrivelse. I tråd med Bersohn-Zewail modellen er fotodissociationen, rekombinationen og den vibrationelle afkøling af I_2 opløst i CCl_4 studeret med klassiske molekylær-dynamiske simuleringer. De vibrationelle afkølingstider og den tidsafhængige I-I parfordelingsfunktion er sammenlignet med nye eksperimentelle resultater, og i begge tilfælde er en kvalitativ overenstemmelse fundet. Endvidere er den rotationelle afkøling af H_2O i flydende vand studeret via simuleringer og en effekt-og-arbejdsanalyse. Mekanismen for energioverførelsen fra det rotationseksiterede H_2O-molekyle til nabo-molekylerne er belyst, dvs. de frihedsgrader som modtager energien i de omkringliggende vandmolekyle er identificeret.

Contents

Chapter 1

Introduction

In a typical chemical reaction some kind of energy redistribution will take place between the various degrees of freedom of the system. In particular, when a chemical bond is formed in a molecule, a transfer of excess energy out of the molecule's vibrational mode associated with the newly formed bond often follows.[1, 2] The excess vibrational energy can flow to the coupled vibrational and rotational degrees of freedom of the molecule, which is the case for low-pressure gases, where the vibrational energy redistribution can be assumed to be collisionless.[3–6] In solutions the description of the vibrational energy redistribution becomes more complex due to the many-body effects present in a dense fluid, i.e. the nonequilibrium vibrational energy distribution for a solute molecule, in which a chemical bond is formed, can decay to equilibrium by a transfer of energy to the various degrees of freedom of the solvent — with a possible energy flow 'through' the solute's rotational degrees of freedom.[7–9] In this case the vibrational energy redistribution is referred to as *vibrational and rotational energy relaxation*, i.e. a dissipative process that dampens the intramolecular motion of the solute molecule by transferring excess energy to the surrounding solvent. Hence, vibrational and rotational energy relaxation is intimately related to rates and mechanisms of chemical reactions in liquids, and a detailed microscopic description of relaxation processes is key to increase the current understanding of molecular reaction dynamics in condensed phases.[10–15]

For decades, energy relaxation in liquids has been investigated intensively both experimentally as well as theoretically.[16–18] Due to continued experimental developments in time-resolved optical spectroscopy and x-ray diffraction, it is possible to carry out real-time measurements of relaxation processes, for which the characteristic time scales are often ultrafast, i.e. in the femto- or picosecond time domain.[19–23] On the theoretical side, the choice of description has moved from purely analytical calculations to more realistic modeling of interactions and dynamics in the liquid phase.[10, 14] In computer simulations an atomistic description of the system is possible, which permits serious testing of theoretical models and the approximations that are introduced in the interpretation of experimental results.[24–29] Although a lot of effort has been put into the studies of vibrational and rotational energy relaxation in liquids, several important questions still remain unanswered in a complete form, e.g.: Which theoretical models are appropriate? What is the rate and mechanism of relaxation? To which solvent modes is the energy transferred?[30]

The overall topic of this thesis is the observation of chemical dynamics associated with vibrational and rotational energy relaxation in liquids, and we try to answer the questions above for some specific chemical systems. We use computer simulations to follow and observe the time evolution of the relaxation processes, and we focus on simple systems: A diatomic molecule in a nonpolar solvent and pure water. In this way the computational cost is kept relatively low and the complexity of the system does not obscure the microscopic level of understanding.

1.1 The Computational Approach

When we study the dynamics of a chemical reaction, we are interested in the time evolution of a molecular system, which is governed by the laws of quantum mechanics. It is well-known that a full quantum mechanical treatment of a many-body system, e.g. a liquid, is computationally expensive, and some approximations often have to be introduced in the theoretical framework. For several decades, classical Molecular Dynamics (MD) simulations have been used for computer experiments on liquids, where the equations of motion are classical, and the interactions are described by molecular mechanics force fields.[31] The dynamical behaviour of a system obtained from classical MD simulations will differ from that obtained employing quantum mechanics. Using classical MD simulations most dynamical, structural and thermodynamic properties of the system can be calculated in good agreement with experimental results, but quantum mechanical effects such as uncertainty in position/momentum and tunneling will be missing.[32] The obvious advantage of using classical MD simulations compared to quantum mechanics descriptions is the relatively low computation time and overall feasibility, and this is the main reason for choosing classical MD simulations as the primary computational approach in the work presented in this thesis.

In order to simulate the energy relaxation of a solute molecule subsequent to the formation of a chemical bond, we have to choose an *ad hoc* theoretical model to describe the process leading to the formation of the chemical bond. In conventional classical MD simulations of liquids, chemical bond breakage and formation are not included (recently, reactive force fields for some molecular systems have been developed, see e.g. [33]). One simple process, in which the formation of a chemical bond can take place in a liquid, is the recombination of photofragments due to 'caging' in a solvent shell subsequent to photodissociation of a solute molecule.[34–36] An exact theoretical description of the photodissociation of a molecule, where an electronic transition from a bonding to an antibonding state takes place due to the interaction with an ultrashort laser pulse, clearly relies on quantum mechanics. Bersohn and Zewail have proposed an approximate model for describing the nuclear dynamics, in terms of classical mechanics, of gas-phase molecules undergoing photodissociation in ultrafast pump-probe experiments.[37] This scheme has been successfully used in several computational studies of photodissociation in both gas- and liquid-phase, see e.g. [38–41]. The well-known approximations involved in deriving the classical Bersohn-Zewail (BZ) model from a quantum mechanics treatment of gas-phase photodissociation seem very reasonable [42], but the exact validity of these approximations has not been investigated in a rigorous fashion to the best of our knowledge. In this thesis we present a thorough numerical study of the validity of the approximations in the BZ model for the photodissociation of a gas-phase Br_2 molecule, and we find that the nuclear dynamics described by the BZ model is in very good agreement with quantum mechanics wave packet calculations in terms of the time-evolution of the expectation value of the nuclear position in the antibonding state. Although, this agreement is quite surprising in the light of the validity of the individual approximations.

1.2 Vibrational Energy Relaxation

After we have established that the BZ model is well suited for a classical description of photodissociation, we proceed to study the bond formation and vibrational energy relaxation following the photodissociation of a solute molecule by means of classical MD simulations. The solvent of choice is carbon tetrachloride, in which we simulate the photodissociation (in the spirit of the Bersohn-Zewail model), the subsequent recombination, and vibrational energy relaxation of an iodine molecule. This system is chosen partly because the solvent

is nonpolar and fairly easy to simulate, and furthermore, the solute diatomic molecule represents the limiting case of an 'isolated' vibrational mode with no opportunity for energy redistribution to other vibrational degrees of freedom of the solute molecule itself.[43] The reaction of iodine atoms to form molecular iodine in condensed phases is perhaps the most extensively studied example of radical recombination, and for decades, the system has served as a prototypical model for bimolecular reactions in solution.[14] Several experimental studies, using time-resolved optical spectroscopy and x-ray diffraction, of this reaction have provided new information about the 'caging' mechanism and the vibrational relaxation time in liquids [44–48] and in inert gas matrices [49–55]. Furthermore, the experimental results have been compared to computer simulations of the reaction.[19, 56–62] In particular for I_2 dissolved in CCl_4, the simulation results have been based on very poor statistics, and the photodissociation and recombination process have not been treated explicitly.[61, 62] Thus, further theoretical scrutinization of this reaction is justified.

We have participated in an international collaboration with experimental groups from France (Michael Wulff, ESRF) and Korea (Hyotcherl Ihee, KAIST), who have developed a so-called 'time-slicing' scheme to increase the time-resolution of x-ray diffraction experiments carried out at synchrotron facilities from the order of $\sim$ 100 ps to $\sim$ 1-10 ps. In order to determine the validity of the 'time-slicing' scheme, the vibrational energy relaxation of I_2 in CCl_4 has been chosen as the test system. We have compared the new experimental and simulation results, in terms of vibrational relaxation times and the time-dependent I-I pair distribution function, and a qualitative agreement is found. This agreement indicates that the novel 'time-slicing' scheme is capable of enhancing the time-resolution of x-ray diffraction experiments. Furthermore, we show that a good approximation to the simulated time-dependent I-I pair distribution function can be constructed from the time-dependent vibrational energy distribution such that experimental data from time-resolved x-ray diffraction and optical spectroscopy can be compared by using the same procedure. Finally, we observe some degree of coherent motion associated with the vibrational energy relaxation. Coherent motion has been observed for the photodissociation of iodine in inert gas matrices, but has been absent in liquids.[54, 55] This partial coherent motion might be observed in future time-resolved x-ray diffraction experiments using free electron lasers, for which a femtosecond time resolution can be obtained.[23, 63, 64]

1.3 Rotational Energy Relaxation

Since a solute molecule's vibrational modes couple to the rotational degrees of freedom of the solute itself, we are also interested in studying rotational energy relaxation. To this end, the system of choice is pure liquid water, which is the most common solvent in organic and biological chemistry. Librations (hindered rotations) of liquid water are important energy receptors for solute vibrational energy relaxation [65, 66], and for water stretch and bend vibrational excitations [29, 67–75]. Futhermore, librations are key participants in the rearrangements of the hydrogen bond networks of water and aqueous solutions.[76–80] Recently, the bend vibrational energy relaxation and the direct rotational energy relaxation of H_2O in liquid water have been monitored in real time using femtosecond two-color infrared spectroscopy.[81–83] Rey and Hynes have shown that the experimental relaxation times can be reproduced via classical MD simulations and that for a bend vibrational excited water molecule, 2/3 of the excitation energy is transferred to the rotational degrees of freedom of the molecule itself.[73]

Here we study the rotational energy relaxation of H_2O in liquid water subsequent to direct rotational excitation. This is of interest in connection to the study by Rey and Hynes [73], and in connection to the case of energy transfer from a vibrational excited solute molecule to the rotational degrees of freedom of a water solvent. We make use

of a recent reformulation [75] of a power and work analysis [65, 66], which leads to an identification of the energy-accepting degrees of freedom of the surrounding solvent water molecules and to which solvent waters the energy flows, hence, the locality of the relaxation process can be determined. Within the chosen force field model of the water system (the molecules are treated as rigid rotors), the rotational degrees of freedom of the surrounding solvent water molecules clearly dominates in the energy transfer, with a minor transfer to the translational degrees of freedom. We observe that the rotational energy relaxation is quite local, in the sense that the 1st and 2nd solvent shells primarily accept the excess energy directly from the rotationally excited molecule. Furthermore, we investigate whether the rotational energy relaxation is dependent on the excitation energy, temperature, and excitation method.

The outline of the remainder of this thesis is as follows. In chapter 2 we briefly present the various numerical algorithms used in the quantum mechanics wave packet calculations and the classical MD simulations and show some test-of-implementation results. The validity of the individual approximations in deriving the BZ model from a quantum mechanics treatment of photodissociation is discussed in chapter 3. The study of photodissociation, subsequent recombination, and vibrational energy relaxation of I_2 in CCl_4 is presented in chapter 4. In chapter 5 a thorough examination of the energy flow pattern for rotational energy relaxation subsequent to direct rotational excitation of H_2O in liquid water is presented. Finally, concluding remarks are offered in chapter 6.

Chapter 2

Computational Methods

In this chapter the computational methods used in the various studies are described. All calculations are carried out with in-house codes written by the author in either C/C++, FORTRAN, or MATLAB. In Sec. 2.1 a scheme for numerical propagation of a wave packet describing the nuclear dynamics of a diatomic molecule is presented, and in Sec. 2.2 the setup for classical Molecular Dynamics simulations of a liquid is discussed.

2.1 Nuclear Wave Packet Propagation

We want to investigate the photodissociation of a diatomic molecule in gas-phase, and we do this in a frame fixed to the internuclear axis. Therefore, the system becomes one-dimensional, where the independent variable is the internuclear distance r, and the natural starting point is the time-dependent radial Schrödinger equation

$$i\hbar\frac{\partial}{\partial t}\Psi(r,t) = \left(-\frac{\hbar^2}{2m}\frac{\partial^2}{\partial r^2} + \frac{\hbar^2 l(l+1)}{2mr^2} + V(r)\right)\Psi(r,t)\,, \tag{2.1}$$

where $\Psi(r,t)$ denotes the radial wave function, m is the reduced mass of the two-nuclei system, l is the angular momentum quantum number, and $V(r)$ denotes the potential energy surface associated with the electronic state in question. We simplify the treatment of the system to encompass only two adiabatic electronic states, which are part of the natural set of eigenstates of the electronic Schrödinger equation.[84] Furthermore, we make use of the Born-Oppenheimer approximation, in which the electronic states are uncoupled, i.e. population transfer between the states can only occur, when a perturbation $\hat{W}$ is applied to the system.[85]

2.1.1 Molecule-Field Interaction

For the photodissociation process the perturbation is an optical laser pulse, and the coupling term within the electric dipole approximation becomes

$$\hat{W}(r,t) = -\boldsymbol{\mu}(r)\cdot\boldsymbol{\epsilon}(t) = -\mu(r)\epsilon(t)\cos(\theta)\,, \tag{2.2}$$

where $\boldsymbol{\mu}(r)$ is the molecular transition dipole moment, $\boldsymbol{\epsilon}(t)$ is the electric field component of the laser pulse, and θ is the angle between them ($\boldsymbol{\epsilon}(t)$ is spatially independent, since the wavelength of the field greatly exceeds the molecular dimension).[86] For convenience, we employ the optimal molecule-field orientation that yields the maximum excitation, i.e. $\theta = 0$. The two coupled equations of motion then read

$$i\hbar\frac{\partial}{\partial t}\begin{bmatrix}\Psi_1(r,t)\\ \Psi_2(r,t)\end{bmatrix} = \begin{bmatrix}\hat{H}_1 & \hat{W}\\ \hat{W} & \hat{H}_2\end{bmatrix}\begin{bmatrix}\Psi_1(r,t)\\ \Psi_2(r,t)\end{bmatrix}, \tag{2.3}$$

where the Hamiltonian operators for each adiabatic state are given by

$$\begin{aligned}\hat{H}_1 &= -\frac{\hbar^2}{2m}\frac{\partial^2}{\partial r^2} + \frac{\hbar^2 l_1(l_1+1)}{2mr^2} + V_1(r) \\ \hat{H}_2 &= -\frac{\hbar^2}{2m}\frac{\partial^2}{\partial r^2} + \frac{\hbar^2 l_2(l_2+1)}{2mr^2} + V_2(r)\,.\end{aligned} \tag{2.4}$$

The shape of the electric field component of the laser pulse is described by a Gaussian envelope function

$$\epsilon(t) = \epsilon_0 \mathrm{e}^{-t^2/(2\tau^2)} \mathrm{e}^{-i\omega t}\,, \tag{2.5}$$

where ϵ_0 is the maximum amplitude, τ denotes the temporal duration of the laser pulse (FWHM$[\epsilon] = 2\tau\sqrt{2\ln 2}$), and ω represents the carrier frequency.

2.1.2 Grid Representation of Wave Functions

It is not possible to analytically solve the coupled set of equations of motion for arbitrary potentials. Therefore, we have to make use of a numerical scheme, and here we have chosen the Fourier transform method, in which the wave function is represented on a grid of $2N$ equidistant points.[87] In essence, a wave function $\Psi(r,t)$ is expanded in a finite basis set of $2N$ plane waves, such that for each grid point r_j

$$\Psi(r_j,t) = \sum_{k=-N+1}^{N} a_k(t) \mathrm{e}^{-i2\pi k r_j/L}\,, \tag{2.6}$$

where L is the length of the interval. The orthogonality of the plane waves leads to the expression for the expansion coefficients

$$a_k(t) = \frac{1}{2N}\sum_{j=1}^{2N} \Psi(r_j,t) \mathrm{e}^{i2\pi k r_j/L}\,, \tag{2.7}$$

which represent the amplitudes of the wave function in momentum space.[88] The expression in Eq. 2.7 is referred to as the discrete Fourier transform, which can be implemented with high efficiency using the FFT algorithm.[89] Thus, the wave function is given by a grid representation in position and momentum space, and the mapping between the two representations is carried out via the discrete Fourier transform.

2.1.3 Grid Representation of Operators

We have to consider how to evaluate the action of operators with a grid representation of the wave function. The most important operator is the Hamiltonian, which is essential to the time propagation of the system. The Hamiltonian operator is the sum of the kinetic energy operator $\hat{T}$ and the potential energy operator $\hat{V}$, where $\hat{V}$ is local in position space, i.e. the action of $\hat{V}$ on the wave function is the multiplication $V(r_j)\Psi(r_j,t)$. The kinetic energy operator $\hat{T}$ is 'global' in position space, i.e. a second order differential operator with respect to r, but becomes a local operator in momentum space, where $T(k) = \hbar^2 k^2/(2m)$.[90] Hence, the action of the Hamiltonian operator on the wave function is carried out in two steps. 1) The action of the potential energy operator: The wave function in position space is multiplied by $V(r_j)$. 2) The action of the kinetic energy operator: The wave function in position space is mapped to momentum space via the discrete Fourier transform, the expansion coefficients are multiplied by $T(k)$, and via the inverse discrete Fourier transform the wave function is mapped to position space.

2.1.4 Short Time Propagator

Now we turn to the problem of propagating the wave function in time. If the Hamiltonian operator is time-independent, then the operator which propagates the wave function from t_0 to t is $\hat{U}(t,t_0) = \exp(-i\hat{H}(t-t_0)/\hbar)$, see Ref. [91]. In our case, the Hamiltonian operator is effectively time-dependent due to the coupling term, see Eq. 2.3. However, if the time-dependence of the Hamiltonian operator is negligible over a short time interval δt the time propagator can be approximated by

$$\hat{U}(t,t_0) \approx \prod_{n=1}^{N} \mathrm{e}^{-i\hat{H}[t_0+(N-n)\delta t]\delta t/\hbar}\,,\ t = t_0 + N\delta t\,, \tag{2.8}$$

where an equally spaced grid in the time domain is applied. Each factor in Eq. 2.8 is referred to as a short time propagator. In the split-operator technique, the short time propagator is written as a symmetric product

$$\mathrm{e}^{-i\hat{H}\delta t/\hbar} \approx \mathrm{e}^{-i\hat{T}\delta t/(2\hbar)}\mathrm{e}^{-i\hat{V}\delta t/\hbar}\mathrm{e}^{-i\hat{T}\delta t/(2\hbar)}\,, \tag{2.9}$$

where the accuracy of the approximation is second order in time. The separation of the propagator in the split-operator technique preserves unitarity, hence, the norm of the wave function is strictly conserved.[92] The approximation of the short time propagator can be enhanced to any finite order in time, but the splitting in Eq. 2.9 leads to a very accurate propagation for time steps up to ~ 1 fs depending on the system.[93, 94]

2.1.5 Tests of Numerical Stability

In the following section we report some results from various tests of the numerical stability of the code for nuclear wave packet propagation. Here, a wave packet is defined as a superposition of stationary states corresponding to the vibrational levels of the potential in question. Therefore, a wave packet is nonstationary in general.

Vibrational Eigenvalues and Eigenfunctions

The first test is to run calculations with only one electronic state described by a Morse potential, where the eigenvalues $E_{\mathrm{M}}(n)$ of the corresponding vibrational levels read

$$E_{\mathrm{M}}(n) = \nu(n+1/2) - \frac{(2\pi\nu)^2(n+1/2)^2}{4D_{\mathrm{e}}}\,, \tag{2.10}$$

where ν is the frequency, D_{e} denotes the classical dissociation energy, and $n \in \mathbb{N}_0$.[95] The vibrational eigenvalues and eigenfunctions (stationary wave functions) of any potential can be found via relaxation of a trial function, i.e. propagation of a trial function in imaginary time.[96] The principle is very simple: We define an imaginary time coordinate $s = it$ and write the propagation of a trial function f as

$$f(s) = \mathrm{e}^{-\hat{H}s/\hbar}f(0) = \mathrm{e}^{-\hat{H}s/\hbar}\sum_n c_n\Phi_n = \sum_n c_n\mathrm{e}^{-E(n)s/\hbar}\Phi_n\,, \tag{2.11}$$

where $\hat{H}$ is the Hamiltonian operator associated with the electronic state in question, and $\{\Phi_n\}$ is the complete set of eigenfunctions (we consider only the discrete spectrum). Clearly, each term in the expansion will decrease exponentially in time, but with different rates depending on the eigenvalue $E(n)$. By renormalization of the trial function during the propagation in imaginary time, the ground vibrational state eigenfunction of the potential is the only 'surviving' term in the expansion. The 1st excited vibrational state

eigenfunction can be found by a similar procedure, where the ground vibrational state eigenfunction (with an appropriate weight) is subtracted from the trial function, and so on for higher order excited vibrational state eigenfunctions.

The eigenvalues of the Morse potential corresponding to the adiabatic ground electronic state of Br_2 (the parameters for the potential are given in Sec. 3.2.1) are found via the relaxation method and compared to the eigenvalues given in Eq. 2.10. A similar comparison is carried out for the eigenvalues of the harmonic potential corresponding to the 2nd order approximation of the Morse potential around the classical equilibrium distance. In Tab. 2.1 the first five eigenvalues of the Morse potential are shown, where E_{M} refers to the values given in Eq. 2.10 and $\tilde{E}_{\mathrm{M}}$ refers to the values calculated by relaxation of a trial function. Similarly for the harmonic potential, $E_{\mathrm{H}} = \nu(n + 1/2)$ and $\tilde{E}_{\mathrm{H}}$ refers to the values calculated by relaxation. Each set of eigenvalues $\{E_{\mathrm{M}}, \tilde{E}_{\mathrm{M}}\}$ or $\{E_{\mathrm{H}}, \tilde{E}_{\mathrm{H}}\}$ are identical, for a given n, within five decimal digits of precision.

Table 2.1: Eigenvalues of the Morse and harmonic potential

n	$E_{\mathrm{M}}/\mathrm{cm}^{-1}$	$\tilde{E}_{\mathrm{M}}/\mathrm{cm}^{-1}$	$E_{\mathrm{H}}/\mathrm{cm}^{-1}$	$\tilde{E}_{\mathrm{H}}/\mathrm{cm}^{-1}$
0	161.19	161.19	161.60	161.60
1	481.10	481.10	484.80	484.80
2	797.73	797.73	808.00	808.00
3	1111.1	1111.1	1131.2	1131.2
4	1421.1	1421.1	1454.4	1454.4

In Fig. 2.1 the Morse potential V_{M} and the harmonic potential V_{H} are shown together with the first five eigenfunctions Φ_n, $n = 0, 1, \ldots, 4$, for each potential. The eigenfunctions are plotted at the corresponding eigenvalues. Analytic expressions for the eigenfunctions of the harmonic potential are well-known, see Ref. [97]. We have compared these with the numerical calculations, and the agreement is perfect within the numerical precision.

Rabi Oscillations

The second test is performed on a two-state system with a sinusoidal oscillating coupling term, for which the two equations of motion read

$$i\hbar\frac{\partial}{\partial t}\begin{bmatrix}\Psi_1(r,t)\\ \Psi_2(r,t)\end{bmatrix} = \begin{bmatrix}E_1 & \zeta \mathrm{e}^{i\omega t}\\ \zeta \mathrm{e}^{-i\omega t} & E_2\end{bmatrix}\begin{bmatrix}\Psi_1(r,t)\\ \Psi_2(r,t)\end{bmatrix}, \tag{2.12}$$

where E_1 and E_2 are scalars representing the energies of each state, and ζ is the amplitude of the oscillating coupling. The two states are chosen as the ground vibrational states of two harmonic potentials with identical curvature and position of the minimum, but shifted in energy. In this case the equations of motion have an analytic solution, see Ref. [91]. It turns out that the probability $P_i(t) = \langle\Psi_i(t)|\Psi_i(t)\rangle$ of the system being found in one of the states $i = 1, 2$ is given by the expressions

$$P_1(t) = 1 - P_2(t) \quad \text{and} \quad P_2(t) = \sin^2(\zeta t/\hbar)\,, \tag{2.13}$$

if only state 1 is populated at $t = 0$, and ω corresponds to the resonance frequency, i.e. $\hbar\omega = E_2 - E_1$. Clearly, the fundamental period of the oscillations in the probabilities, often referred to as Rabi oscillations, is $T_{\mathrm{f}} = \pi\hbar/\zeta$, and with the chosen value of ζ we get

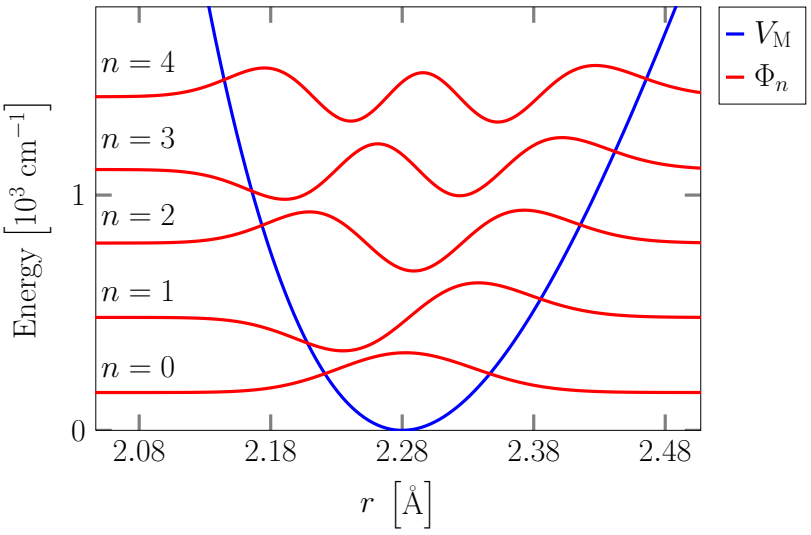

(a) Morse potential and first five eigenfunctions.

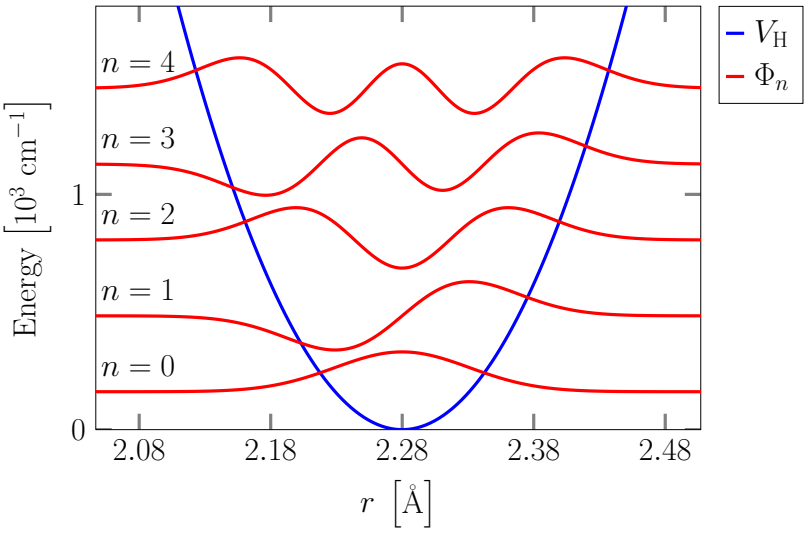

(b) Harmonic potential and first five eigenfunctions.

Figure 2.1: a) Morse potential V_{M} and the first five vibrational eigenfunctions Φ_n, $n = 0, 1, \ldots, 4$. The eigenfunctions are plotted at the corresponding eigenvalues. b) Harmonic potential V_{H} and the first five vibrational eigenfunctions Φ_n, $n = 0, 1, \ldots, 4$.

$T_{\mathrm{f}} = 226.54$ fs. Hence, the probability is completely removed from state 1 and transferred to state 2 in $T_{\mathrm{f}}/2$ and vice versa. In Fig. 2.2 the probability of the system being found in state 1 and state 2 as a function of time is shown for a propagation of 500 fs, and we see that the fundamental period is 226.54 fs as expected.

The code for nuclear wave packet propagation has also been used to reproduce various results reported in the literature, e.g. Tawari *et al.* [98], and several comparisons with similar codes have been carried out. In all cases the agreement was perfect.

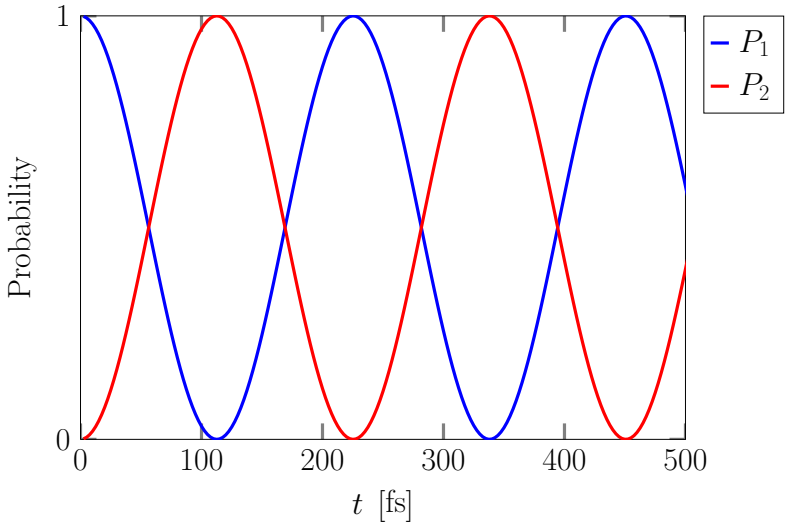

Figure 2.2: The probability of the system being found in state 1 ($P_1(t) = \langle\Psi_1(t)|\Psi_1(t)\rangle$) and state 2 ($P_2(t) = \langle\Psi_2(t)|\Psi_2(t)\rangle$) as a function of time. The fundamental period of the Rabi oscillations is 226.54 fs.

2.2 Classical Molecular Dynamics Simulations

Numerous codes for classical Molecular Dynamics (MD) simulations are available, but the simulations reported in this thesis require nonstandard setup and output, and therefore, the codes are written by the author. The two liquids H_2O and CCl_4 are studied, but in the following sections the numerical results are only shown for simulations of H_2O.

2.2.1 Numerical Integrator

The core routine of a code for classical MD simulations is the numerical integrator, which solves the coupled set of Newton's equations of motion for a system of interacting particles. We have used either the Velocity-Verlet algorithm or the Gear Predictor-Corrector algorithm to carry out the time propagation of the systems.[31, 99, 100] Here, we present only the Velocity-Verlet algorithm.

The propagation of the position of atom α_i of molecule i from time t to $t + \delta t$ reads

$$\mathbf{r}_{\alpha_i}(t + \delta t) = \mathbf{r}_{\alpha_i}(t) + \delta t\, \mathbf{v}_{\alpha_i}(t) + \frac{\delta t^2}{2m_{\alpha_i}} \mathbf{F}_{\alpha_i}(t)\,, \tag{2.14}$$

and the corresponding propagation of the velocity of atom α_i is given by

$$\mathbf{v}_{\alpha_i}(t + \delta t) = \mathbf{v}_{\alpha_i}(t) + \frac{\delta t}{2m_{\alpha_i}} \left(\mathbf{F}_{\alpha_i}(t) + \mathbf{F}_{\alpha_i}(t + \delta t)\right)\,, \tag{2.15}$$

where m_{α_i} is the mass of atom α_i, and $\mathbf{F}_{\alpha_i}$ is the force acting on α_i. The global error (i.e. the numerical error in computing a conserved quantity such as the total energy E of an isolated system from two integration steps separated by a finite time) is of the order δt^2. A rigorous test of the implementation of the Velocity-Verlet algorithm is to undertake several runs with the same initial conditions for the system and covering the same total time, but with different values of the time step δt. The standard deviation of the energy fluctuations for each run as a function of δt^2 should be linear.[101]

2.2.2 Force Fields

The interactions between the molecules in the liquids are defined by molecular mechanics force fields. For both systems, the intermolecular forces are derived from Lennard-Jones 12-6 potentials

$$U_{\mathrm{LJ}}(r) = \left(\frac{B}{r}\right)^{12} - \left(\frac{A}{r}\right)^{6} = 4\epsilon\left(\left(\frac{\gamma}{r}\right)^{12} - \left(\frac{\gamma}{r}\right)^{6}\right), \tag{2.16}$$

where $\gamma = B^2/A$ and $\epsilon = A^{12}/(4B^{12})$, and Coulomb potentials

$$U_{\mathrm{C}}(r) = \frac{q_1 q_2}{4\pi\epsilon_0 r}, \tag{2.17}$$

where q_1 and q_2 denote the charges of the interaction sites, and ϵ_0 is the vacuum permittivity.[31] In both cases r denotes the internuclear distance. The force field parameters used for each system are listed in the corresponding chapters.

2.2.3 Constrained Dynamics

The molecules are treated as rigid rotors, i.e. bond lengths and bend angles are kept constant during the time propagation. Two methods for this type of constrained dynamics have been used. One is the RATTLE algorithm, in which a set of constraints are maintained by an iterative procedure, and the other is the Quaternions method, where Euler's rigid body equations are solved using quaternions to represent orientations.[102, 103] Here, we present only the RATTLE algorithm.

The constraints for rigid rotors are of the type that require certain pairs of atoms to remain a fixed distance apart. If α_i and β_i are such a pair of constrained atoms with a distance d_{α_i,β_i}, we define the constraint as

$$C_{\alpha_i,\beta_i} \equiv |\mathbf{r}_{\alpha_i} - \mathbf{r}_{\beta_i}|^2 - d_{\alpha_i,\beta_i} = 0\,. \tag{2.18}$$

The time derivative of the constraint equation gives a constraint on the velocities

$$\dot{C}_{\alpha_i,\beta_i} \equiv \frac{\mathrm{d}C_{\alpha_i,\beta i}}{\mathrm{d}t} = 2\left(\mathbf{v}_{\alpha_i} - \mathbf{v}_{\beta_i}\right)\cdot\left(\mathbf{r}_{\alpha_i} - \mathbf{r}_{\beta_i}\right) = 0\,, \tag{2.19}$$

such that not only the distance is kept fixed, but the velocity vector $\mathbf{v}_{\alpha_i} - \mathbf{v}_{\beta_i}$ is kept perpendicular to the distance vector $\mathbf{r}_{\alpha_i} - \mathbf{r}_{\beta_i}$, which is the case for a rigid rotor. The equation of motion for constrained dynamics reads

$$m_{\alpha_i}\mathbf{a}_{\alpha_i} = \mathbf{F}_{\alpha_i} + \mathbf{G}_{\alpha_i}\,, \tag{2.20}$$

where $\mathbf{a}_{\alpha_i}$ is the acceleration of atom α_i, $\mathbf{F}_{\alpha_i}$ denotes the force on atom α_i due to the intermolecular interactions, and $\mathbf{G}_{\alpha_i}$ is the force on atom α_i due to the constraints. $\mathbf{G}_{\alpha_i}$ can be written as a sum of products of the relevant constraints and time-dependent Lagrange multipliers. In the RATTLE algorithm $\mathbf{G}_{\alpha_i}$ is determined by an iterative procedure. For more comments on the implementation of the RATTLE algorithm and explicit formulas for computing $\mathbf{G}_{\alpha_i}$, see Ref. [102]. Furthermore, the global error of the Velocity-Verlet algorithm is invariant to the implementation of the RATTLE algorithm.

2.2.4 Periodic Boundary Conditions

In order to carry out computer experiments on a liquid, which from a microscopic point of view is infinitely large, we apply periodic boundary conditions to a cubic simulation box of length L with N molecules.[104] Hence, the liquid is described as a 3-dimensional lattice, where the cubic simulation box represents the unit cell. Furthermore, we use the minimum image convention to keep the number of interactions finite.[105]

2.2.5 Initial Conditions

In the simulation box the center of mass of the molecules resemble a simple cubic lattice structure, and the orientation is the same for all molecules. The box length L is chosen such that the density corresponds to the experimental value at the chosen thermodynamic temperature T. The molecular linear velocities corresponding to T are given by the Maxwell-Boltzmann distribution

$$f_{\mathrm{lv}}(v_i) = \left(\frac{m}{2\pi k_{\mathrm{B}} T}\right)^{1/2} \exp\left(-\frac{m v_i^2}{2 k_{\mathrm{B}} T}\right) \,,\; i = x, y, z \,, \tag{2.21}$$

where m is the mass of the molecule, and k_{B} is the Boltzmann constant.[106] Similarly, the molecular angular velocities are given by the normal distribution

$$f_{\mathrm{av}}(\omega_i) = \left(\frac{I_{ii}}{2\pi k_{\mathrm{B}} T}\right)^{1/2} \exp\left(-\frac{I_{ii} \omega_i^2}{2 k_{\mathrm{B}} T}\right) \,,\; i = x, y, z \,, \tag{2.22}$$

where I_{ii} denotes the principal moments of inertia, and ω_i is the i-component of the angular velocity vector associated with the molecular frame in which the moment of inertia matrix is diagonal. The random normal deviates are obtained with the formulas reported by Box and Muller.[107]

2.2.6 Ewald Summation

In MD simulations with periodic boundary conditions, the point charge lattice becomes infinite. Therefore, the lattice sum, i.e. the sum of Coulomb potential energy terms for interactions between the charges in the simulation box and interactions with all their images, becomes conditionally convergent.[108, 109] The Ewald summation takes care of this difficulty by recasting the lattice sum into two rapidly converging sums; One sum in real space and the other in Fourier space.[110] The physical interpretation of the partition of the lattice sum is that every point charge is 'neutralized' by a Gaussian charge cloud of opposite sign. The screening of the point charges makes the interactions short ranged, and hence, the lattice sum in real space becomes absolute convergent. A Gaussian charge cloud of the same sign as each point charge is added to compensate for the first charge cloud. The expression for the second charge cloud is Fourier transformed such that the contribution to the lattice sum is found in Fourier space. Explicit formulas for calculating the Ewald sum are reported by Sangster and Dixon.[111]

In Tab. 2.2 the potential energy contributions in Fourier space are given as a function of k-vectors and the Ewald parameter α (for a system with 216 H_2O molecules). Here $k_{\max}$ denotes the maximum value of $(k_x^2 + k_y^2 + k_z^2)^{1/2}$, where $k_i \in \mathbb{Z}$ for $i = x, y, z$, and N_k is the corresponding number of k-vectors. Since α is inversely proportional to the width of the Gaussian charge distributions, the number of k-vectors for convergence of the lattice sum in Fourier space increases, when α is increased. Since the minimum image convention is applied in the MD simulations, the cutoff distance for intermolecular interactions is bounded from above by $L/2$. Hence, the screening of the point charges at the cutoff distance should be effective (otherwise some charge-charge interactions are left out in the Ewald summation). In the bottom line of Tab. 2.2 the screening factor at a distance $L/2$ is given. In the MD simulations a parameter set of $k_{\max} = 5$ and $\alpha = 6/L$ is chosen.

2.2.7 Nosé-Hoover Thermostat

The ordered initial positions of the molecules are chosen for pure convenience, but this configuration leads to a very repulsive state. Thus, the molecules gain a large amount of kinetic energy in the first 500 fs of the propagation of the system (in fact, the temperature

Table 2.2: Potential energy contributions in Fourier space

$k_{\max}/N_k$	$\alpha L = 5$	$\alpha L = 6$	$\alpha L = 7$
2/32	$5.380 \cdot 10^{-2}$	$6.760 \cdot 10^{-2}$	$7.825 \cdot 10^{-2}$
3/122	$7.716 \cdot 10^{-2}$	$1.179 \cdot 10^{-1}$	$1.595 \cdot 10^{-1}$
4/256	$8.292 \cdot 10^{-2}$	$1.414 \cdot 10^{-1}$	$2.153 \cdot 10^{-1}$
5/514	$8.358 \cdot 10^{-2}$	$1.477 \cdot 10^{-1}$	$2.409 \cdot 10^{-1}$
6/924	$8.363 \cdot 10^{-2}$	$1.491 \cdot 10^{-1}$	$2.524 \cdot 10^{-1}$
7/1418	$8.363 \cdot 10^{-2}$	$1.493 \cdot 10^{-1}$	$2.555 \cdot 10^{-1}$
8/2108	$8.363 \cdot 10^{-2}$	$1.493 \cdot 10^{-1}$	$2.561 \cdot 10^{-1}$
9/3070	$8.363 \cdot 10^{-2}$	$1.493 \cdot 10^{-1}$	$2.561 \cdot 10^{-1}$
$\exp(-\alpha^2(L/2)^2)$	$1.930 \cdot 10^{-3}$	$1.234 \cdot 10^{-4}$	$4.785 \cdot 10^{-6}$

is increased from $\sim$ 300 K to $\sim$ 1200 K). Since the MD simulations should be carried out at $T \approx 300$ K, the velocities have to be rescaled. It is easy to remove kinetic energy from the system: By running a simulation of 10 ps and saving the positions, a new 10 ps run can be carried out with the saved positions and zero velocities as initial conditions. This procedure can be repeated until the averaged temperature is close to T. In order to fine tune the average temperature, the Nosé-Hoover thermostat is applied.[112–114] In essence, the thermostat makes use of a bath coordinate, such that energy can flow between the system and the bath.

2.2.8 Tests of Numerical Stability

The codes for classical MD simulations have been thoroughly tested for numerical stability. In Fig. 2.3 the fluctuations of the total energy $E - \langle E \rangle$ for a system of 216 H_2O molecules as a function of time are shown for two calculations with time steps $\delta t = 1.0$ fs and $\delta t = 0.1$ fs (the Nosé-Hoover thermostat is turned off). Clearly, the energy fluctuations decrease as the time step is lowered (with the chosen energy interval, the fluctuations are not visible for $\delta t = 0.1$ fs). Furthermore, we have calculated the standard deviation of the energy fluctuations σ_E for four time steps (1.0 fs, 0.1 fs, 0.01 fs, and 0.001 fs), and σ_E as a function of δt^2 is well represented by a linear function as expected.

RATTLE Algorithm

The implementation of the RATTLE algorithm is tested by several runs of 100 ps with different sets of iteration criteria and number of iterations and with different values of the time step δt. With a criteria of iteration equal to 10^{-12} (10^{-7}) in reduced units and $\delta t \leq 1.0$ fs, a sufficient number of iterations is 100 (50). In Fig. 2.4 the maximum values of the discrepancy from the constraints

$$\max(C_r) = \max(||\mathbf{r}_{\alpha_i,\beta i}|^2 - d_{\alpha_i,\beta_i}|) \quad \text{and} \quad \max(C_v) = \max(|\mathbf{r}_{\alpha_i,\beta_i} \cdot \mathbf{v}_{\alpha_i,\beta i}|) \tag{2.23}$$

are shown as functions of time.

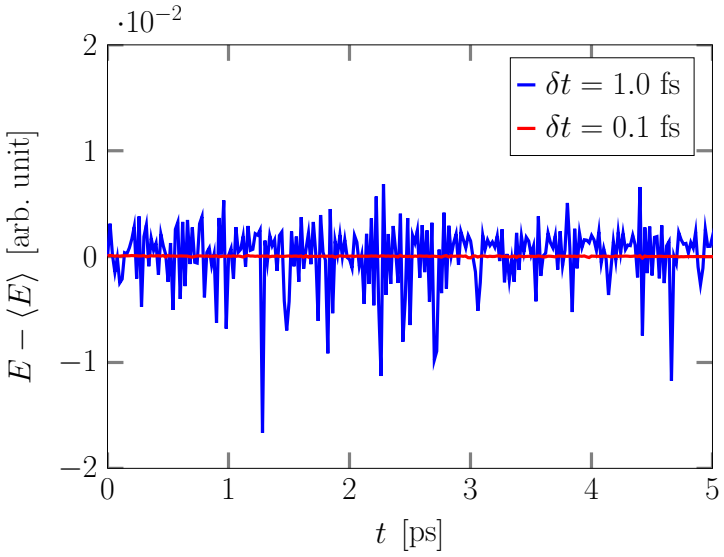

Figure 2.3: Fluctuations of the total energy $E - \langle E \rangle$ for two MD simulations with time steps $\delta t = 1.0$ fs and $\delta t = 0.1$ fs (the Nosé-Hoover thermostat is turned off).

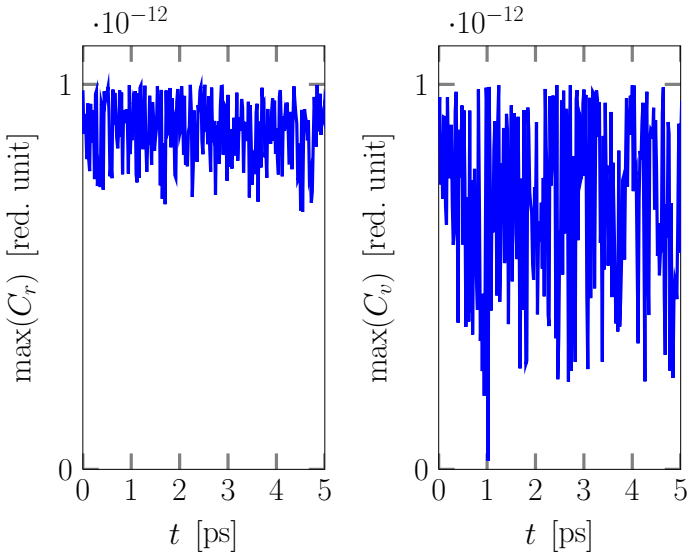

Figure 2.4: Maximum values of the discrepancy from the constraints $\max(C_r)$ and $\max(C_v)$ as functions of time. The criteria of iteration is 10^{-12} in reduced units, and the number of iterations is 100.

Radial Distribution Functions

The radial distribution function $g(r)$ for a liquid is related to the total number N of molecules by the following expression [106]

$$\int_0^\infty \mathrm{d}r \, 4\pi\rho g(r) r^2 = N - 1 \approx N \,, \tag{2.24}$$

where ρ is the number density of molecules. The relation can also be written in the following form

$$4\pi\rho g(r)r^2 = \frac{\mathrm{d}N}{\mathrm{d}r} \approx \frac{\Delta N}{\Delta r} = \frac{N(r+\Delta r) - N(r)}{\Delta r}\,. \tag{2.25}$$

If $N(r_i)$ denotes the number of molecules positioned at a distance between r_i and $r_i + \Delta r$, we get

$$g(r_i) \approx \frac{N(r_i)}{4\pi\rho r_i^2 \Delta r}\,, \tag{2.26}$$

which is the expression used by Rahman.[115] This formula can be used for CM-CM (Center of Mass) pairs and for O-O pairs in the case of H_2O molecules. A similar expression can be used for H-H and O-H pairs with a normalization factor obtained by counting the H-H and O-H pairs for a given number of molecules and comparing with the O-O pairs. In Fig. 2.5 the radial distribution function for O-O, H-H, and O-H pairs as function of distance is shown. They are all obtained from a 1 ns NVT-ensemble simulation with 1000 H_2O molecules at $T \approx 298$ K, and they reproduce the radial distribution functions reported by Mark and Nilsson.[116]

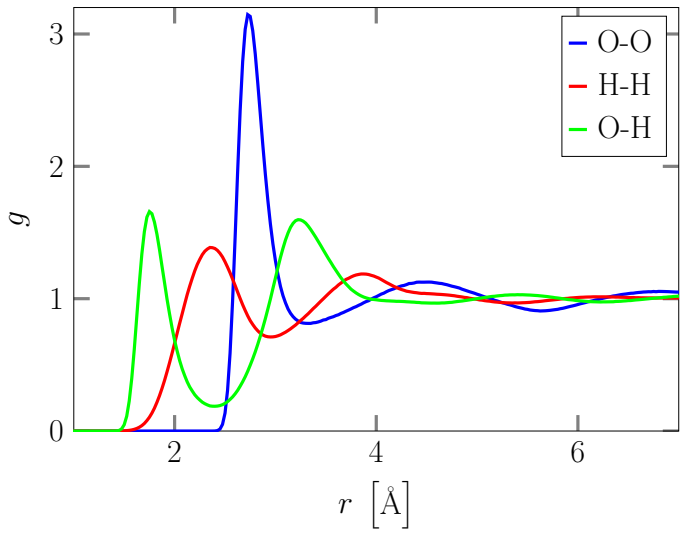

Figure 2.5: Radial distribution function for O-O, H-H and O-H pairs obtained from a 1 ns NVT-ensemble simulation with 1000 H_2O molecules at an average temperature of $T \approx 298$ K.

Diffusion Coefficient

The self-diffusion coefficient D is related to the mean square displacement by the Einstein formula [31]

$$\langle |\mathbf{r}(t) - \mathbf{r}(0)|^2 \rangle = 6Dt\,. \tag{2.27}$$

The self-diffusion coefficient is calculated by linear regression of the mean square displacement of the center of mass as a function of time, and we get $D \approx 2.6 \cdot 10^{-9}$ m^2/s, which is in perfect agreement with the self-diffusion coefficient reported by Mark and Nilsson (the data is obtained from the 1 ns NVT-ensemble simulation with 1000 H_2O molecules at $T \approx 298$ K).[116]

Velocity Distributions

Molecular linear and angular velocity distributions are calculated from the 1 ns simulation with 1000 H_2O molecules at $T \approx 298$ K. The calculated distributions are compared with the expressions in Eq. 2.21 and Eq. 2.22, see Fig. 2.6, and the agreement is excellent. From this follows that the averaged kinetic energy associated with the translational and rotational degrees of freedom is correct, and thus, the principle of equipartition of energy is not violated.[106] After the numerical tests and comparison with various published data, we conclude that the codes are working correctly.

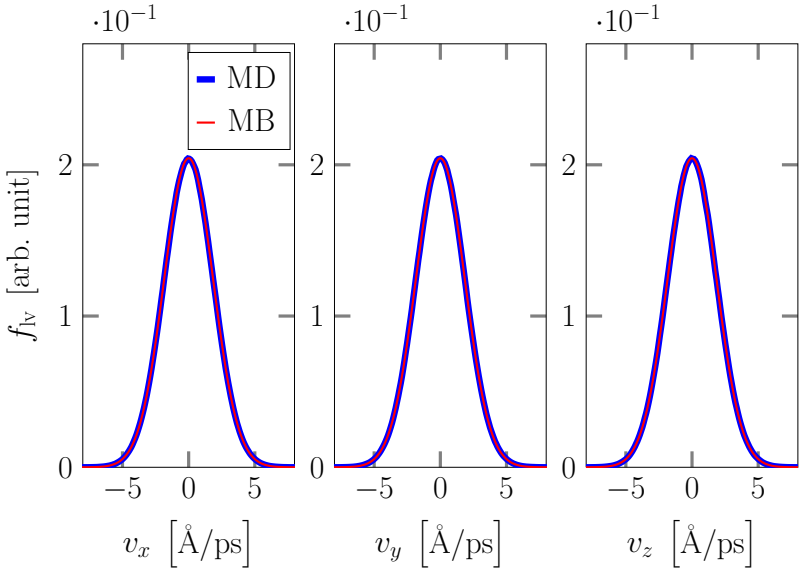

(a) Molecular linear velocity distributions for the x-, y-, and z-components.

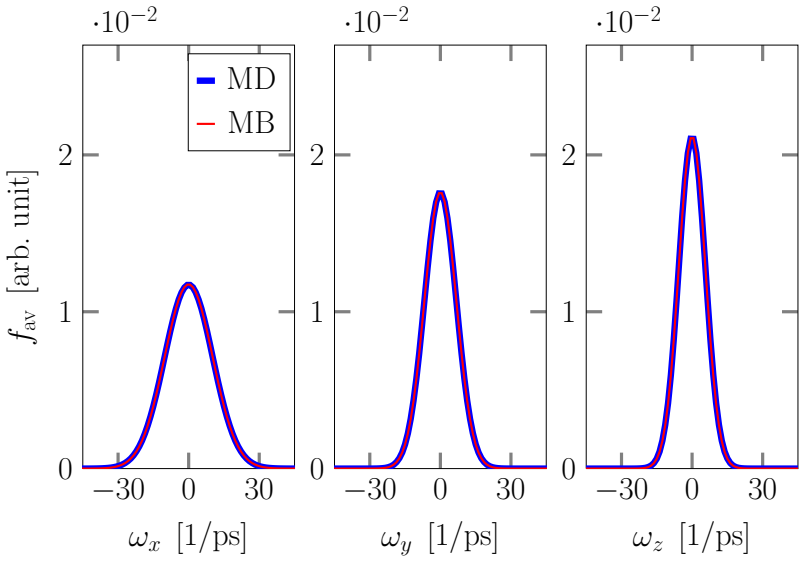

(b) Molecular angular velocity distributions for the x-, y-, and z-components.

Figure 2.6: The molecular linear (a) and angular (b) velocity distributions obtained from a Molecular Dynamics (MD) simulation are compared with the Maxwell-Boltzmann (MB) expressions in Eq. 2.21 and Eq. 2.22, respectively.

Chapter 3

Validity of the Bersohn-Zewail Model beyond Justification

The absorption of probe pulses in ultrafast pump-probe experiments on photodissociation of gas-phase molecules can be determined from the classical Bersohn-Zewail (BZ) model.[37, 42] The model relies on classical mechanics to describe the time evolution of the position of the nuclei in the excited electronic state prepared by an ultrashort pump pulse, and the initial position of the trajectory is chosen as the resonance position. The BZ model provides good agreement between the classical trajectory and the expectation value of the position for the excited state wave packet (WP) calculated from a full quantum mechanical (QM) treatment.

We show that the usefulness of the BZ model goes far beyond the validity of the individual approximations connecting the nuclear dynamics described by the full QM treatment and the classical BZ model. The approximations involve 1st order perturbation theory, an approximate form of the promoted state WP, and the assumptions that the pump pulse is monochromatic and the nuclear dynamics is adequately governed by classical mechanics.[42]

3.1 Introduction

Due to the development of ultrafast pulsed laser techniques over the last four decades, the dynamics of elementary chemical processes can be followed in real time.[117] One of the earliest femtosecond experiments was the detection of the direct bond breakage of ICN into products of I and CN.[118, 119] Bersohn and Zewail proposed a simple model for determining the absorption of the probe pulse in pump-probe experiments on photodissociation of molecules, and hence for calculating the dissociation time for direct bond breakage.[37] The BZ model relies on classical mechanics to describe the time evolution of the position of the nuclei in the excited electronic state from which the absorption spectrum is calculated. The initial position of the classical trajectory is chosen as the resonance position, i.e. the position at which the energy of the pump photon equals the potential energy difference between the excited electronic state and the ground electronic state. In the following, we do not deal with the absorption of the probe pulse when referring to the BZ model, but focus entirely on the classical mechanics treatment of the nuclear dynamics induced by the ultrashort pump pulse.

The classical scheme of the BZ model for determining nuclear dynamics has been used successfully in a number of early studies of photodissociation reactions [38, 120–125], and the model is still in use today [39–41, 126–128] for determining the initial positions in classical trajectory calculations for photochemical reactions in gas-phase and solution. In similar treatments of the nuclear dynamics, in which a classical phase space ensemble is

propagated in the excited state, the choice of initial conditions of the ensemble is in the spirit of the BZ model.[129–132]

The well-known approximations that connect a full QM treatment of the photodissociation of a gas-phase molecule with the classical BZ model can be represented by three steps: 1) 1st order perturbation theory, 2) an approximate form of the promoted state WP, and 3) assuming that the pump pulse is monochromatic and approximate the nuclear dynamics by classical mechanics.[42] In this letter we address the validity of these approximations one by one for the photodissociation of a gas-phase Br_2 molecule, which is described by a 1-dimensional electronic two-state model, see Fig. 3.1.

We compare the time-evolution of the expectation value of the position of the excited state WP from a full QM treatment of the two-state system with the classical trajectory described by the BZ model. The apparent agreement between the two calculations is shown to be somewhat surprising in the light of the applicability of the three approximations to the system of interest. It turns out that a) the approximate form of the promoted state WP is a crude approximation to the full QM WP for durations of the pump pulse in the range 10–40 fs, and that b) the subsequent use of classical mechanics to describe the nuclear dynamics, given by the time evolution of the approximate form of the promoted state WP, is inadequate. This leads to the conclusion that two wrongs do make a right for the BZ model in the case of gas-phase photodissociation of Br_2.

3.2 The BZ Model and Photodissociation of Br_2

First, we recall how to justify the classical treatment of the nuclear dynamics in the BZ model from the full QM treatment.[42, 131, 132] In the 1-dimensional electronic two-state QM description of the Br_2 molecule, the electronic states are coupled by an ultrashort laser pulse, see Eq. 2.2 and Eq. 2.3, to which certain approximations are introduced.

1) 1st Order Perturbation Theory

We apply perturbation theory to 1st order, where the electronic and vibrational ground state wave function Ψ_1 is unaffected by the laser pulse, and the excited state WP $\Psi_2(t)$ is approximated by $\Psi_{\mathrm{pt}}(t)$ [133]

$$\begin{aligned}\Psi_{\mathrm{pt}}(t) &\propto \int_{-\infty}^{t} \mathrm{d}t' \mathrm{e}^{-i\hat{H}_2(t-t')/\hbar}\mu(r)\epsilon(t')\mathrm{e}^{-i\hat{H}_1 t'/\hbar}\Psi_1 \\ &= \mathrm{e}^{-i\hat{H}_2 t/\hbar}\int_{-\infty}^{t} \mathrm{d}t' \mathrm{e}^{i\hat{H}_2 t'/\hbar}\mu(r)\epsilon(t')\mathrm{e}^{-i\hat{H}_1 t'/\hbar}\Psi_1 \\ &\approx \hat{U}_2(t)\int_{-\infty}^{\infty} \mathrm{d}t' \mathrm{e}^{i\hat{H}_2 t'/\hbar}\mu(r)\epsilon(t')\mathrm{e}^{-i\hat{H}_1 t'/\hbar}\Psi_1\,,\end{aligned} \tag{3.1}$$

where $\hat{U}_2(t) = \mathrm{e}^{-i\hat{H}_2 t/\hbar}$, and the Hamiltonian operators $\hat{H}_1 = \hat{T} + V_1$ and $\hat{H}_2 = \hat{T} + V_2$ refer to the ground electronic state and excited electronic state, respectively. The potential energy surfaces (PESs) V_1 and V_2 are shown in Fig. 3.1. We note that the last line in Eq. 3.1 is strictly valid for times, when the ultrashort laser pulse has vanished.

In the following we refer to

$$\Psi_{\mathrm{ps}} = \int_{-\infty}^{\infty} \mathrm{d}t' \mathrm{e}^{i\hat{H}_2 t'/\hbar}\mu(r)\epsilon(t')\mathrm{e}^{-i\hat{H}_1 t'/\hbar}\Psi_1 \tag{3.2}$$

as the promoted state WP, where $\Psi_{\mathrm{ps}}(t) = \hat{U}_2(t)\Psi_{\mathrm{ps}}$ can be viewed as an artificial WP, which evolves freely on V_2 and coincides with $\Psi_{\mathrm{pt}}(t)$ for times, when the laser pulse has died out.[134] The promoted state WP is often used as the underlying basis in analytic work on photodissociation of gas-phase molecules.[42, 134]

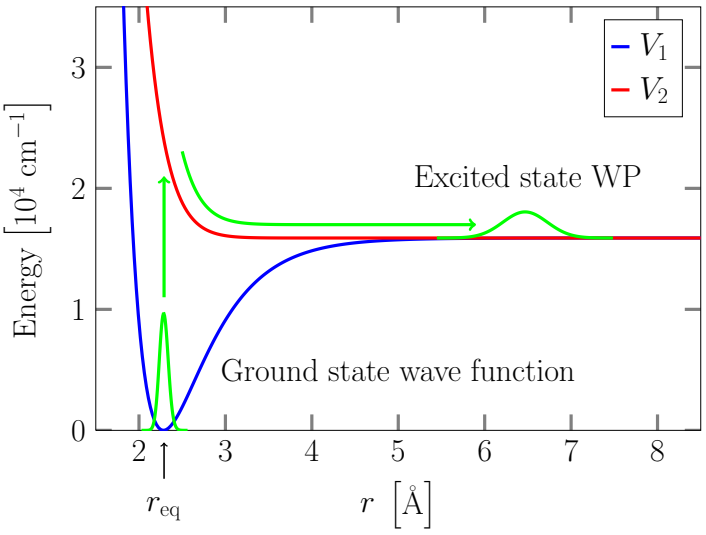

Figure 3.1: The potential energy surfaces of the 1-dimensional electronic two-state system. The electronic and vibrational ground state wave function and the excited electronic state WP are shown, along with the electronic excitation and subsequent dissociation process (indicated by arrows).

2) Approximate Form of the Promoted State WP

To make use of the Condon approximation,[135] in which the dipole moment is assumed constant in the r range spanned by Ψ_1, we substitute the expression for $\epsilon(t)$ in Eq. 2.5 into Eq. 3.2. More importantly, we neglect the commutator $[\hat{H}_2, \hat{H}_1]$ and the kinetic energy operators,[132, 136] and for times t after the excitation process has finished, we get an approximate expression for Ψ_{ps}, which is referred to as the approximate form of the promoted state WP

$$\overline{\Psi}_{\mathrm{ps}} \propto \mathrm{e}^{-\tau^2(\Delta V(r)-\hbar\omega)^2/(2\hbar^2)}\Psi_1 = g(r)\Psi_1\,, \tag{3.3}$$

where τ is the temporal duration of the laser pulse ($\mathrm{FWHM}[\epsilon] = 2\pi\sqrt{2\ln 2}$), $\Delta V(r) = V_2(r) - V_1(r)$, and ω is the carrier frequency of the laser pulse, see Sec. 2.1.1. Hence, $\overline{\Psi}_{\mathrm{ps}}$ is given by a product of the Gaussian function $g(r)$, peaking at r^* for which $\Delta V(r^*) = \hbar\omega$, and the electronic and vibrational ground state wave function Ψ_1, which is approximately bell-shaped and peaking at r_{eq}. Therefore, the product is Gaussian-like with a peak $r_{\mathrm{ps}} = \langle\overline{\Psi}_{\mathrm{ps}}|\hat{r}|\overline{\Psi}_{\mathrm{ps}}\rangle$ between r^* and r_{eq}. In classical phase space ensemble calculations, the initial conditions of the ensemble in the excited state is given by an expression similar to Eq. 3.3, where $\overline{\Psi}_1$ is substituted by a phase space distribution function.[131, 132]

3) Monochromatic Pump Pulse and Classical Mechanics

If we neglect the frequency spread of the laser pulse (τ large), then $\overline{\Psi}_{\mathrm{ps}}$ becomes a δ-function at the position r^*, at which the potential energy difference is at resonance with the photon energy $\hbar\omega$.[137, 138] In the BZ model, this δ-function is evolved according to classical mechanics, i.e. the dynamics is described by a single classical trajectory, whose initial conditions are taken as the expectation values of position and momentum of $\overline{\Psi}_{\mathrm{ps}}$

$$\begin{aligned} r_{\mathrm{BZ}}(0) &= r^* \\ p_{\mathrm{BZ}}(0) &= 0\,, \end{aligned} \tag{3.4}$$

where $\Delta V(r^*) = \hbar\omega$. Thus, the photodissociation is described without any form of QM treatment, when the PESs of the system are given.

At this point we note that even if the pulse is not assumed to be monochromatic, the dynamics of the center of $\overline{\Psi}_{\rm ps}(t) = \hat{U}_2(t)\overline{\Psi}_{\rm ps}$ will follow a classical trajectory, if at all times $\overline{\Psi}_{\rm ps}(t)$ can be contained in the r range, in which the potential V_2 can be satisfactorily approximated by a local second order polynomial. This approximation is known as the local harmonic approximation.[139] However, the initial conditions are different as this classical trajectory will start out at $r_{\rm ps}$.

3.2.1 Potential Energy Surfaces and Numerical Methods

Here we give the expressions for each PES of the 1-dimensional electronic two-state system, and describe briefly the numerical setup for the WP calculations. The PES V_1 of the adiabatic ground state of Br_2 is given by the Morse potential energy function

$$V_1(r) = D_1 \left(1 - \mathrm{e}^{-\alpha(r-r_{\rm eq})}\right)^2 , \tag{3.5}$$

where $D_1 = 15897$ cm^{-1}, $\alpha = 1.973$ Å^{-1}, and $r_{\rm eq} = 2.283$ Å.[140] The PES V_2 of the adiabatic excited state is given by the expression

$$V_2(r) = D_2 \mathrm{e}^{-\beta(r-r')-\gamma(r-r')^2} + D_1 , \tag{3.6}$$

where the parameters have the following values: $D_2 = 7654$ cm^{-1}, $\beta = 4.637$ Å^{-1}, $\gamma = 0.879$ Å^{-2}, and $r' = 2.3$ Å.[141] The numerical solution for the time-dependent Schödinger equation is found by using the Fourier transform method in connection with the split operator propagation scheme, see Sec. 2.1.[88, 92] The 1-dimensional coordinate space is represented by 16384 evenly spaced grid points in the domain $r \in [1\text{ Å}, 30\text{ Å}]$, and a time step of 0.005 fs proves to be small enough to reach convergence of the calculations (the huge number of grid points, the large r range, and the small time step are necessary, since $\overline{\Psi}_{\rm ps}(t)$ is spreading and oscillating for 'large' values of τ, i.e. $\tau \gtrsim 20$ fs). The propagation is initiated at $t_0 = -150$ fs such that $\epsilon(t_0) \approx 0$.

Initially, the Br_2 molecule is in the electronic and vibrational ground state (furthermore, the angular momentum quantum number l_1 is zero), which is obtained by propagating a trial function in imaginary time, see Sec. 2.1.5.[96] The trial function is chosen as the vibrational ground state for the harmonic potential corresponding to the 2nd order expansion of V_1 around $r_{\rm eq}$. A probability density plot of the electronic and vibrational ground state wave function Ψ_1 is shown in Fig. 3.1.

The two electronic states are coupled by a laser pulse, as described above. The intensity of the laser is chosen to be $I_0 = 0.03$ TW/cm^2, and the expression for the transition dipole moment reads

$$\mu(r) = \mu_0 + \mu_1(r - 2.3\text{ Å}) , \tag{3.7}$$

where $\mu_0 = 0.506$ D and $\mu_1 = 0.154$ D/Å.[141] The electronic excitation and subsequent dissociation process are indicated by arrows in Fig. 3.1, along with a probability density plot of the excited electronic state WP. Within the electric dipole approximation, the selection rule for an electronic transition leads to $l_2 = 1$ for the excited state. Thus, the term $\hbar^2/(mr^2)$ is added to the PES in Eq. 3.6, where m denotes the reduced mass of Br_2.[142] In the computation of the classical trajectory, the propagation is carried out with the Velocity-Verlet algorithm, see Sec. 2.2.1.[100]

3.3 Results and Discussions

As mentioned in the previous section, the approximate form of the promoted state WP $\overline{\Psi}_{\rm ps}$ is Gaussian-like with a peak $r_{\rm ps} = \langle\overline{\Psi}_{\rm ps}|\hat{r}|\overline{\Psi}_{\rm ps}\rangle$ between r^* and $r_{\rm eq}$. The position of the

peak is dependent on the width of $g(r) = \exp[-\tau^2(\Delta V(r) - \hbar\omega)/(2\hbar^2)]$, i.e., the temporal duration of the laser pulse τ. For 'short' laser pulses, i.e. $\tau \lesssim 1$ fs, $g(r)$ is broad and $\overline{\Psi}_{\rm ps}$ is peaking at $r_{\rm ps} \sim r_{\rm eq}$ (since Ψ_1 determines the peak position). For 'long' laser pulses, i.e. $\tau \gtrsim 40$ fs, $g(r)$ is narrow and $\overline{\Psi}_{\rm ps}$ is peaking at $r_{\rm ps} \sim r^*$, which is a function of the carrier frequency given by $\Delta V(r^*) = \hbar\omega$. In order to study the usefulness of the BZ model for different values of $r_{\rm ps}$, we show results for calculations with three carrier frequencies: $\omega_{\rm eq} = \Delta V(r_{\rm eq})/\hbar$ and $\omega_\pm = \Delta V(r_{\rm eq} \pm 0.1$ Å$)/\hbar$

$$\begin{aligned} \omega_+ &\approx 3874\,\text{THz} \quad (\tilde{\nu}_+ \approx 20570\,\text{cm}^{-1}) \\ \omega_{\rm eq} &\approx 4554\,\text{THz} \quad (\tilde{\nu}_{\rm eq} \approx 24180\,\text{cm}^{-1}) \\ \omega_- &\approx 5303\,\text{THz} \quad (\tilde{\nu}_- \approx 28150\,\text{cm}^{-1})\,, \end{aligned} \tag{3.8}$$

which are shown in Fig. 3.2(a). If we choose a photon energy smaller than the energy difference at $r_{\rm eq}$, then r^* is larger than $r_{\rm eq}$, and vice versa (this can easily be realized by inspection of the potentials V_1 and V_2 for r in the vicinity of $r_{\rm eq}$). Thus, for durations of the laser pulse in the interval 1 fs $\leq \tau \leq$ 40 fs, the peak of $\overline{\Psi}_{\rm ps}$ is positioned in the interval $r_{\rm eq} \lesssim r_{\rm ps} \lesssim r^*$ for $\omega < \Delta V(r_{\rm eq})/\hbar$, and $r^* \lesssim r_{\rm ps} \lesssim r_{\rm eq}$ for $\omega > \Delta V(r_{\rm eq})/\hbar$. In Fig. 3.2(b) probability density plots of $\overline{\Psi}_{\rm ps}$ for three temporal durations of the laser pulse with the carrier frequency ω_+ are shown. Clearly, the peak position of $\overline{\Psi}_{\rm ps}$ increases from $\sim r_{\rm eq}$ to $\sim r^*$, and $\overline{\Psi}_{\rm ps}$ becomes increasingly localized, when τ is increased from 1 fs to 10 fs. Hence, the use of r^* as the initial position in the BZ model was fully justified in the early experiments, since the duration of the pump pulse was of the order of 100 fs.[118]

For calculations with the three carrier frequencies we compare $\Psi_2(t)$, $\Psi_{\rm pt}(t)$, and $\overline{\Psi}_{\rm ps}(t)$ by computing the correlation functions

$$\begin{aligned} C_{\rm pt}(t) &= |\langle \Psi_2(t) | \Psi_{\rm pt}(t) \rangle| \\ C_{\rm ps}(t) &= |\langle \Psi_2(t) | \overline{\Psi}_{\rm ps}(t) \rangle|\,, \end{aligned} \tag{3.9}$$

at time $t = 200$ fs, such that the excitation process is finished and the laser pulse has died out (the WPs are normalized, i.e. a perfect correlation between two WPs corresponds to unity of the associated correlation function).

1) 1st Order Perturbation Theory

Employing 1st order perturbation theory as the only approximation we find that the correlation between $\Psi_2(t)$ and $\Psi_{\rm pt}(t)$ is perfect regardless of the values of ω and τ (in fact, the correlation is perfect at all times). Hence, the use of 1st order perturbation theory is fully justified, which is not surprising, since the population transfer in all calculations is less than 1 % for the chosen laser intensity. We conclude that the 1st approximation in the BZ model is applicable to the system of interest.

2) Approximate Form of the Promoted State WP

We now turn to the 2nd approximation: The approximate form of the promoted state WP $\overline{\Psi}_{\rm ps}$, and its time evolution. The correlation function $C_{\rm ps}(t)$ is shown for $t = 200$ fs ($\gg \tau$) in Tab. 3.1, see columns 2–4. Clearly, the correlation between $\Psi_2(t)$ and $\overline{\Psi}_{\rm ps}(t)$ is dependent on ω and τ: For 'short' laser pulses the correlation is perfect, but as the duration of the laser pulse is increased, the correlation decreases significantly. This is somewhat expected, since we neglect the commutator $[\hat{H}_2, \hat{H}_1]$ and kinetic energy operators in $\Psi_{\rm ps}$ during the laser excitation. Hence, the accuracy of the approximation is dependent on the duration of the laser pulse, i.e. the correlation decreases for all carrier frequencies, when τ is increased.

To visualize the crudeness of the 2nd approximation in the BZ model, in Fig. 3.3 we show probability density plots of $\Psi_{\rm ps}(t)$ and $\overline{\Psi}_{\rm ps}(t)$ at the two times $t = 0$ and $t = 200$ fs

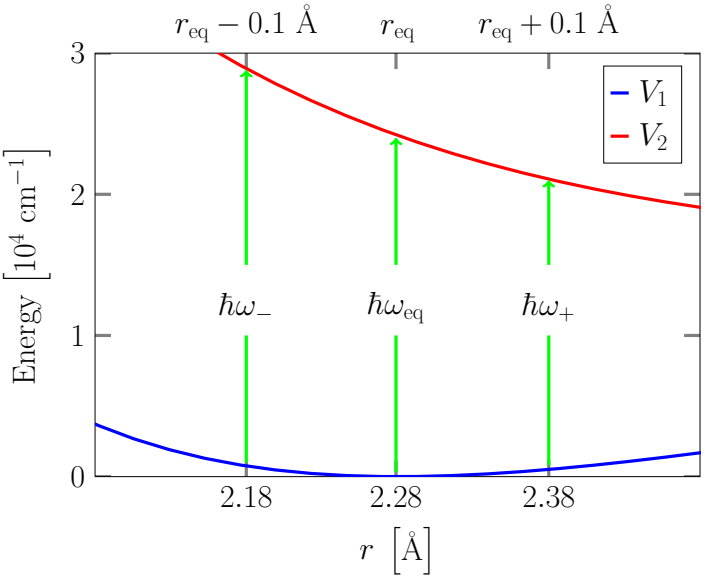

(a) Three carrier frequencies.

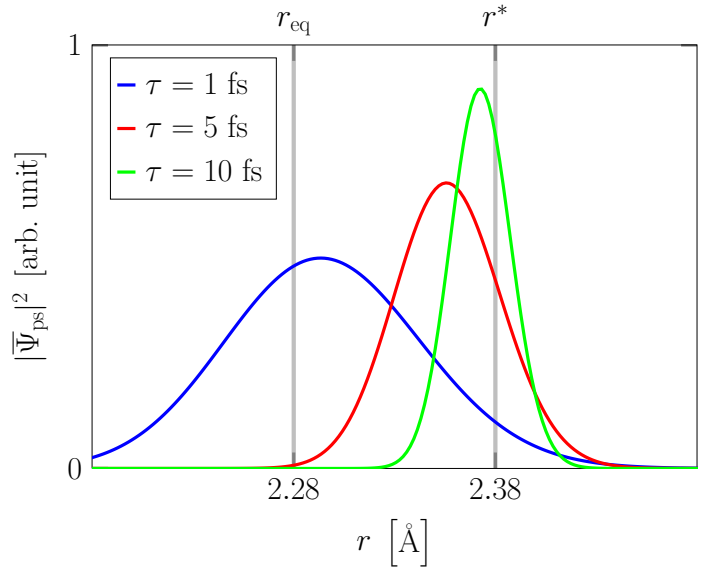

(b) Probability density of $\overline{\Psi}_{\mathrm{ps}}$ for three values of τ.

Figure 3.2: (a) Potential energy surfaces of the electronic two-state system shown in the vicinity of $r_{\mathrm{eq}} = 2.283$ Å. Three carrier frequencies of the laser pulse are indicated by arrows: ω_-, ω_{eq}, and ω_+. (b) Probability density plots of $\overline{\Psi}_{\mathrm{ps}}$ for three durations of the laser pulse: $\tau = 1$ fs, $\tau = 5$ fs, and $\tau = 10$ fs (with carrier frequency ω_+).

calculated with the carrier frequency ω_{eq}. The probability densities of $\Psi_{\mathrm{ps}}(t)$ and $\overline{\Psi}_{\mathrm{ps}}(t)$ are shown for two durations of the laser pulse, $\tau = 10$ fs and $\tau = 20$ fs, and in both cases $\overline{\Psi}_{\mathrm{ps}}(t)$ is clearly a crude approximation to $\Psi_{\mathrm{ps}}(t)$ at the two propagation times. We see that the 'interference' (the oscillatory pattern) and the broadness of $\Psi_{\mathrm{ps}}(0)$ and $\overline{\Psi}_{\mathrm{ps}}(200\ \mathrm{fs})$ is increased, when the temporal duration of the laser pulse is increased. This behavior is repeated with increasing interference and broadness for longer durations of the

Table 3.1: Correlation functions (calculated at time $t = 200$ fs) as a function of pulse duration τ and carrier frequency ω

	$C_{\mathrm{ps}}(t)$			$C_{\mathrm{lha}}(t)$		
τ/fs	ω_+	ω_{eq}	ω_-	ω_+	ω_{eq}	ω_-
1	1.00	1.00	1.00	1.00	1.00	1.00
5	0.96	0.98	0.92	0.98	0.98	0.98
10	0.65	0.76	0.53	0.86	0.89	0.83
15	0.42	0.56	0.33	0.69	0.72	0.67
20	0.30	0.43	0.24	0.56	0.57	0.56
25	0.24	0.35	0.19	0.47	0.47	0.47
30	0.19	0.29	0.15	0.40	0.39	0.41
35	0.16	0.25	0.13	0.34	0.34	0.36
40	0.14	0.22	0.11	0.30	0.29	0.31

pulse. The same pattern is found for calculations with the carrier frequencies ω_- and ω_+. We conclude that the approximate form of the promoted state WP, and hence the 2nd approximation leading to the BZ model, is only applicable to the system of interest, when the temporal duration of the laser pulse is very short, i.e. $\tau \lesssim 5$ fs. The approximation becomes increasingly poor when the duration of the laser pulse is increased.

3) Monochromatic Pump Pulse and Classical Mechanics

We now turn to the 3rd approximation: Here we neglect the frequency spread of the laser pulse (τ large) such that $\overline{\Psi}_{\mathrm{ps}}$ becomes a δ-function at the position r^*. The nuclear dynamics given by the time evolution of $\overline{\Psi}_{\mathrm{ps}}$ is described by a single classical trajectory $r_{\mathrm{BZ}}(t)$ with initial conditions given in Eq. 3.4. We compare $r_{\mathrm{BZ}}(t)$ with the two expectation values of the position

$$\begin{aligned} r_{\mathrm{QM}}(t) &= \langle \Psi_2(t) | \hat{r} | \Psi_2(t) \rangle \\ r_{\mathrm{ps}}(t) &= \langle \overline{\Psi}_{\mathrm{ps}}(t) | \hat{r} | \overline{\Psi}_{\mathrm{ps}}(t) \rangle \,, \end{aligned} \tag{3.10}$$

for the carrier frequencies ω_+ (see Fig. 3.4), ω_{eq} (see Fig. 3.5), ω_- (see Fig. 3.6), and nine temporal durations of the laser pulse.

The following comments apply to calculations with any of the carrier frequencies. We observe that $r_{\mathrm{ps}}(t)$ is a poor approximation to $r_{\mathrm{QM}}(t)$ for $\tau \gtrsim 15$ fs. This is not surprising in the light of the comparison of $\Psi_2(t)$ and $\overline{\Psi}_{\mathrm{ps}}(t)$: If the correlation between the WPs is poor, then the expectation values of the position of the WPs are most likely different. We note that the approximation becomes worse, when the temporal duration of the laser pulse is increased, which is in good agreement with the previous comments. On the other hand, we see that for $t \gtrsim 50$ fs $r_{\mathrm{BZ}}(t)$ is a fairly good approximation to $r_{\mathrm{QM}}(t)$ (and therefore, a poor approximation to $r_{\mathrm{ps}}(t)$) for all durations of the laser pulse. Thus, the 3rd approximation in the BZ model, in which $r_{\mathrm{ps}}(t)$ is assumed to be well represented by $r_{\mathrm{BZ}}(t)$ at times after the laser pulse has vanished, is not applicable to the system of interest. We can conclude that the BZ model leads to a very good description of the photodissociation

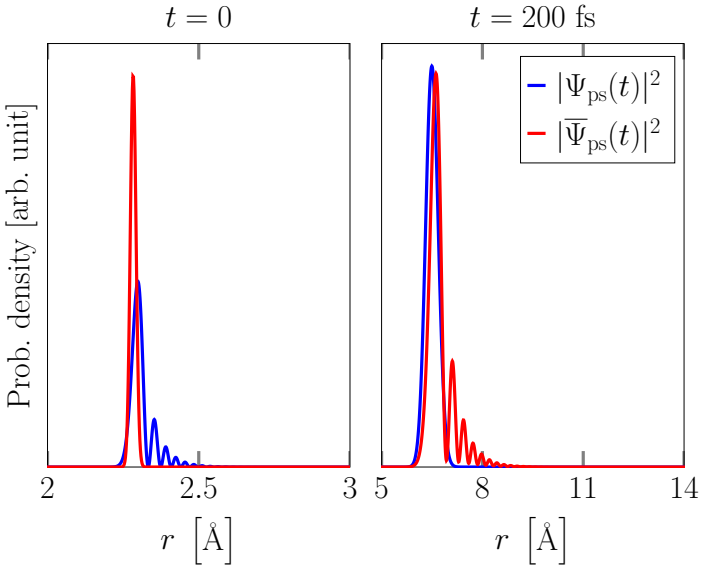

(a) Probability density for $\tau = 10$ fs.

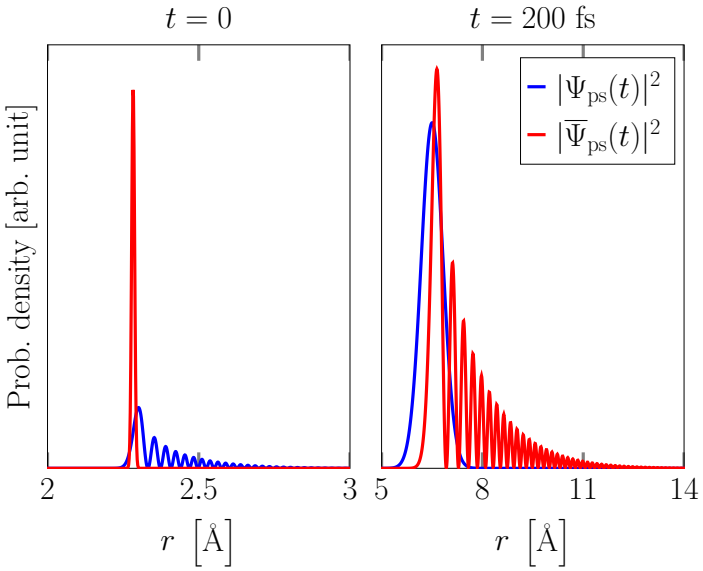

(b) Probability density for $\tau = 20$ fs.

Figure 3.3: Probability density of $\Psi_{\mathrm{ps}}(t)$ and $\overline{\Psi}_{\mathrm{ps}}(t)$ at the two times $t = 0$ and $t = 200$ fs calculated with a laser pulse duration of $\tau = 10$ fs (a) and $\tau = 20$ fs (b) (with carrier frequency ω_{eq}). The overlap $|\langle\Psi_{\mathrm{ps}}(t)|\overline{\Psi}_{\mathrm{ps}}(t)\rangle|$ is less than 0.8 in each case.

dynamics of a gas-phase Br_2 molecule, which is quite surprising, since the investigation of the validity of the 2nd and 3rd approximations connecting the BZ model with a full QM treatment does not lead to this conclusion. In fact, the nonapplicability of the 2nd and 3rd approximations seem to cancel out.

As mentioned in Sec. 3.2 for the 3rd approximation, the dynamics of the center of $\overline{\Psi}_{\mathrm{ps}}(t)$ will follow a classical trajectory for any polychromatic pulse, if the local harmonic approximation to V_2 is valid. Here, we investigate the validity of this approximation and denote the

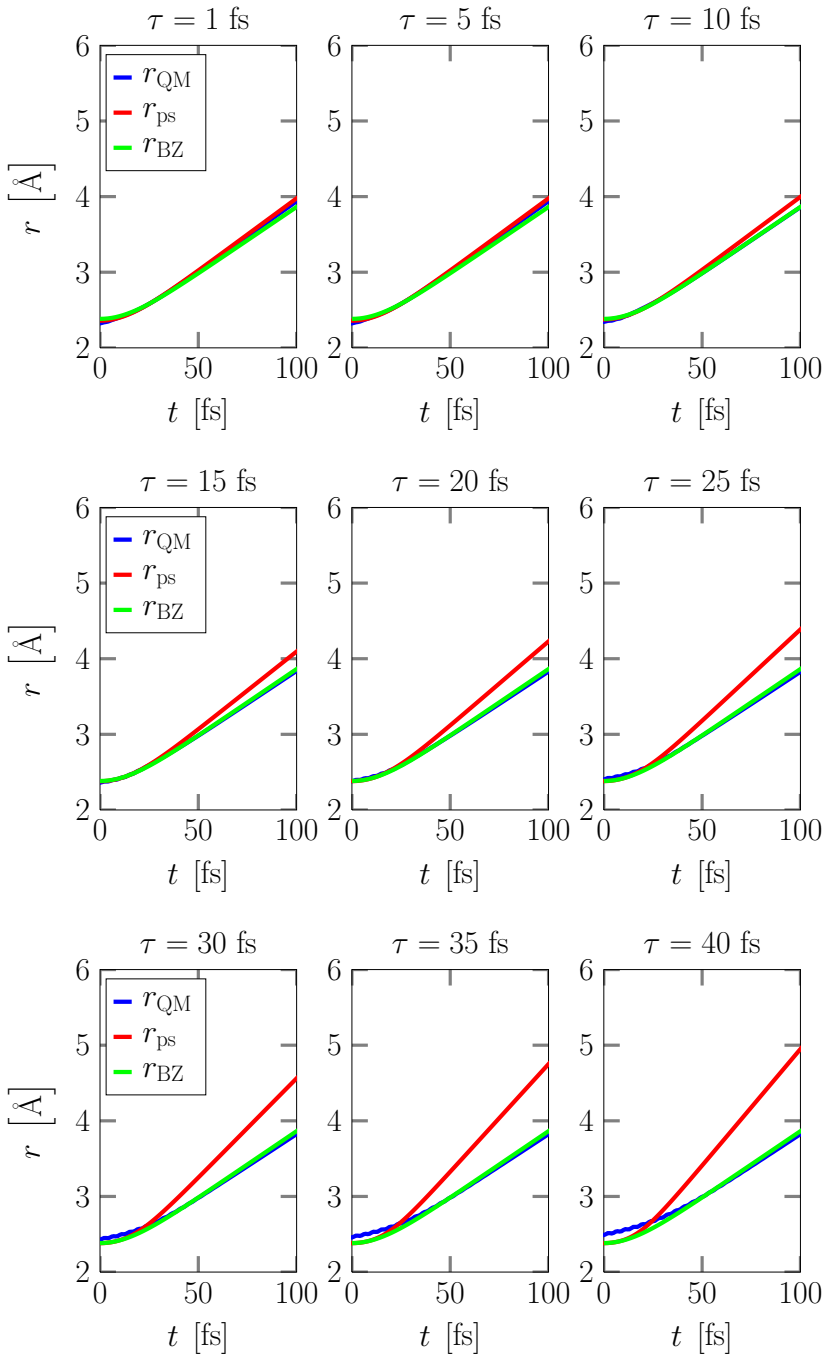

Figure 3.4: The classical trajectory $r_{\mathrm{BZ}}(t)$ (green) compared with the expectation values of the position $r_{\mathrm{QM}}(t)$ (blue) and $r_{\mathrm{ps}}(t)$ (red) for the carrier frequency ω_+. For $t \gtrsim 50$ fs, $r_{\mathrm{BZ}}(t)$ is a very good approximation to $r_{\mathrm{QM}}(t)$ for all durations of the laser pulse.

WP $\overline{\Psi}_{\mathrm{lha}}(t)$. We have calculated the correlation function $C_{\mathrm{lha}}(t) = |\langle \Psi_2(t) | \overline{\Psi}_{\mathrm{lha}}(t) \rangle|$ (where $\overline{\Psi}_{\mathrm{lha}}(0) = \overline{\Psi}_{\mathrm{ps}}(0)$) at time $t = 200$ fs, see column 5–7 in Tab. 3.1. Surprisingly, the correlation between Ψ_2 and $\overline{\Psi}_{\mathrm{lha}}$ is better than the correlation between Ψ_2 and $\overline{\Psi}_{\mathrm{ps}}$, but still far from unity for all values of ω and for $\tau \gtrsim 10$ fs. For durations of the laser pulse $\tau \gtrsim 10$ fs, $\overline{\Psi}_{\mathrm{ps}}$ becomes quite narrow in coordinate space, see Fig. 3.2(b), and therefore, quite broad

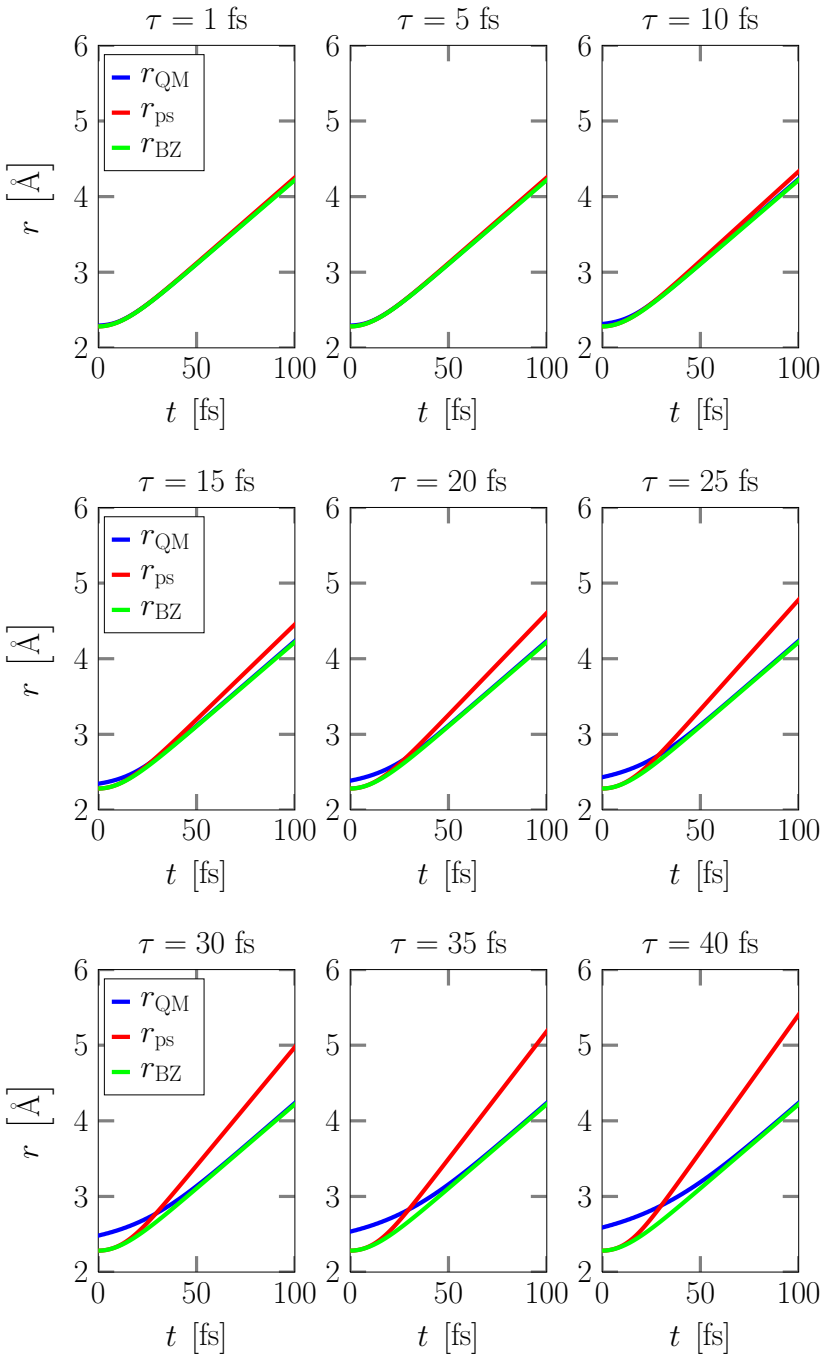

Figure 3.5: The classical trajectory $r_{\mathrm{BZ}}(t)$ (green) compared with the expectation values of the position $r_{\mathrm{QM}}(t)$ (blue) and $r_{\mathrm{ps}}(t)$ (red) for the carrier frequency ω_{eq}. For $t \gtrsim 50$ fs, $r_{\mathrm{BZ}}(t)$ is a very good approximation to $r_{\mathrm{QM}}(t)$ for all durations of the laser pulse.

in momentum space, which leads to a delocalization of $\overline{\Psi}_{\mathrm{ps}}(t)$ shortly after the propagation is initiated. Thus, the local harmonic approximation breaks down, and $\overline{\Psi}_{\mathrm{ps}}(t)$ and $\overline{\Psi}_{\mathrm{lha}}(t)$ evolve differently. Furthermore, we find that $r_{\mathrm{lha}}(t) = \langle\overline{\Psi}_{\mathrm{lha}}(t)|\hat{r}|\overline{\Psi}_{\mathrm{lha}}(t)\rangle$ match $r_{\mathrm{BZ}}(t)$ almost perfectly, with the match becoming perfect for increasing values of τ, since $r_{\mathrm{ps}}(0)$ approaches r^*, see Fig. 3.2(b). In fact, $r_{\mathrm{lha}}(t)$ is a better approximation, than $r_{\mathrm{BZ}}(t)$, to

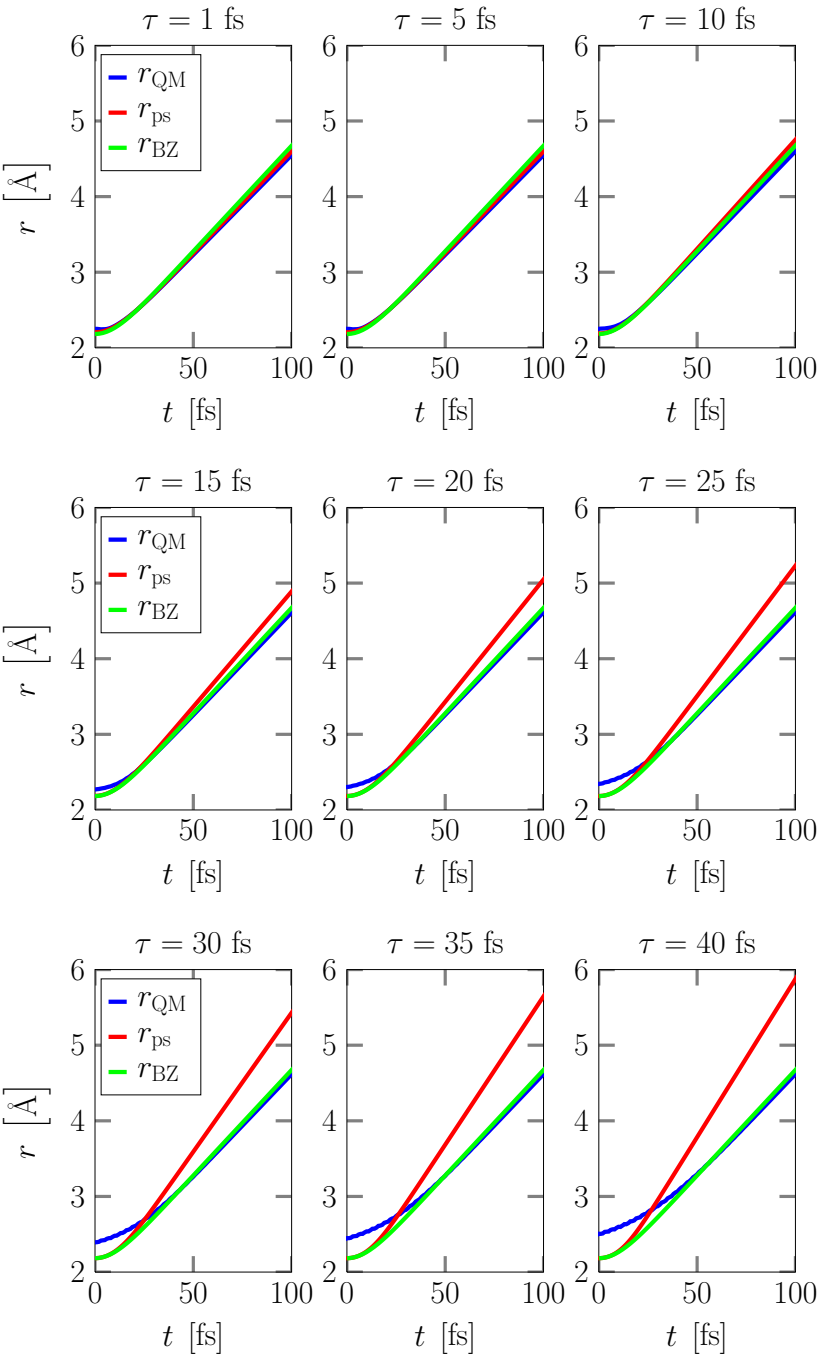

Figure 3.6: The classical trajectory $r_{\mathrm{BZ}}(t)$ (green) compared with the expectation values of the position $r_{\mathrm{QM}}(t)$ (blue) and $r_{\mathrm{ps}}(t)$ (red) for the carrier frequency ω_{-}. For $t \gtrsim 50$ fs, $r_{\mathrm{BZ}}(t)$ is a very good approximation to $r_{\mathrm{QM}}(t)$ for all durations of the laser pulse.

$r_{\mathrm{QM}}(t)$. Hence, the accuracy of the BZ model is increased, if the initial position for the classical trajectory is chosen as $r_{\mathrm{ps}}(0)$ and not r^* (see Eq. 3.10). We can conclude that the description of the nuclear dynamics by $\overline{\Psi}_{\mathrm{lha}}$ is very useful for approximating the center of $\Psi_2(t)$ for most durations of the laser pulse, but the shape of $\Psi_2(t)$ is poorly described for $\tau \gtrsim 10$ fs.

3.4 Conclusions

We have investigated the applicability of the classical scheme from the Bersohn-Zewail model to describe the nuclear dynamics for the photodissociation of a gas-phase Br_2 molecule. Clearly, the BZ model provides a good description of the dynamics, when the pump laser has vanished. This is in line with the applicability of other 'less restrictive' approaches, such as classical phase space ensemble calculations, see, e.g. Li *et al.* [131], and the use of concepts closely related to the BZ model (i.e. a resonance condition for excitation and classical mechanics to describe the dynamics) in current research on more complex systems, see e.g. Tao *et al.* [128].

The apparent usefulness of the BZ model is in contrast to the approximations involved in deriving the BZ model from a full QM treatment of the photodissociation process. The use of 1st order perturbation theory is completely justified, but the approximate form of the promoted state WP and the subsequent assumptions about a monochromatic pump pulse and the usefulness of classical mechanics to describe the nuclear dynamics are not applicable to the system of interest for durations of the pump pulse $\tau \gtrsim 5$ fs. Nonetheless, we conclude that regardless of the crude approximations for durations of $\tau \gtrsim 5$ fs, the BZ model provides a very good description of the nuclear dynamics in the case of gas-phase photodissociation of Br_2.

Chapter 4

Photodissociation and Vibrational Energy Relaxation of I_2 in CCl_4

The photodissociation, subsequent geminate recombination*, and vibrational energy relaxation of iodine in carbon tetrachloride are studied using classical nonequilibrium MD simulations. The time dependence of the vibrational energy relaxation associated with the cooling of molecular iodine in the ground electronic state is found to be in excellent agreement with time-resolved optical spectroscopy data. The time-dependent I-I pair distribution function is compared to experimental results obtained by a novel time-resolved x-ray diffraction scheme, and a qualitative agreement is established. Furthermore, we show that the time-dependent I-I pair distribution function can be extracted from the time-dependent vibrational energy distribution, hence, experimental data from time-resolved x-ray diffraction and optical spectroscopy can be compared. Last, we show that the vibrational energy relaxation exhibits some degree of coherence even at 10 ps after the laser excitation.

4.1 Introduction

The microscopic dynamics of geminate recombination of iodine atoms to form molecular iodine subsequent to photodissociation in condensed phases has been studied by spectroscopy for more than seven decades, and the simple reaction has served as a prototypical model for bimolecular solution reactions.[14] The geminate recombination of the iodine atoms after the optical laser excitation is possible due to collisions with the surrounding solvent molecules, whereby the excess vibrational energy of the newly formed iodine molecule dissipates into the various degrees of freedom of the solvent, and hence, the iodine atoms can be trapped in a bound state. This so-called cage effect of the solvent was first proposed by Franck, Rabinowitch, and Wood in the 1930's.[34–36]

Spectroscopic studies, in which the photodissociation and recombination process of I_2 in CCl_4 and various alkane liquids were monitored in real time, has provided information about the probability of geminate recombination and the time dependence of the vibrational energy relaxation.[44–48, 143] The photodissociation and geminate recombination of I_2 in various liquids and solids have also been studied by classical nonequilibrium MD simulations.[19, 52, 53, 56–60, 144] Recently, the vibrational energy relaxation of I_2 dissolved in CCl_4 has attracted renewed interest as a test-case for illustrating that time-resolved x-ray diffraction can be used to monitor transient molecular structures during a chemical reaction.[22, 48, 62] The temporally varying x-ray signal was expressed in terms of atom-atom pair distribution functions to visualize atomic motion, however, with lim-

*'Geminate recombination' refers to the recombination of iodine atoms with their original partners.

ited time-resolution of the order of 100 ps. Optical spectroscopy studies suggest that the vibrational energy relaxation of I_2 in CCl_4 is completed within $\sim$ 200 ps after the laser excitation.[45, 47] Therefore, the time-resolution of the x-ray diffraction experiments have to be enhanced to fully visualize the dynamics during the vibrational energy relaxation.

In this chapter we show classical nonequilibrium MD simulation results, where the time dependence of the vibrational energy relaxation associated with the cooling of molecular iodine in the ground electronic state is found to be in very good agreement with time-resolved optical spectroscopy data reported by Harris *et al.* [45, 47]. From the MD simulations we can calculate the time-dependent I-I pair distribution function, which we compare with data from new time-resolved x-ray diffraction experiments carried out by Michael Wulff (ESRF, France), Hyotcherl Ihee (KAIST, South Korea), and coworkers. From this comparison a qualitative agreement is established. A novel 'time-slicing' scheme is used to increase the time-resolution of the x-ray diffraction experiments to the order of 1-10 ps (see paper 2 in Preface). Furthermore, we show that a good approximation to the time-dependent I-I pair distribution function can be constructed from a knowledge of the time-dependent vibrational energy distribution. Hence, experimental results from time-resolved x-ray diffraction and optical spectroscopy can be compared.

In the solid phase (inert gas matrices) geminate recombination and vibrational energy relaxation of I_2 with vibrational coherence lasting several picoseconds has been observed in experiments and classical MD simulations, but in the liquid phase vibrational coherence has been absent, i.e. complete vibrational phase randomization of the I_2 trajectories occurred in the soft solvent cages.[52, 54, 55] In the present work, we have carried out simulations which show that the vibrational energy relaxation of I_2 in CCl_4 at standard temperature and pressure exhibits some degree of coherence, even 10 ps after the laser excitation. This partial coherent motion might be observed in the future using free electron lasers in time-resolved x-ray diffraction experiments.[23]

4.2 Computational Method

In chapter 3 we showed that the nuclear dynamics associated with gas-phase photodissociation of Br_2 is well-described by the classical scheme of the Bersohn-Zewail model. This motivates us to use a classical description of the photodissociation of I_2 in CCl_4. The computational method is presented below.

All the results reported in this chapter were obtained from classical MD simulations performed with periodic boundary conditions for a cubic simulation box of length $L \approx 43.6$ Å, and consisting of one I_2 molecule embedded in a solution of 511 CCl_4 molecules. This setup corresponded to the density of CCl_4 at $T \approx 300$ K and standard pressure (1.59 g/cm^3).[145] The classical equations of motion were integrated using the Gear Predictor-Corrector algorithm with a time step of 1 fs, and the solvent molecules were kept rigid using the Quaternions method.[31, 103] Freezing the vibrational degrees of freedom of CCl_4 was in agreement with previous experimental and computational studies, which indicated the importance of the V-T (vibrational-translational) energy transfer from solute to solvent compared to the V-V energy transfer, even for low vibrational energy states of the iodine molecule.[45, 47] (Here we note, that previous theoretical studies of the energy transfer during the vibrational energy relaxation of I_2 in CCl_4 suggest that the V-V energy transfer is more important than the V-T energy transfer.[146, 147])

All interactions were assumed to be pairwise additive. For the intermolecular C-C, Cl-Cl, and C-Cl interactions, the OPLS parameters for Lennard-Jones 12-6 potentials and Coulomb potentials were used.[148] The I-C and I-Cl interactions were modeled by Lennard-Jones 12-6 potentials with parameters constructed using the usual Lorentz-

Berthelot mixing rules, where $\epsilon_{\mathrm{I}} = 240$ K and $\sigma_{\mathrm{I}} = 3.8$ Å were determined from a fit of parameters for I-Ne and I-Ar interactions.[58, 61] The cutoff distance for terminating the Van der Waals dispersion forces was half the box length.

In the spirit of the Bersohn-Zewail model, we described the intramolecular dynamics of the I_2 molecule by two electronic states. The ground electronic state (X-state) of I_2 was represented by a Morse potential

$$V_X(r) = D\left(1 - \mathrm{e}^{-\alpha(r-r_{\mathrm{eq}})}\right)^2 , \tag{4.1}$$

with the parameters: $D = 12547$ cm^{-1}, $\alpha = 1.91$ Å^{-1}, and $r_{\mathrm{eq}} = 2.67$ Å.[149] The purely repulsive potential for the excited electronic state (Π-state) was of the form

$$V_{\Pi}(r) = \beta\left(r/\text{Å}\right)^{-9.5} + D\,, \tag{4.2}$$

with $\beta = 8.61 \cdot 10^7$ cm^{-1}.[39, 150] The potentials are shown in Fig. 4.1, along with the potentials for the A- and B-state, although they were not included in the MD simulations.[149, 150] The instantaneous electronic excitation, the dissociation, and the geminate recombination of I_2 are sketched by arrows. Initially, a vertical Franck-Condon excitation brings the I_2 molecule from the X- to the Π-state. The molecule starts to dissociate and at an internuclear distance of $r \gtrsim 5.4$ Å, the iodine atoms bounce of the solvent shell. The iodine atoms can then recombine and relax on the X-state potential.

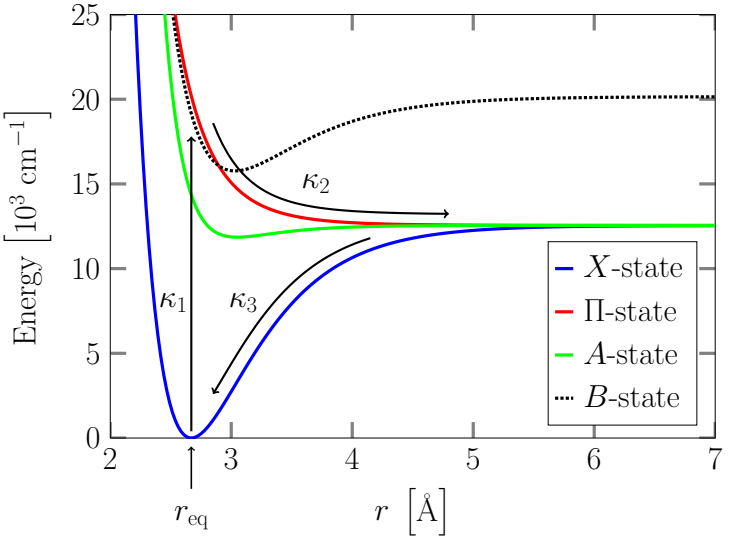

Figure 4.1: The potentials for the X- and Π-state of I_2. The potentials for the A- and B-state are also shown, although they were not included in the MD simulations. The instantaneous electronic excitation (κ_1), the dissociation (κ_2), and the geminate recombination (κ_3) are sketched by arrows.

In the classical treatment of the dynamics, an electronic transition from the Π- to the X-state — after laser excitation — can not occur. This is, however, an important quantum effect especially in the asymptotic region of the two states, where the potentials are close enough to facilitate curve crossing (and a necessity for simulating the geminate recombination and vibrational energy relaxation).[54] A simple surface hopping model was chosen in which an instantaneous deexcitation from the Π- to the X-state occurred once the energy difference between the two potentials equaled $k_{\mathrm{B}}T \approx 208$ cm^{-1} (no further

electronic excitation was allowed to take place).[38, 58] In order to maintain energy conservation 'during' the transition, $k_{\mathrm{B}}T$ was added to the kinetic energy associated with the vibrational degree of freedom of I_2, while the direction of the corresponding momentum vector was conserved.

As mentioned above, the A- and B-state were not included in the MD simulations. Clearly, the iodine atoms can also recombine in the A-state subsequent to collisions with the solvent cage, but we are only interested in the vibrational energy relaxation in the X-state. In the new time-resolved x-ray diffraction data, the experimental signal from the two recombination channels can be separated, thus, the focus on the X-state dynamics is justified (see paper 2 in Preface). Since the Π- and B-state cross close to r_{eq}, the I_2 molecule can be trapped for some time in the B-state shortly after the laser excitation. This will give rise to a longer dissociation time, and in Sec. 4.3 we comment on this deficiency of the model.

Initial conditions for the photodissociation calculations were found by classical equilibrium MD simulations performed in the canonical (NVT) ensemble at $T \approx 300$ K using the Nosé-Hoover thermostat.[113, 114] Snapshots of phase space points were saved every 10 ps. The I_2 molecule was kept rigid during the equilibration runs with a separation equal to the classical equilibrium distance r_{eq}. A contour plot of the I_2-C (center of mass of I_2 to C) pair distribution function based on the equilibrium MD simulations is shown in Fig. 4.2. This contour plot of the distribution function gives a more detailed picture of the average configuration of the solvent molecules with respect to the iodine molecule than the radial distribution function, and we see that the 1st solvent shell is approximately ellipsoidal in shape.

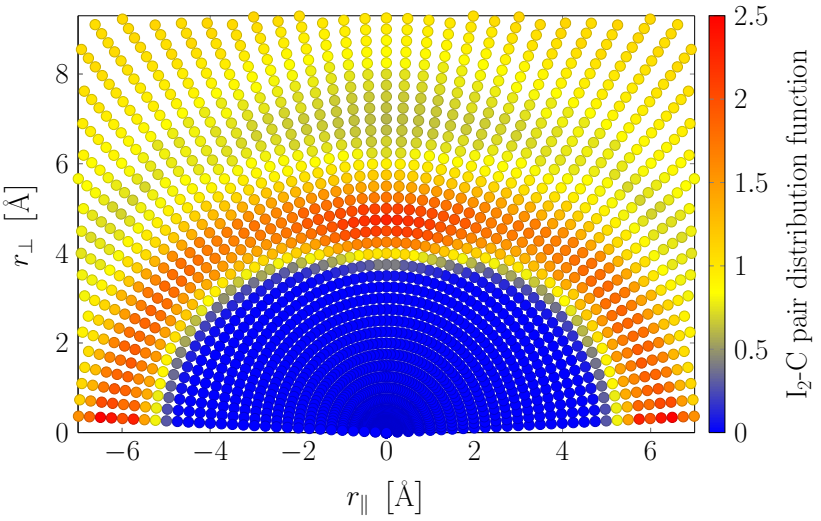

Figure 4.2: A contour plot of the I_2-C pair distribution function dependent on $r_\parallel$ (the internuclear axis of I_2 with origin at the center of mass) and $r_\perp$ (the radial distance perpendicular to the internuclear axis). The 1st solvent shell is approximately ellipsoidal in shape (the red 'belt'). Here we note that a CCl_4 molecule can be located at a distance of ~ 4 Å from the center of mass of I_2 (with a direction perpendicular to the internuclear axis).

The photodissociation trajectories were calculated in the microcanonical (NVE) ensemble to avoid non-collisional velocity scaling from the Nosé-Hoover thermostat. 272 initial conditions were used to run 200 ps photodissociation trajectories, where an instantaneous replacement of the X- by the Π-state potential mimicked an optical laser

excitation of I_2 in the spirit of the Bersohn-Zewail model. Hence, at the first integration step the total energy of the system increased by $\sim$ 20000 cm^{-1} (the energy difference between the two electronic states at the distance r_{eq}, see Fig. 4.1).

4.3 Results and Discussions

For 32 trajectories out of 272 the iodine atoms escape the solvent cage and do not recombine within 200 ps. Hence, the probability of escaping the cage is approximately 12 %, which is in good agreement with experimental results.[151] The criterion for the electronic deexcitation from the Π- to the X-state corresponds to a separation between the iodine atoms of $\sim$ 5.2 Å, which is nearly always reached before the iodine atoms reapproach (if they do not escape the solvent cage) on the X-state potential due to collisions with solvent molecules. For approximately 6 % of the trajectories the iodine atoms oscillate twice or more before reaching a separation of $\sim$ 5.2 Å.

In Fig. 4.3(a) two examples of the time-dependent I-I distance in the first 3 ps after the laser excitation are shown. In both nonequilibrium runs the initial I-I distance corresponds to r_{eq}, since the iodine molecule is kept rigid during the MD simulations (in the NVT ensemble) from which the initial conditions are found. In run 1 a solvent molecule slips 'in between' the iodine atoms during the initial separation after the laser excitation, and within $\sim$ 2 ps the configuration of the solvent has changed such that the iodine atoms can recombine. In Fig. 4.2 we see that a CCl_4 molecule can be located at a distance of $\sim$ 4 Å from the center of mass of I_2 (with a direction perpendicular to the internuclear axis) which is the case for run 1. In run 2 the iodine atoms recombine immediately after the first collision with the solvent cage. The average I-I distance based on the truncated set of nonequilibrium MD simulations (240), for which the iodine atoms do recombine, is also shown in Fig. 4.3(a).

The X- and Π-state potentials used in this study are calculated for gas-phase I_2 molecules. Hence, the 'true' intramolecular potentials for I_2 dissolved in CCl_4 might be somewhat different due to the electron distribution of the solvent molecules. In Fig. 4.3(b) we have compared the magnitude of the forces acting on the iodine atoms during the recombination in run 2. The magnitude of the force $F_{\text{I-I}}$ derived from the X-state potential is almost identical to the magnitude of the total force acting on each of the iodine atoms, F_{I_a} and F_{I_b}, when the I-I distance is close to the classical equilibrium distance r_{eq}. Therefore, we can assume that the gas-phase X-state potential of the I_2 molecule is a fairly good approximation to the 'true' ground electronic state potential for I_2 dissolved in CCl_4 at least with the chosen force field parameters.

4.3.1 Vibrational Energy Distribution

In Fig. 4.4 the density $\bar{\gamma}(E,t)$ of the vibrational energy of I_2 as a function of time is shown based on the truncated set of nonequilibrium MD simulations (240), where the density is constructed from instantaneous vibrational energy distributions $\gamma(E,t)$ averaged over an interval of 100 fs (a typical time duration of a pump pulse used in optical spectroscopy) for every 2 ps. The color bar on the right hand side of the plot shows the magnitude of $\bar{\gamma}(E,t)$. The vibrational energy consists of potential energy $E_{\text{pot}} = V_X(r)$ and kinetic energy $E_{\text{kin}} = \mu v^2/2$, where μ is the reduced mass of I_2 and v denotes the magnitude of the relative velocity vector projected on the bond vector.

Since the average vibrational energy based on the MD simulations clearly coincides with the time-resolved optical spectroscopy results reported by Harris *et al.* [45, 47], the force field parameters seem to be well suited for studying the photodissociation, geminate recombination, and vibrational energy relaxation of I_2 dissolved in CCl_4 at $T \approx 300$ K and

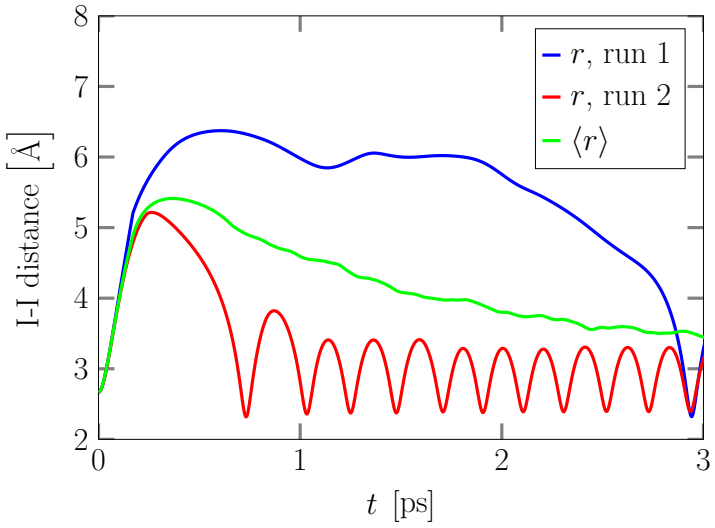

(a) I-I distance as a function of time.

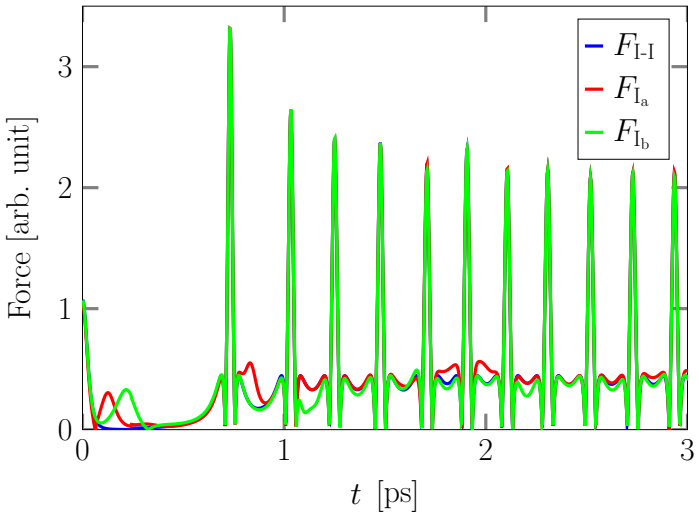

(b) Magnitude of the force on the I atoms as a function of time.

Figure 4.3: (a) I-I distance as a function of time for two nonequilibrium MD simulations. The average I-I distance $\langle r \rangle$ based on the truncated set of nonequilibrium MD simulations is also shown. (b) Magnitude of the forces on the iodine atoms as a function of time for run 2: The I-I interaction (blue), the total force on I_a (red), and the total force on I_b (green).

standard pressure. Here we note that the time-resolution of the experiments performed by Harris *et al.* is ~ 1 ps, thus, the time-resolution of the MD simulation results (100 fs) is not biasing the comparison.

The nonequilibrium MD simulations show that approximately 40 % of the initial vibrational energy is on average lost upon the first few collisions with the solvent cage (this energy loss corresponds to the initial potential energy in the Π-state relative to the asymp-

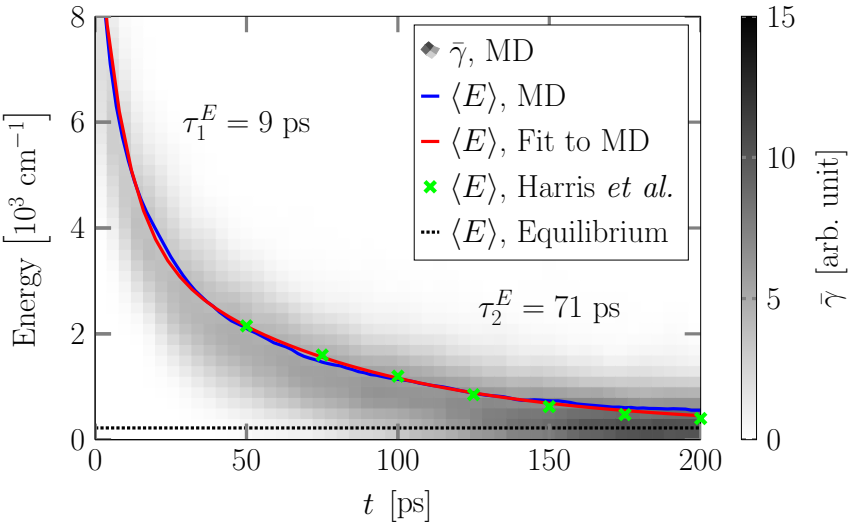

Figure 4.4: The density $\bar{\gamma}(E,t)$ of the vibrational energy as a function of time. Fit of a bi-exponential function (red) to the average vibrational energy (blue) gives the relaxation times $\tau_1^E = 9$ ps and $\tau_2^E = 71$ ps. The equilibrium vibrational energy of I_2 in the X-state at $T \approx 300$ K is ~ 222 cm^{-1} (black dotted line). Clearly, the MD simulation results coincide with the experimental data from Harris *et al.* [45, 47] (green x-marker). Note that the relaxation is not quite completed within 200 ps.

totic region). This dramatic loss of vibrational energy has been reported previously for photodissociation of iodine in inert gas matrices.[52, 53]

We also observe that the decrease in the vibrational energy is significantly larger during the first 50 ps of the MD simulations than during the last 150 ps. In fact, the loss of vibrational energy is approximately 90 % for the first time window and 8 % for the last (the relaxation is not quite completed at 200 ps after the laser excitation, hence, the missing 2 %). The equilibrium vibrational energy of I_2 in the X-state at $T \approx 300$ K is ~ 222 cm^{-1}, which is determined by an equilibrium MD simulation of a vibrating I_2 molecule in the electronic X-state at $T \approx 300$ K. Hence, the average vibrational energy $\langle E \rangle$ based on the nonequilibrium MD simulations approaches ~ 222 cm^{-1}, for t approaching infinity (here we have neglected the slight increase in the average temperature due to the energy added to the system by the laser excitation). A fit to $\langle E \rangle$ of a bi-exponential function of the type

$$f(t) = A_E \exp(-t/\tau_1^E) + B_E \exp(-t/\tau_2^E) + 222\ \mathrm{cm}^{-1}\,, \tag{4.3}$$

gives the relaxation times $\tau_1^E = 9$ ps and $\tau_2^E = 71$ ps ($A_E = 6248$ cm^{-1} and $B_E = 3824$ cm^{-1}). We can conclude, that the vibrational energy cooling of iodine in carbon tetrachloride is very well described by two relaxation times, which is in agreement with time-resolved optical spectroscopy data.[45]

The density plot in Fig. 4.4 shows that the vibrational energy distribution has a significant spread in energy at all times, and that the characteristic shape of the distribution changes in time. In Fig. 4.5 the vibrational energy distribution at two times, $t = 20$ ps and $t = 200$ ps, is plotted. We see that the distribution at $t = 20$ ps is approximately Gaussian. The equilibrated vibrational energy distribution ($t = \infty$), which has an exponential shape (approximately), is also shown. At $t = 200$ ps the shape of the distribution is somewhere

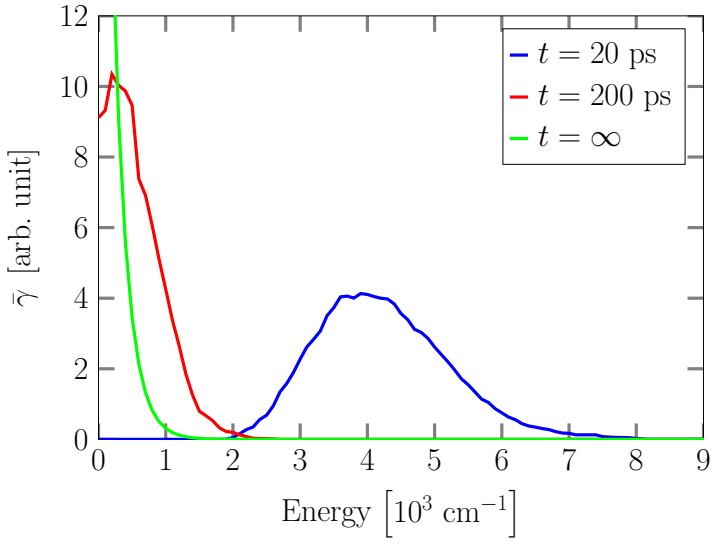

Figure 4.5: Vibrational energy distributions at $t = 20$ ps (blue) and $t = 200$ ps (red) averaged over 100 fs. The equilibrium vibrational energy distribution ($t = \infty$) based on an equilibrium MD simulation of a vibrating I_2 molecule in the electronic X-state at $T \approx 300$ K is also shown (green).

in between the Gaussian and the exponential distributions. Thus, the relaxation is not a thermally equilibrated cooling at any instant in the time interval [0 ps; 200 ps].

Here we note that the simple surface hopping model used in the nonequilibrium MD simulations gives rise to a faster vibrational energy relaxation than would be the case with a more realistic surface hopping model, in which the interaction potential of the iodine atoms can switch back and forth between the X- and the Π-state potential in the asymptotic region. Hence, the iodine atoms can recombine on the repulsive Π-state potential and subsequently dissociate again, which can occur several times before recombination on the X-state potential. Furthermore, the B-state potential is not included in the MD simulations as mentioned in Sec. 4.2. The I_2 molecule can be trapped in the potential well of the B-state shortly after the laser excitation but only for a short time (a lifetime of ~ 15 ps is observed in experiments, see Ref. [143]). The molecule will dissociate eventually due to the curve crossing of the B- and Π-state potentials. These deficiencies of the model are most likely of little importance on the 'long time' trend of the simulated vibrational energy relaxation, which is in very good agreement with experimental data.

4.3.2 I-I Pair Distribution Function

In Fig. 4.6 the time dependence of the I-I pair distribution function $\bar{\rho}(r,t)$ is shown, where $\bar{\rho}(r,t)$ is constructed from instantaneous I-I pair distribution functions $\rho(r,t)$ averaged over an interval of 100 fs for every 2 ps. The width of $\bar{\rho}(r,t)$ in r depends on the vibrational energy distribution $\bar{\gamma}(E,t)$, since the vibrational energy and the X-state potential determines the accessible range of r. Thus, the width of $\bar{\rho}(r,t)$ decreases in time while the ensemble of I_2 molecules based on the truncated set of MD simulations relaxes in the potential well (the average vibrational energy and the spread of $\bar{\gamma}(E,t)$ in energy decrease, and so does the accessible range of r). A fit to the average I-I distance $\langle r \rangle$ of a bi-exponential function

$$g(t) = A_r \exp(-t/\tau_1^r) + B_r \exp(-t/\tau_2^r) + 2.67\ \text{Å}\,, \tag{4.4}$$

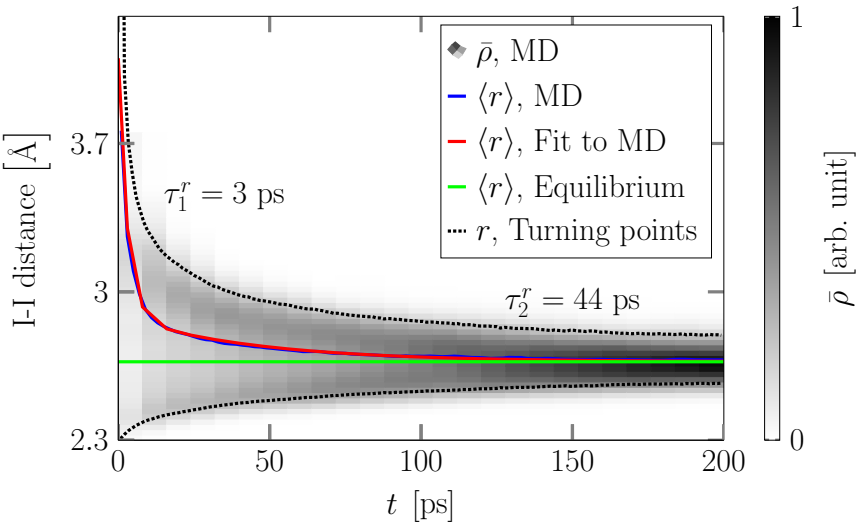

Figure 4.6: Time dependence of the I-I pair distribution function $\bar{\rho}(r,t)$. Fitting of a bi-exponential function (red) to the average I-I distance $\langle r \rangle$ (blue) yields the relaxation times $\tau_1^r = 3$ ps and $\tau_2^r = 44$ ps. The equilibrium I-I distance (green) and the classical turning points (black dotted lines) corresponding to the average vibrational energy are also shown.

gives the two relaxation times $\tau_1^r = 3$ ps and $\tau_2^r = 44$ ps ($A_r = 1.22$ Å and $B_r = 0.22$ Å), which are clearly different from τ_1^E and τ_2^E, respectively. The decrease in the average I-I distance relative to r_{eq} is ~ 97 % in the first 5 ps and ~ 3 % in the last 195 ps. Hence, a simple proportionality correspondence between $\langle E \rangle$ and $\langle r \rangle$ in terms of relaxation time or relative decrease in E and r does not exist. This can be understood by considering the change in the accessible range of r for a given change in vibrational energy E in the neighborhood of the dissociation limit $E \approx 12000$ cm^{-1} and the 'bottom' of the potential well, e.g. $E \approx 3000$ cm^{-1}, respectively (see Fig. 4.1). Clearly, the change in r is much larger near the dissociation limit, and therefore, the ratio $\tau_1^E/\tau_1^r = 3$ is larger than $\tau_2^E/\tau_2^r \approx 1.6$.

We observe that the major change in $\bar{\rho}(r,t)$ during the slow part of the relaxation is in the shape of the distribution. $\bar{\rho}(r,t)$ is bimodal with the two maxima close to the classical turning points of the X-state potential. This is clearly observed in Fig. 4.7, where $\bar{\rho}_{\text{MD}}(r,t)$ is shown for seven different times after the laser excitation with the base of the distributions at $\langle E \rangle(t)$ (each $\bar{\rho}_{\text{MD}}(r,t)$ has the same normalization constant). In Fig. 4.7 the corresponding experimental I-I pair distribution functions $\bar{\rho}_{\text{EXP}}(r,t)$ are also shown, where $\bar{\rho}_{\text{EXP}}(r,t)$ is based on data from time-resolved x-ray diffraction experiments using the 'time-slicing' scheme.[†] Clearly, the experimental and simulated I-I pair distribution functions are not identical, but the intervals, in which the distributions are nonzero, are somewhat comparable. If a bi-exponential function is fitted to the experimental average I-I distance, the two relaxation times are $\tau_{1,\text{ EXP}}^r = 16$ fs and $\tau_{1,\text{ EXP}}^r = 76$. Again, the agreement between the experimental and simulated results is not quantitative (in fact, the experimental relaxation times for the average I-I distance are fairly close to the simulated relaxation times for the average vibrational energy). Although, we can only establish a 'qualitative' agreement between the experimental and simulated results, where the bi-exponential relaxation is observed in both cases, the comparison still indicates that

[†]The author of this thesis has taken no part in carrying out the experiments.

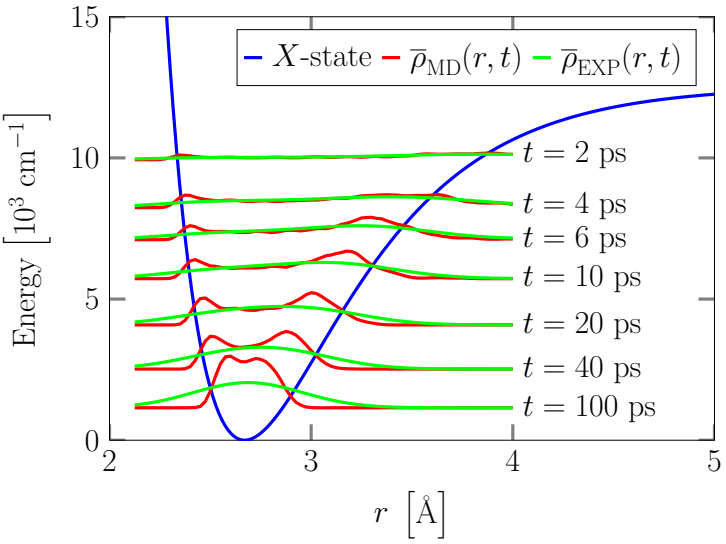

Figure 4.7: Potential energy curve corresponding to the X-state (blue), along with plots of the I-I pair distribution functions based on MD simulations $\bar{\rho}_{\mathrm{MD}}(r,t)$ (red) and x-ray experiments $\bar{\rho}_{\mathrm{EXP}}(r,t)$ (green) at seven times.

the novel time-slicing scheme is capable of enhancing the time-resolution of the x-ray experiments. Furthermore, a perfect quantitative agreement is rather unexpected due to the approximations used in the simulations, i.e., classical dynamics, an 'arbitrary' force field, the simple surface hopping model etc., and in the complex numerical analysis of the experimental data (see paper 2 in Preface).

Here we pause to comment on the two peaks of the simulated I-I pair distribution function $\bar{\rho}_{\mathrm{MD}}(r,t)$ in the neighborhood of the classical turning points. Although $\bar{\rho}_{\mathrm{MD}}(r,t)$ spans an interval in r larger than the classically allowed region, this is of course no quantum phenomenon: $\bar{\rho}_{\mathrm{MD}}(r,t)$ is averaged over 100 fs and plotted with the base at the average vibrational energy $\langle E\rangle(t)$, whereby the support of the distribution function can be larger than the classically allowed region corresponding to $\langle E\rangle(t)$.

Experimental results from time-resolved x-ray diffraction and optical spectroscopy can be compared, if we construct a good approximation to the I-I pair distribution function from the vibrational energy distribution. First we define the Hamiltonian function associated with the I_2 vibrational degree of freedom, $H(r,p) = p^2/(2\mu) + V_X(r)$, where p is the momentum (we neglect the potential energy functions due to interactions with the solvent molecules, which is a fairly good approximation for vibrational energies somewhat smaller than the dissociation energy, see Fig. 4.3(b)). In the microcanonical ensemble with vibrational energy E the I-I pair distribution function $\bar{\rho}_{\mathrm{MC}}(r,E)$ reads

$$\begin{aligned}\bar{\rho}_{\mathrm{MC}}(r,E) &= \int \mathrm{d}p\,\delta\left[H(r,p)-E\right]/\Omega\,,\ \text{where}\ \Omega = \int \mathrm{d}r \int \mathrm{d}p\,\delta\left[H(r,p)-E\right] \\ &\propto \int \mathrm{d}p\,\delta\left[p-p_E\right]\left|\frac{\mathrm{d}H}{\mathrm{d}p}\right|^{-1} \propto \int \mathrm{d}p\,\delta\left[p-p_E\right]|p|^{-1} \\ &= |p_E|^{-1} \propto \left(E - V_X(r_E)\right)^{-1/2}\,,\end{aligned} \tag{4.5}$$

where the phase space points (r_E, p_E) correspond to $H(r_E,p_E) = E$, and in the second line we have used the equality $\delta\left[p-p_E\right] = |\mathrm{d}H/\mathrm{d}p| \cdot \delta\left[H(r,p)-E\right]$.[152] In Fig. 4.8 we compare $\bar{\rho}_{\mathrm{MD}}(r,t)$ based on the MD simulations with the microcanonical I-I pair distri-

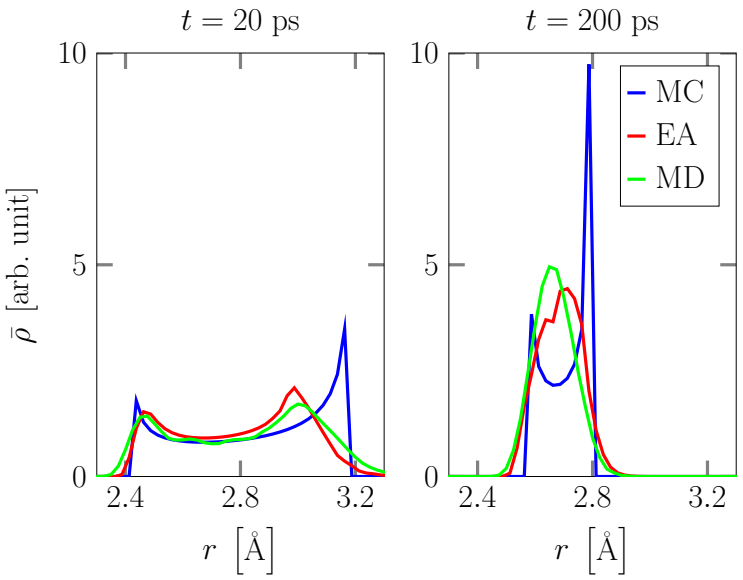

Figure 4.8: I-I pair distribution functions determined from the microcanonical ensemble (MC) averaged over the vibrational energy distribution (EA) as well as directly from MD simulations (MD) at times $t = 20$ ps and $t = 200$ ps.

bution function $\bar{\rho}_{\mathrm{MC}}(r, E)$ for $E = \langle E \rangle(t)$ at $t = 20$ ps and $t = 200$ ps. Clearly, the microcanonical I-I pair distribution function resembles the simulated $\bar{\rho}_{\mathrm{MD}}(r, t)$ only moderately well especially at 200 ps. This is due to the relatively large spread of $\bar{\gamma}(E, t)$ in energy and taking this into account by constructing energy averaged I-I pair distribution functions according to

$$\bar{\rho}_{\mathrm{EA}}(r, t) = \int \mathrm{d}E\, \bar{\gamma}(E, t) \bar{\rho}_{\mathrm{MC}}(r, E)\,, \tag{4.6}$$

the simulated $\bar{\rho}_{\mathrm{MD}}(r, t)$ is very well represented by $\bar{\rho}_{\mathrm{EA}}(r, t)$, see Fig. 4.8. Hence, the time-dependent I-I pair distribution function obtained from x-ray experiments can be compared to the time-dependent vibrational energy distribution determined in optical spectroscopy experiments using Eq. 4.6 with $\bar{\gamma}(E, t)$ replaced by the experimental vibrational energy distribution and substituting $\bar{\rho}_{\mathrm{MC}}$ by $(E - V_X(r_E))^{-1/2}$.

Finally, we address the issue of coherent motion during the vibrational energy relaxation. As mentioned before, vibrational coherence following the photodissociation of I_2 in liquids has been absent in classical MD simulations, but observed in experiments and MD simulations of the photodissociation of I_2 in solids.[52, 54, 55] To this end, we construct I-I pair distribution functions $\bar{\rho}_{\mathrm{MD}}(r, t)$, which are averaged over an interval of 20 fs. In Fig. 4.9 I-I pair distribution functions at six times around 10 ps are shown, and we see that the vibrational coherence is still detectable with a vibrational period of ~ 250 fs for ~ 8 % of the population oscillating between the classical turning points of the X-state potential. This partial coherent motion might be detectable with the use of free electron lasers, for which a femtosecond time resolution can be obtained.[23, 63, 64]

4.4 Conclusions

We have studied the photodissociation, subsequent recombination, and vibrational energy relaxation of iodine in carbon tetrachloride by means of classical nonequilibrium MD simulations. The chosen force field reproduces very well previous experimental results in

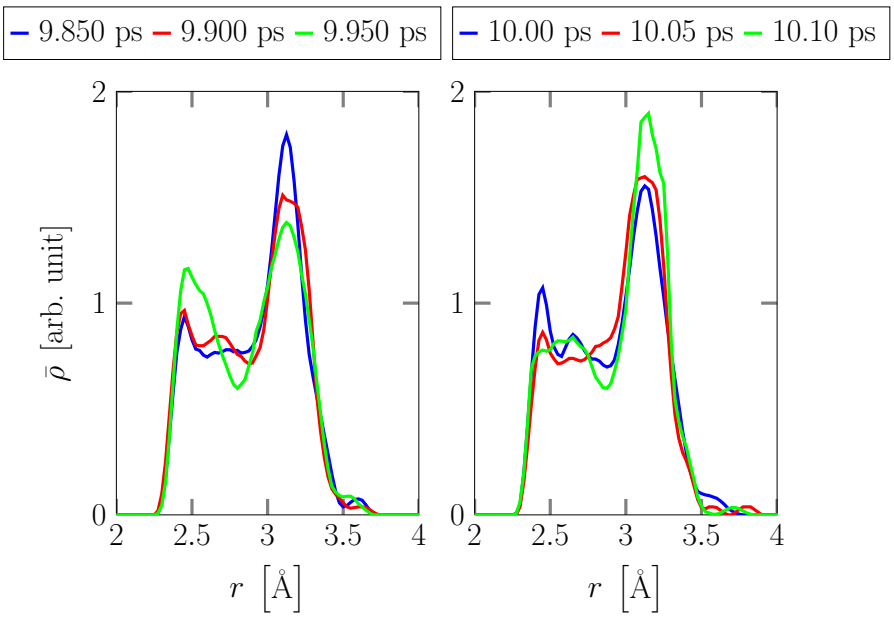

Figure 4.9: I-I pair distribution functions $\bar{\rho}_{\mathrm{MD}}(r,t)$ averaged over an interval of 20 fs at six times after the laser excitation. Vibrational coherence is still detectable at 10 ps after with $\sim$ 8 % of the population oscillating between the classical turning points of the X-state potential.

terms of the vibrational relaxation times, and hence, the force field appears suitable for studying this process. The vibrational energy relaxation of I_2 in the X-state follows a bi-exponential decay for both the average vibrational energy and the average I-I distance, albeit with different time constants. This bi-exponential decay is also observed in new time-resolved x-ray diffraction experiments using a novel time-slicing scheme. The simulated distribution of iodine distances is bimodal during most of the relaxation, but only moderately well described by a microcanonical density due to the relatively large spread in the vibrational energy. A good approximation to the I-I pair distribution function can be constructed by a simple procedure, in which an energy averaged distribution function is calculated using Eq. 4.6. Finally, some degree of vibrational coherence is observed, which has been absent for the vibrational energy relaxation of I_2 in other liquids. This partial coherent motion might be observed in future experiments.

Chapter 5

Ultrafast Librational Relaxation of H_2O in Liquid Water

The ultrafast librational (hindered rotational) relaxation of a rotationally excited H_2O molecule in pure liquid water is investigated by means of classical nonequilibrium MD simulations and a power and work analysis. This analysis allows the mechanism of the energy transfer from the excited H_2O to its water neighbors to be followed in molecular detail for this sub-100 fs process. We can thus observe which water molecules receive the energy and in which degrees of freedom. It is found that the dominant energy flow is to the four hydrogen-bonded water partners in the first hydration shell dominated by those partners' rotational motion in a reasonably symmetric fashion over the hydration shell. The minority component of the energy transfer to these neighboring waters' translational motion exhibits an asymmetry in energy reception between hydrogen bond-donating and -accepting water molecules. The variation of the energy flow characteristics with rotational axis, initial rotational energy excitation magnitude, method of excitation, and temperature is discussed. Finally, the relation of the nonequilibrium results to equilibrium time correlations is discussed.

5.1 Introduction

The dynamics of the librations (hindered rotations) of liquid water are not well understood despite their invocation as (a) important energy receptors in the pathways for energy relaxation of the water stretch and bend vibrational excitations [29, 67–75, 81–83, 153] and of some solute vibrations in aqueous solutions [65, 66], and (b) key participants in the rearrangements of the hydrogen bond networks of water and aqueous solutions.[76–80] In the present work we investigate some key aspects of water librational dynamics. In particular, we examine the relaxation time scale and molecular level energy transfer pathway of a rotationally excited H_2O molecule in liquid water via classical nonequilibrium MD simulations and a power and work formulation of energy transfer.

Much of the explicit scrutiny of pure liquid water libration dynamics is fairly recent and concerned with vibrational energy relaxation. Librational excitations in liquid water have been experimentally studied via femtosecond two-color infrared spectroscopy both directly and in connection with the energy transfer from excited water bend vibration.[81–83] For direct librational excitation the relaxation time scale is extremely short: sub-100 fs. Librations were also invoked as the major initial recipient of the excess water bend energy.[81–83] On the theoretical side, Hynes and coworkers have studied the bend relaxation mechanism.[72, 73, 75] This was shown via a power and work analysis [65, 154–157] to primarily involve a centrifugal coupling 2:1 Fermi resonance intramolecular energy transfer route from the bend to water rotation, leading to subsequent flow, primarily to

water librations in the first and second hydration shells of the initially bend-excited water molecule.[73] A very recent reformulation of the power and work description allowed the explicit identification of *which* water molecules (e.g. first hydration shell water accepting a hydrogen bond from the excited water) and degrees of freedom (rotation, translation) are key in accepting the energy.[75]

In the present work we apply the power and work formulation to the energy flow mechanism for a directly rotationally excited (rigid) water molecule, a process which has not received much previous theoretical attention primarily due to the comparatively limited experimental scrutiny [81–83] noted above. Prior theoretical work on this aspect includes those of nonequilibrium excited water rotation by Ingrosso *et al.* [72] and to a more restricted degree (in connection with water bend relaxation) by Rey *et al.* [73], as well as by Saito and coworkers.[158–161] These last authors initially focused on 2d spectroscopy [158–160] and more recently [161] on a combination of nonequilibrium MD simulations and kinetic equation modeling in a way complementary to ours. The present study extends the initial study of this process by Ingrosso *et al.* [72] (which did not exploit a power-work approach) in a number of important ways. First and foremost the specific identity of energy-accepting water molecules and degrees of freedom is found. In addition, a wider range of rotational excitation energies, temperatures and rotational axes is examined, and excitation via an external electric field is considered in addition to instantaneous excitation via an initial assignment of excess rotational energy. Furthermore, a comparison of the nonequilibrium results with a linear response perspective is given.

5.2 Theoretical Background

The work on the rotationally excited H_2O molecule done by the surrounding water molecules proves to be a useful quantity for examining the energy flow during the librational relaxation. This is often referred to as the work preformed by the 'solvent' on the central molecule. This work is the time-integrated power associated with the rotational kinetic energy of the central water molecule. A brief remark concerning nomenclature: Any rotation of a water molecule in the liquid is hindered, i.e. librational in character. Since we will be primarily concerned with rotational kinetic energy and a 'libration' actually refers to both kinetic and potential energy aspects, we will hereafter generally employ the terms 'rotation' or 'rotational'.

In the ensuing study, we apply the analysis of power and work contributions used previously by Whitnell, Wilson, and Hynes.[65, 66] A general discussion of the power-work formalism for energy relaxation can be found in Ref. [75].

5.2.1 Power Formula

In an isolated system of N rigid molecules the total energy E can be partitioned in kinetic energy $K = T + R$ (T denotes translational kinetic energy and R rotational kinetic energy) and potential energy U. As usual the kinetic energy of molecule i is given by a sum of contributions from each atom α_i

$$K_i = \sum_{\alpha_i} K_{\alpha_i} = \frac{1}{2} \sum_{\alpha_i} m_{\alpha_i} \mathbf{v}_{\alpha_i} \cdot \mathbf{v}_{\alpha_i} \,, \tag{5.1}$$

where m_{α_i} is the mass and $\mathbf{v}_{\alpha_i}$ is the velocity of atom α_i. The power of the kinetic energy of molecule i, i.e. the time derivative of K_i, reads

$$P_i \equiv \frac{\mathrm{d}K_i}{\mathrm{d}t} = \frac{1}{2} \sum_{\alpha_i} m_{\alpha_i} \left(\frac{\mathrm{d}\mathbf{v}_{\alpha_i}}{\mathrm{d}t} \cdot \mathbf{v}_{\alpha_i} + \mathbf{v}_{\alpha_i} \cdot \frac{\mathrm{d}\mathbf{v}_{\alpha_i}}{\mathrm{d}t} \right) = \sum_{\alpha_i} \mathbf{F}_{\alpha_i} \cdot \mathbf{v}_{\alpha_i} \,, \tag{5.2}$$

where $\mathbf{F}_{\alpha_i}$ is the force on atom α_i, which can be partitioned such that

$$P_i = \sum_{\alpha_i} \sum_{j} \sum_{\beta_j} \mathbf{F}_{\alpha_i,\beta_j} \cdot \mathbf{v}_{\alpha_i} \,, \tag{5.3}$$

with $\mathbf{F}_{\alpha_i,\beta_j}$ denoting the force on atom α_i due to the interaction with atom β_j. The term $\mathbf{F}_{\alpha_i,\beta_j} \cdot \mathbf{v}_{\alpha_i}$ is the change in kinetic energy of atom α_i due to the interaction with atom β_j. Since the increase/decrease in kinetic energy is equal to the decrease/increase in potential energy of the isolated system, we can write

$$\mathbf{F}_{\alpha_i,\beta_j} \cdot \mathbf{v}_{\alpha_i} + \mathbf{F}_{\beta_j,\alpha_i} \cdot \mathbf{v}_{\beta_j} = -\frac{\mathrm{d}U_{\alpha_i,\beta_j}}{\mathrm{d}t} \,, \tag{5.4}$$

where U_{α_i,β_j} denotes the potential energy of atom α_i and β_j due to their interaction.[162] In the rigid rotor approximation the summation over j does not include i, and we obtain

$$\begin{aligned} P_i &= -\sum_{\alpha_i} \sum_{j\neq i} \sum_{\beta_j} \left(\frac{\mathrm{d}U_{\alpha_i,\beta_j}}{\mathrm{d}t} + \mathbf{F}_{\beta_j,\alpha_i} \cdot \mathbf{v}_{\beta_j} \right) \\ &= -\sum_{j\neq i} \frac{\mathrm{d}U_{i,j}}{\mathrm{d}t} - \sum_{j\neq i} \sum_{\beta_j} \mathbf{F}_{\beta_j,i} \cdot \mathbf{v}_{\beta_j} \,, \end{aligned} \tag{5.5}$$

where $U_{i,j}$ is the potential energy of molecule i and j due to their interaction. Here $\mathbf{F}_{\beta_j,i}$ denotes the force on atom β_j due to the interaction with molecule i. We write the velocity vector $\mathbf{v}_{\beta_j}$ as

$$\mathbf{v}_{\beta_j} = \mathbf{v}_j + \boldsymbol{\omega}_j \times \mathbf{r}_{\beta_j} \,, \tag{5.6}$$

where $\mathbf{v}_j$ is the center of mass velocity of molecule j, $\boldsymbol{\omega}_j$ is the angular velocity of molecule j, and $\mathbf{r}_{\beta_j}$ is the position of atom β_j with respect to the center of mass of molecule j. This leads to

$$\begin{aligned} P_i &= -\sum_{j\neq i} \frac{\mathrm{d}U_{i,j}}{\mathrm{d}t} - \sum_{j\neq i} \sum_{\beta_j} \mathbf{F}_{\beta_j,i} \cdot \mathbf{v}_j - \sum_{j\neq i} \sum_{\beta_j} \mathbf{F}_{\beta_j,i} \cdot \boldsymbol{\omega}_j \times \mathbf{r}_{\beta_j} \\ &= -\sum_{j\neq i} \frac{\mathrm{d}U_{i,j}}{\mathrm{d}t} - \sum_{j\neq i} \mathbf{F}_{j,i} \cdot \mathbf{v}_j - \sum_{j\neq i} \sum_{\beta_j} \mathbf{r}_{\beta_j} \times \mathbf{F}_{\beta_j,i} \cdot \boldsymbol{\omega}_j \\ &= -\sum_{j\neq i} \frac{\mathrm{d}U_{i,j}}{\mathrm{d}t} - \sum_{j\neq i} \mathbf{F}_{j,i} \cdot \mathbf{v}_j - \sum_{j\neq i} \sum_{\beta_j} \boldsymbol{\tau}_{\beta_j,i} \cdot \boldsymbol{\omega}_j \\ &= -\sum_{j\neq i} \frac{\mathrm{d}U_{i,j}}{\mathrm{d}t} - \sum_{j\neq i} \mathbf{F}_{j,i} \cdot \mathbf{v}_j - \sum_{j\neq i} \boldsymbol{\tau}_{j,i} \cdot \boldsymbol{\omega}_j \,, \end{aligned} \tag{5.7}$$

where $\mathbf{F}_{j,i}$ is the force and $\boldsymbol{\tau}_{j,i}$ is the torque on molecule j (with respect to the center of mass) due to the interaction with molecule i. In the second line we use the equality

$$\mathbf{a} \cdot \mathbf{b} \times \mathbf{c} = \mathbf{c} \cdot \mathbf{a} \times \mathbf{b} = \mathbf{b} \cdot \mathbf{c} \times \mathbf{a} \,. \tag{5.8}$$

The kinetic energy of molecule i is partitioned in translational and rotational contributions

$$\begin{aligned} P_i &= P_i^T + P_i^R = \frac{\mathrm{d}T_i}{\mathrm{d}t} + P_i^R = \frac{\mathrm{d}}{\mathrm{d}t} \left(\frac{1}{2} m_i \mathbf{v}_i \cdot \mathbf{v}_i \right) + P_i^R \\ &= \mathbf{F}_i \cdot \mathbf{v}_i + P_i^R = \sum_{j\neq i} \mathbf{F}_{i,j} \cdot \mathbf{v}_i + P_i^R \,, \end{aligned} \tag{5.9}$$

and we obtain an expression for the power of the rotational kinetic energy of the ith molecule

$$\begin{aligned} P_i^R &= P_i - \sum_{j\neq i} \mathbf{F}_{i,j} \cdot \mathbf{v}_i \\ &= -\sum_{j\neq i} \frac{\mathrm{d}U_{i,j}}{\mathrm{d}t} - \sum_{j\neq i} \mathbf{F}_{i,j} \cdot \mathbf{v}_i - \sum_{j\neq i} \mathbf{F}_{j,i} \cdot \mathbf{v}_j - \sum_{j\neq i} \boldsymbol{\tau}_{j,i} \cdot \boldsymbol{\omega}_j \,, \end{aligned} \tag{5.10}$$

where the first term is the contribution to the power from the interaction potential energy between the ith molecule and the surrounding solvent molecules, the second and third terms are the translational kinetic energy contributions from the ith molecule and the surrounding solvent, respectively, and the fourth term is the rotational kinetic energy contribution from the solvent. A numerical check of the formula in Eq. 5.10 is to calculate the power of the rotational kinetic energy of the ith molecule from the expression

$$\begin{aligned} P_i^R \equiv \frac{\mathrm{d}R_i}{\mathrm{d}t} &= \frac{1}{2}\frac{\mathrm{d}}{\mathrm{d}t}\left(\boldsymbol{\omega}_i^{\mathrm{T}}\,\mathbf{I}_i\,\boldsymbol{\omega}_i\right) = \frac{1}{2}\frac{\mathrm{d}}{\mathrm{d}t}\left(\boldsymbol{\omega}_i^{\mathrm{T}}\mathbf{S}_i^{-1}\,\mathbf{S}_i\,\mathbf{I}_i\,\mathbf{S}_i^{-1}\,\mathbf{S}_i\boldsymbol{\omega}_i\right) = \frac{1}{2}\frac{\mathrm{d}}{\mathrm{d}t}\left(\tilde{\boldsymbol{\omega}}_i^{\mathrm{T}}\,\tilde{\mathbf{I}}_i\,\tilde{\boldsymbol{\omega}}_i\right) \\ &= \frac{1}{2}\left(\frac{\mathrm{d}\tilde{\boldsymbol{\omega}}_i^{\mathrm{T}}}{\mathrm{d}t}\,\tilde{\mathbf{I}}_i\,\tilde{\boldsymbol{\omega}}_i + \tilde{\boldsymbol{\omega}}_i^{\mathrm{T}}\,\tilde{\mathbf{I}}_i\,\frac{\mathrm{d}\tilde{\boldsymbol{\omega}}_i}{\mathrm{d}t}\right) = \tilde{\boldsymbol{\omega}}_i^{\mathrm{T}}\,\tilde{\boldsymbol{\tau}}_i = \tilde{\boldsymbol{\omega}}_i^{\mathrm{T}}\,\mathbf{S}_i\,\mathbf{S}_i^{-1}\,\tilde{\boldsymbol{\tau}}_i = \boldsymbol{\omega}_i^{\mathrm{T}}\,\boldsymbol{\tau}_i = \boldsymbol{\omega}_i \cdot \boldsymbol{\tau}_i \,, \end{aligned} \tag{5.11}$$

where $\mathbf{I}_i$ denotes the matrix representation of the moment of inertia tensor for the ith molecule with respect to the center of mass, and $\tilde{\mathbf{I}}_i = \mathbf{S}_i\,\mathbf{I}_i\,\mathbf{S}_i^{-1}$ is the matrix representation of the principal moment of inertia tensor (which is independent of time).[163] Here, $\boldsymbol{\omega}_i^{\mathrm{T}}$ denotes the transpose of $\boldsymbol{\omega}_i$, and we use that $\mathbf{S}_i$ is an orthogonal matrix ($\mathbf{S}_i^{-1} = \mathbf{S}_i^{\mathrm{T}}$).[164]

5.2.2 Work Formula

The work corresponding to the power in Eq. 5.10 is defined by

$$W_i(t) \equiv \int_{t_0}^{t} \mathrm{d}t'\, P_i^R(t') = \Delta R_i \,, \tag{5.12}$$

where $W_i(t)$ denotes the difference in rotational energy of the ith molecule between time t_0 and t, i.e. the transfer of excess rotational energy to the surrounding solvent molecules. The full expression for the work formula becomes

$$W_i = -\Delta U - \Delta T_i - W_T - W_R \,, \tag{5.13}$$

where the explicit expressions for the work terms are

$$\begin{aligned} W_T(t) &= \int_{t_0}^{t} \mathrm{d}t' \sum_{j\neq i} \mathbf{F}_{j,i}(t') \cdot \mathbf{v}_j(t') \\ W_R(t) &= \int_{t_0}^{t} \mathrm{d}t' \sum_{j\neq i} \boldsymbol{\tau}_{j,i}(t') \cdot \boldsymbol{\omega}_j(t') \,. \end{aligned} \tag{5.14}$$

The first term on the RHS in Eq. 5.13 is the difference in potential energy (due to interactions between the central water molecule and the surrounding solvent waters) between time t_0 and t, the second term is the change in translational kinetic energy of the central molecule, and the third and fourth terms are the energy transferred to the translational and rotational degrees of freedom of the surrounding water solvent, respectively. The key point is that we can hereby determine to which molecules and degrees of freedom of the solvent the excess rotational kinetic energy is transferred.

Finally, in order to obtain a detailed picture of the pathway of the energy flow, the solvent is divided into hydration shells around the central excited water molecule. The 1st

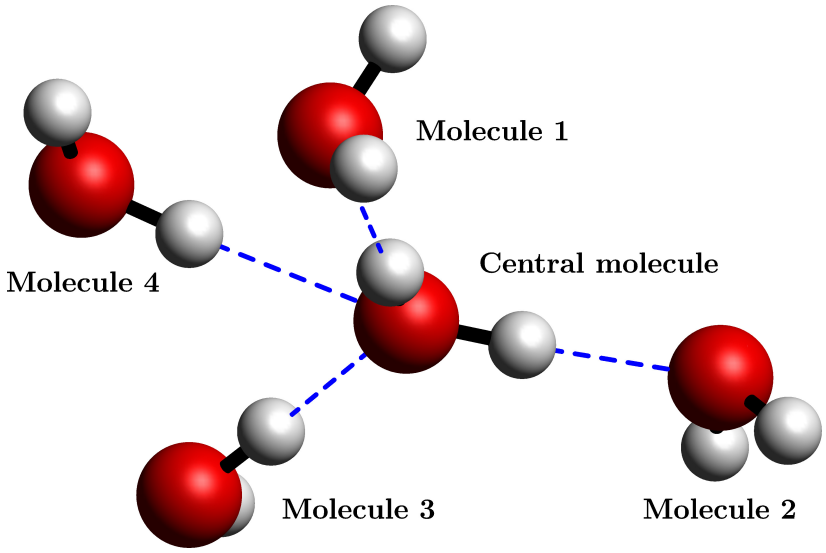

(a) First hydration shell molecules.

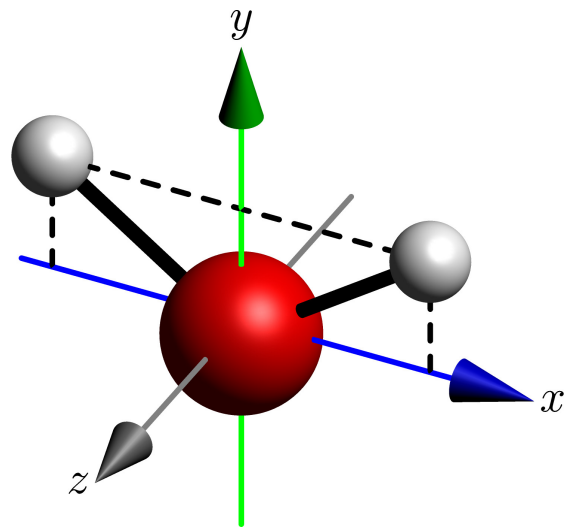

(b) Principal axes of a rigid H_2O molecule.

Figure 5.1: (a) The central water molecule is hydrogen bonded to four water molecules in its first hydration shell. Molecules 1 and 2 are receiving H-bonds from the central H_2O molecule, and molecules 3 and 4 are donating H-bonds to the central molecule. (b) The principal axes for a rigid H_2O molecule. The corresponding moments of inertia are $I_{xx} \cong 0.6$, $I_{yy} \cong 1.3$, and $I_{zz} \cong 1.9$ (in amu·Å^2).

shell corresponds to the four nearest water molecules, where two are receiving hydrogen (H)-bonds from the central water, and two are donating H-bonds, see Fig. 5.1(a). The 2nd shell consists of all water molecules except the four nearest within a radial distance of ~ 5.7 Å with respect to the central molecule. Under equilibrium conditions at $T \sim 300$ K the 2nd shell includes 21.6 molecules on average.

We pause to remark that there are substantial differences between our approach and a recently reported alternate nonequilibrium approach.[158–161] In that work the entire

sample is excited and total excess energies are followed, with most information obtained from a fitting to a phenomenological model. Although providing neither the detailed molecule-to-molecule nor the mode-to-mode energy fluxes determined in the present work, this alternate perspective is a valuable approach which provides interesting information on the excitation frequency dependence of energy flow consistent with our results in Sec. 5.4.5.

5.3 Computational Methods

The classical MD simulations are carried out with an in-house code, which applies cubic periodic boundary conditions and the minimum image convention for a system of 216 H_2O molecules. The atomic equations of motion are solved with the Velocity-Verlet algorithm [100] using a time step of 0.5 fs, and the intermolecular forces are described by the SPC/E model [165]. The length of the simulation box is $L \approx 18.6$ Å corresponding to the experimental value of the density ($\rho = 0.998$ g/cm^3) at $T \approx 300$ K, and the cutoff distance is $L/2$.[166] The Ewald summation correction for the Coulomb forces has been included with $\alpha = 5L$ and $n^2_{\max} = 25$.[108] The water molecules are kept rigid during the simulations with the RATTLE algorithm [112] (with a relative accuracy of 10^{-7}), and the Nosé-Hoover thermostat [113, 114] is used for the initial thermal equilibration.

5.3.1 Initial Conditions

In order to obtain a statistical picture of the librational relaxation process, a set of equilibrated initial conditions of the system is produced. The setup of the simulation box corresponds to a simple cubic lattice with a water molecule at each lattice point, and the orientations of the molecules are the same. The molecular linear and angular velocities are chosen from Maxwell-Boltzmann distributions at $T = 300$ K.[31] This setup corresponds to a very repulsive state, and the temperature increases significantly within 2 ps of the propagation. The Nosé-Hoover thermostat is turned on to correct for the increase in the temperature, and after 500 ps the system is equilibrated at $T \approx 300$ K. The thermostat is then turned off, and the propagation is continued under NVE-conditions for 100 ps.

A total number of 20000 initial conditions is produced from a 100 ns NVE-simulation run, where snapshots of phase space points are saved every 5 ps. After the atomic positions and velocities are saved, new random molecular linear and angular velocities at $T = 300$ K are chosen for each molecule. With this procedure, the initial conditions correspond to a canonical ensemble at $T \approx 300$ K with a standard deviation of ~ 9 K. Similar procedures are followed for the other temperatures examined (the standard deviations of the temperature fluctuations are ~ 10 K and ~ 11 K for $T \approx 325$ K and $T \approx 350$ K, respectively).

5.3.2 Nonequilibrium MD Simulations

Based on the initial conditions, nonequilibrium MD (NEMD) simulations are carried out with instantaneous rotational excitations of the central water molecule. We commence with the case where an energy of $E_{\text{rot}} = 5$ kcal/mol is added to the rotation with respect to the principal x-axis of the central molecule. This energy choice corresponds to approximately one H_2O bend quantum.[72] It is of interest in connection with the bend relaxation problem and is also useful in highlighting aspects of the energy flow. To investigate if the librational relaxation is dependent on the chosen value of 5 kcal/mol for the rotational excitation energy, we carry out simulations where the excitation energy is varied from 1–15 kcal/mol. Special attention is also given to the 1 kcal/mol case as an illustration of rotational excitation in the thermal range.

The angular velocity component corresponding to the excitation is found via $\omega_x = \sqrt{2E_{\rm rot}/I_{xx}}$, where I_{xx} is the principal moment of inertia element associated with the x-axis. The value of ω_x is added to the existing value of the angular velocity component, which can be both negative and positive. Hence, the initial rotational energy of the central molecule is not equal to, for example, 5 kcal/mol (plus the equilibrium value) for each trajectory, but can be both less than or greater than 5 kcal/mol (plus the equilibrium value). But on average the excitation energy is 5 kcal/mol. This prescription differs from that of Ingrosso *et al.* [72], where the central water molecule is given an excess rotational kinetic energy. Therefore, the initial rotational kinetic energy is the excitation energy plus the equilibrium value for each trajectory. The system is then propagated until the rotational relaxation of the excited water molecule is completed. The same calculations are carried out for separate excitations with respect to the principal y- and z-axes, see Fig. 5.1(b).

The librational energy relaxation is found to proceed very rapidly, and it is possible that the width of an experimental optical excitation pulse might influence the decay time. In order to examine this issue, the rotational excitation is also carried out via an external time-dependent electric field. The details of these simulations are presented together with the results in Sec. 5.4.5. Finally, the NEMD simulations were checked for finite-size effects by comparing results for a system of 64 H_2O molecules with those for systems of 216 and 343 H_2O molecules. The librational energy decay shows no significant difference for the three systems, and we choose to base all presented MD simulation results on the 216 H_2O molecule system.

5.3.3 Test of the Implementation of the Power Formula

Here, we show a test result for the numerical implementation of the power formula in Eq. 5.10. In the code for classical MD simulations of liquid water the calculation of the time derivative of the interaction potential energy $U_{C,j}(t)$ is carried out using the 'five point' formula [167]

$$\frac{{\rm d}U_{C,j}}{{\rm d}t} \approx \frac{-U_{C,j}(t+2\delta t) + 8U_{C,j}(t+\delta t) - 8U_{C,j}(t-\delta t) + U_{C,j}(t-2\delta t)}{12\delta t}\,, \qquad (5.15)$$

where δt denotes the time step of the propagation of the system. In Fig. 5.2 the power of the rotational kinetic energy of the central molecule P_C^R as a function of time for an equilibrium simulation is shown, where the power is calculated using both Eq. 5.10 and Eq. 5.11, and the obtained results are clearly identical. Several other numerical test are successfully carried out, from which we conclude that the numerical implementation of the power formula in Eq. 5.10 is correct.

5.4 Simulation Results and Discussion

5.4.1 Rotational Kinetic Energy Relaxation

We begin with simulation results for the decay to equilibrium of the rotational kinetic energy for the initially rotationally excited central water molecule. Fig. 5.3(a) displays several examples of the time dependence of the rotational kinetic energy (of 5 kcal/mol) of the central molecule for three of the NEMD trajectories in which the instantaneous rotational excitation is with respect to the principal x-axis. These different trajectory results give an impression of the differing initial rotational energies as explained in Sec. 5.3.2, and of an oscillatory character at least for the shortest times where there is a qualitative agreement for all three trajectories.

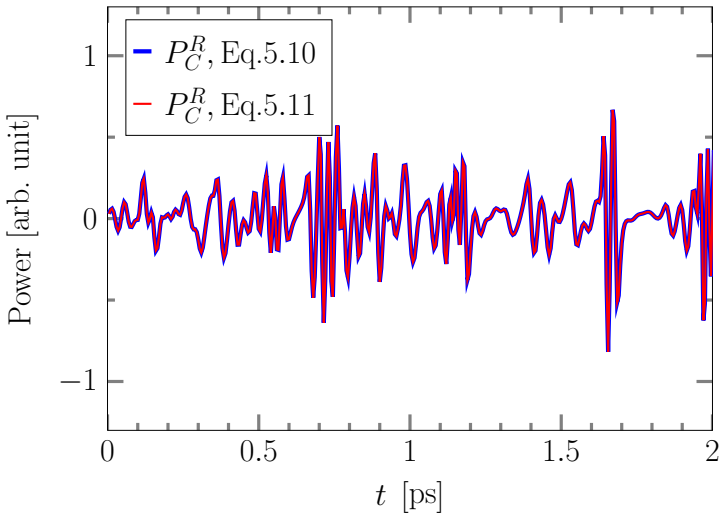

Figure 5.2: Power of the rotational kinetic energy of the central molecule P_C^R as a function of time for an equilibrium simulation. The power is calculated using both Eq. 5.10 and Eq. 5.11, and the results are clearly identical.

The average rotational kinetic energy of the central water molecule based on 20000 NEMD trajectories is shown in Fig. 5.3(b). The first point of importance is that the main portion of the excitation energy is lost within $\sim$ 100 fs, which agrees with the decay behavior for librational excitation obtained by ultrafast IR experiments.[72, 83] Second, a single oscillation remains in this average decay. The local maximum in the rotational kinetic energy at $t \sim 25$ fs associated with this oscillation indicates clearly, that most if not all NEMD trajectories are qualitatively quite similar with respect to the time evolution of the rotational kinetic energy during the first $\sim$ 25 fs after the excitation, and some degree of rotational coherence is maintained during that time interval. This initial oscillation in the average rotational kinetic energy decay is associated with rotational caging, in which the angular momentum is reversed due to the restraining torques of the surrounding water molecules. This is established in the Sec. 5.4.6, which extends and generalizes the similar identification made for the total angular momentum in Ingrosso *et al.* [72].

The behavior just discussed is not restricted to the rotational excitation with respect to the principal x-axis. Fig. 5.3(c) shows the excited water molecule's rotational kinetic energy as a function of time for excitation with respect to the principal x-, y-, and z-axes. The time evolutions are quite similar: The rotational kinetic energy drops from $\sim$ 6 kcal/mol to $\sim$ 1.5 kcal/mol within $\sim$ 15 fs. This energy then increases to $\sim$ 2.5 kcal/mol within the next $\sim$ 15 fs in the course of the rotational caging oscillation and completes the remaining small decline to the equilibrium value within $\sim$ 200 fs. In view of this similarity, we will in the following focus on the results for the principal x-axis rotational excitation and refer to the other axes results for particular points of interest.

5.4.2 Work Analysis

The various terms in Eq. 5.13 for the work on the excited water molecule rotation, which are defined in detail below that equation, are plotted as functions of time in Fig. 5.4. After 2 ps (and importantly to a significant degree already within $\sim$ 250 fs) $\sim$ 90 % ($\overline{W_R}$) of the excitation energy has been transferred to the rotational degrees of freedom of

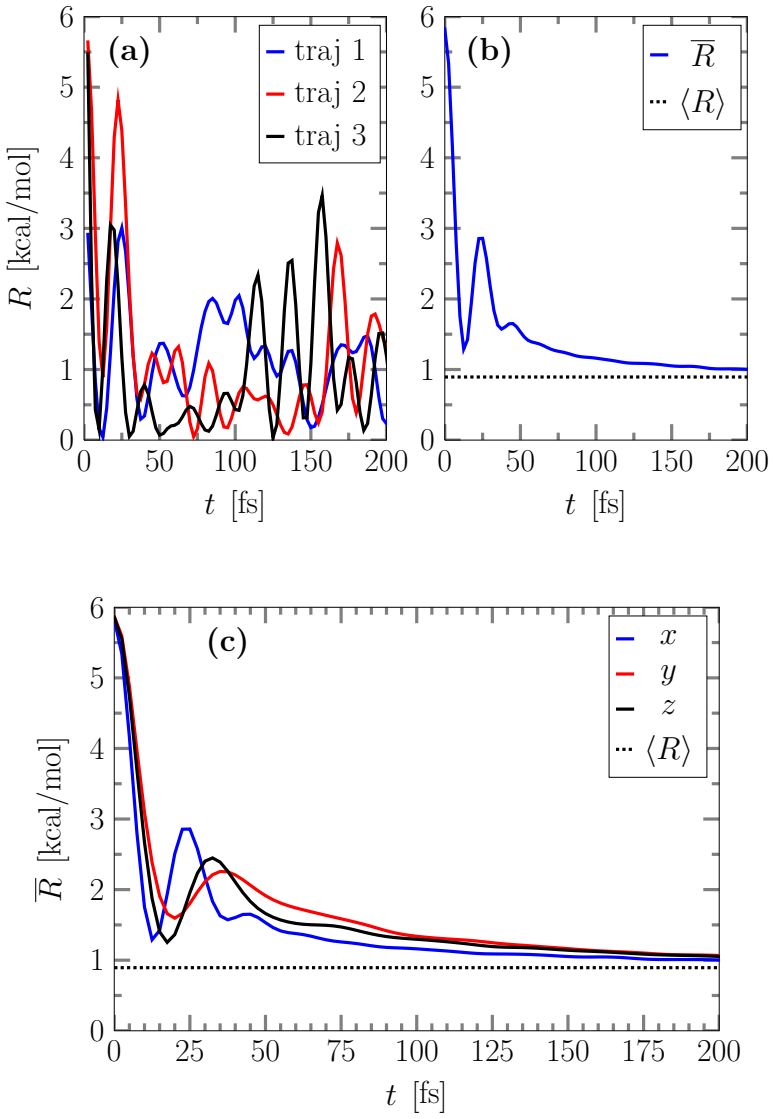

Figure 5.3: (a) Nonequilibrium rotational kinetic energy R of the central water molecule as a function of time for instantaneous 5 kcal/mol rotational excitation with respect to the principal x-axis (for three of the NEMD trajectories), and (b) the corresponding nonequilibrium average rotational kinetic energy $\overline{R}$ based on 20000 NEMD trajectories. The equilibrium average rotational kinetic energy $\langle R \rangle \approx 0.894$ kcal/mol ($3N_{\mathrm{A}}k_{\mathrm{B}}T/2$) is also shown. (c) Nonequilibrium average rotational kinetic energy $\overline{R}$ of the central water molecule as a function of time for 5 kcal/mol rotational excitation with respect to the principal x-, y-, and z-axes. A similar figure was reported by Ingrosso *et al.* [72].

the surrounding water molecules, and the remaining ~ 10 % ($\overline{W_T}$) is transferred to their translational degrees of freedom. The y- and z-axis excitation results are similar with slightly more transfer to translation (see Tab. 5.1). This dominance of transfer of excess rotational kinetic energy to water solvent rotation is consistent with the central molecule's greater rotational frequency overlap with water's librational spectrum ($\sim$ 400-800 cm^{-1}) than with its translational spectrum ($\lesssim$ 200 cm^{-1}).[78, 168] It is also in good agreement with the results reported by Rey and Hynes [75] for the energy transfer from a water

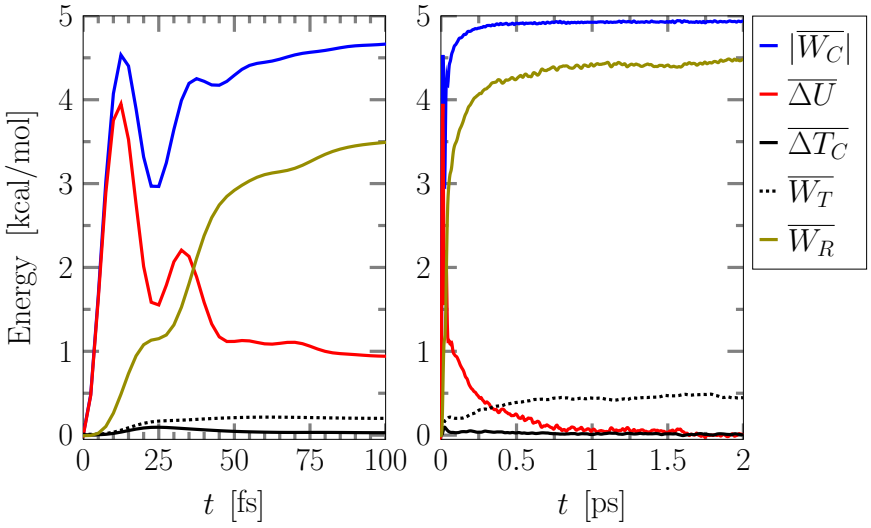

Figure 5.4: Nonequilibrium average work and energy terms for 5 kcal/mol rotational excitation of the central water molecule with respect to the principal x-axis. Shown are the absolute value of the work on the rotational degrees of freedom $|\overline{W_C}|$ of the central rotationally excited water molecule (equal to the magnitude of the molecule's energy loss), the difference in potential energy $\overline{\Delta U}$ between time 0 and t, and the difference in translational kinetic energy $\overline{\Delta T_C}$ of the central water molecule, and the work on the translational $\overline{W_T}$, and the rotational degrees of freedom $\overline{W_R}$ of the surrounding waters.

molecule rotationally excited via the Fermi resonance-induced energy transfer from the bend excitation of that molecule. This core result concerning the dominance of transfer to rotation is also consistent with the conclusions of Saito and coworkers.[161]. Their phenomenological model using fitted lifetimes close to those of a similar model in Ref. [73] is consistent with a fast energy transfer between rotational modes. In addition, these authors observe, as in the present work, a slow increase of excess translational energy of the entire sample, a feature also found in Ref. [72].

The time interval in which the changes in the terms are most pronounced is from 0–0.1 ps. For $t \sim 2$ ps all the terms have reached asymptotically stable values, with the magnitude of the work on the excited water molecule rotation $|\overline{W_C}|$, which is the negative of the molecule's rotational kinetic energy loss, having plateau'd long before this. The first significant increase of $|\overline{W_C}|$ within the first ~ 15 fs is a decrease in the central water's rotational kinetic energy in agreement with the sharp decrease in the excited water's rotational kinetic energy for the three NEMD trajectories in Fig. 5.3(a) within the same interval. This decrease is clearly due to an increase in $\overline{\Delta U}$, the potential energy of its interaction with the remaining 'solvent' water molecules. This conversion is of course expected, since the network of intermolecular H-bonds is distorted when the central molecule starts to rotate more intensely.

In a feature related to the average rotational kinetic energy in Fig. 5.3(b), Fig. 5.4 shows that at time $t \sim 15$ fs, both $|\overline{W_C}|$ and $\overline{\Delta U}$ exhibit an oscillatory character. The rotation with respect to the x-axis is on average reversed due to the repulsive torques from the distorted network of H-bonds (the rotational caging described above), and the molecule begins a 'backward' rotation with respect to the principal x-axis, reducing the repulsion (see also Sec. 5.4.6). Hence, the rotational kinetic energy of the central molecule

transiently increases and decreases in the time interval 15-30 fs due to a decrease and increase in the interaction potential energy due to the completion of the cage oscillation. After this interval any coherence is largely lost, and the central water's rotational kinetic energy decreases as does the potential energy.

Turning our attention now to the surrounding water molecules, the work on their translational and rotational degrees of freedom starts to build up significantly after ~ 10 fs dominated by the work on rotation. This slight time delay with respect to the buildup of potential energy, is readily understood: The only path for energy transfer between the molecules is via the intermolecular interactions, i.e. the intermolecular forces and torques deriving from the potential energy. (One should also note the transfer to the translational kinetic energy of the excited central molecule, which subsequently decays). The only other marked feature is the slight pause in the steady increase in the solvent rotational kinetic energy in the midst of the rotational cage oscillation, after which there is an incoherent increase of this energy.

5.4.3 Energy and Temperature Dependence

We now investigate the dependence of the rotational energy relaxation on the excitation energy and the temperature. Fig. 5.5(a) displays the normalized excess rotational kinetic energy, $\overline{R}(t) - \langle R \rangle$, of the central water molecule for four different excitation energies (all the excitations are with respect to the x-axis). While the very initial decay to ~ 0.1 remains very nearly the same, the excitation energy affects both the position and amplitude of the first local maximum, the former being shifted to slightly longer times and the latter decreasing somewhat as the energy increases. A further effect is that the second local maximum vanishes for the largest excitation energies 10–15 kcal/mol, i.e. the degree of rotational coherence is decreased. On the other hand, the long-time behaviour, i.e. post ~ 50 fs, of the decay of the rotational kinetic energy is not significantly affected. Further, for all the excitation energies considered, we find that ~ 85–90 % of the excess rotational kinetic energy is transferred to the rotational degrees of freedom of the solvent waters indicating that the energy pathway is approximately independent of the excitation energy, a result confirmed by calculations analogous to the lower energy results in Fig. 5.4.

The normalized excess rotational kinetic energy of the central molecule for three different temperatures is shown in Fig. 5.5(b). The positions of the local extrema are not affected by the temperature, but their amplitudes and the degree of rotational coherence are decreased slightly. The very modest magnitudes of the temperature effects here are consistent with the much smaller magnitude of initial water rotational kinetic energy compared to the three higher excitation energy situations in Fig. 5.5(a).

Finally, these general features of the x-axis excitation results are largely axis-independent. A similar dependence on the excitation energy and the temperature for instantaneous excitation with respect to the water molecule's y- and z-axes is found as shown in the Appendix.

5.4.4 Hydration Shell Analysis

In the preceding section, we have established that the energy flow for the librational relaxation is strongly dominated by the transfer to the rotational degrees of freedom of the water molecules surrounding the excited water molecule. We now examine in detail the energy transfer to the excited water molecule's hydration shells. The contributions from the 1st shell, the 2nd shell, and the remainder of the solvent to the work on the rotational degrees of freedom $|\overline{W_C}|$ of the central excited molecule (magnitude of the rotational kinetic energy loss) are shown in Fig. 5.6(a) (see also Tab. 5.1, first column entries $\overline{W_C}_{\mathrm{1st/2nd}}$).

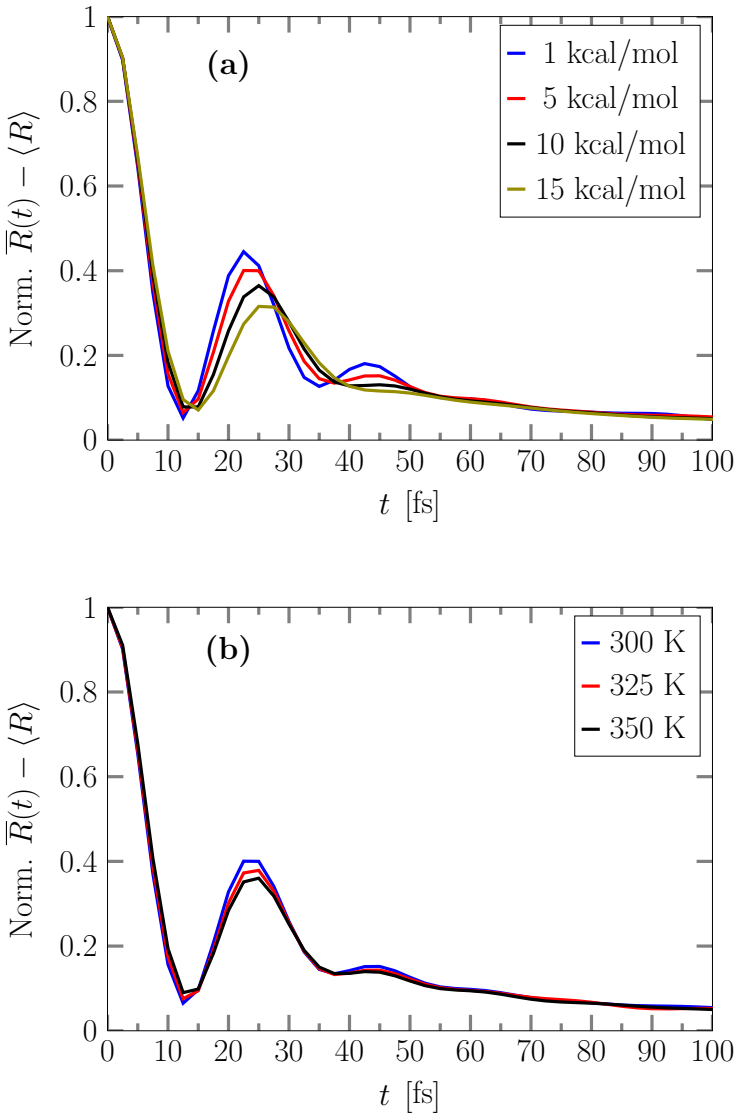

Figure 5.5: (a) Normalized nonequilibrium average excess rotational kinetic energy of the central water molecule for four different excitation energies. The instantaneous excitation is with respect to the principal x-axis. (b) Normalized nonequilibrium average excess rotational kinetic energy for three different temperatures, where the 1 kcal/mol instantaneous excitation of the central water is with respect to the principal x-axis.

The 1st shell, 2nd shell, and remaining contributions are approximately 75 %, 22 %, and 3 %, respectively, for x-axis excitation, with slightly higher 1st shell dominance for the remaining axis excitations (see Tab. 5.1 entries $\overline{W_{C\,\mathrm{1st/2nd}}}$). The main contributions come from transfer especially to the 1st shell and to a lesser degree to the 2nd shell, a conclusion also reached by Rey and Hynes for the different case of water bend vibrational relaxation.[75] Clearly, the librational relaxation is mainly a local process involving the first two hydration shells.

Since energy transfer to the 1st hydration shell was just shown to be dominant, it is interesting to determine how this work contribution is distributed among the hydrogen-bonded molecules. To this end, Fig. 5.6(b) compares the work contributions from the water molecules accepting H-bonds from the rotationally excited water (molecules 1 and 2

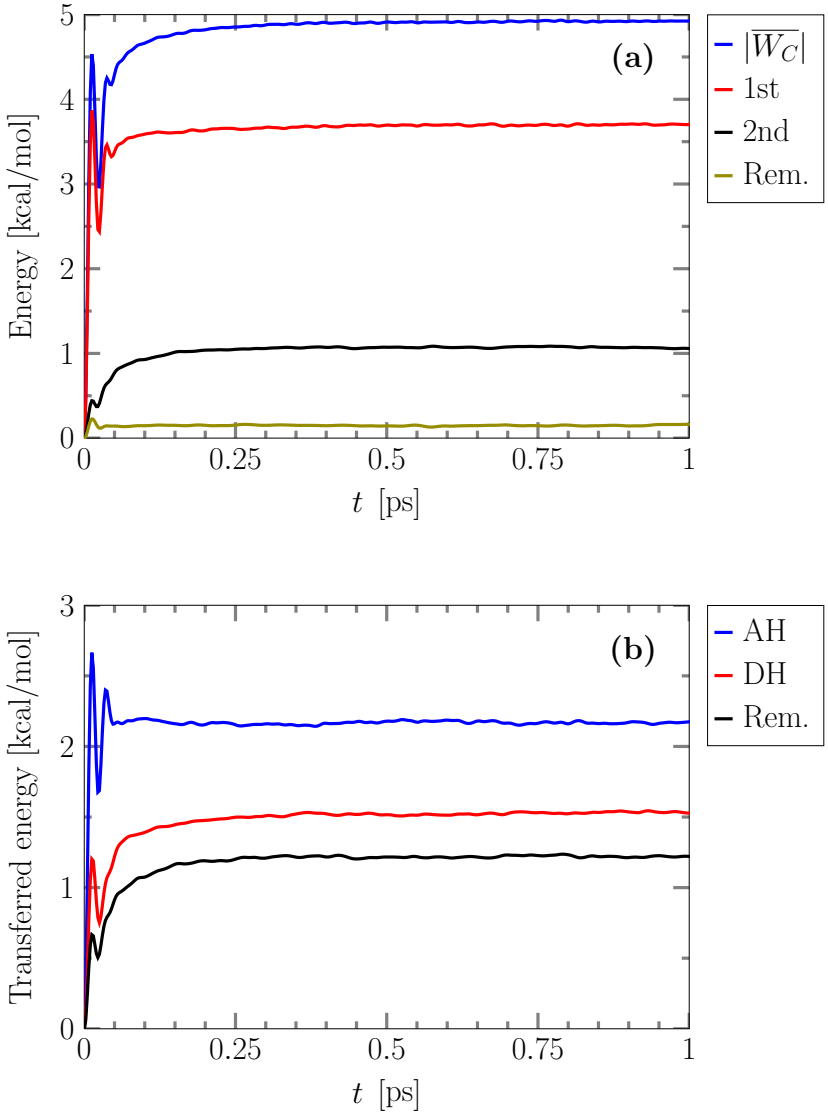

Figure 5.6: (a) Magnitude of the nonequilibrium average work $|\overline{W_C}|$ on the central water molecule, the work contribution from the 1st hydration shell water molecules, the work contribution from the 2nd hydration shell water molecules, and the work contribution from the remaining water molecules (Rem.). (b) Work contribution from the molecules accepting H-bonds (AH), the work contribution from the molecules donating H-bonds (DH), and the work contribution from the remaining water molecules (Rem.). Note that AH and DH waters are by definition 1st shell waters, see Fig. 5.1(a).

in Fig. 5.1(a)), the work contribution from those molecules donating H-bonds (molecules 3 and 4 in Fig. 5.1(a)), and the work contribution from all other water molecules which are primarily in the 2nd hydration shell). Since the H-bond-accepting and -donating waters are by definition 1st shell waters, we see again that most of the excess rotational kinetic energy ($\sim$ 75 % for x-axis excitation) is transferred to the water molecules in the 1st hydration shell. The new information is that the energy transfer to water molecules accepting H-bonds (AH, molecules 1,2) dominates over energy transfer to H-bond donating waters (DH, molecules 3,4). However, the magnitude of this dominance varies noticeably with the axis excitation, as indicated by the $\overline{W_{C12/34}}$ entries of Tab. 5.1: 1.5, 1.9, and 1.2

Table 5.1: Work contributions in percentages at time $t = 2$ ps[a]

	x-axis	y-axis	z-axis	I_0[b]
$\overline{W_R}$ [%]	91	82	84	91
$\overline{W_T}$ [%]	9	17	16	9
$\overline{\Delta U}$ [%]	0	1	0	0
$\overline{W_C}_{\mathrm{1st/2nd}}$[c] [%]	75/22	85/13	85/13	79/18
$\overline{W_R}_{\mathrm{1st/2nd}}$ [%]	65/23	67/15	67/14	68/20
$\overline{W_T}_{\mathrm{1st/2nd}}$ [%]	9/ 1	15/ 2	15/ 2	10/ 1
$\overline{\Delta U}_{\mathrm{1st/2nd}}$[d] [%]	1/ -2	3/ -4	3/ -3	1/ -3
$\overline{W_C}_{12/34}$[e] [%]	45/30	56/29	46/39	45/35
$\overline{W_R}_{12/34}$ [%]	32/32	33/32	27/40	32/37
$\overline{W_T}_{12/34}$ [%]	8/ 1	15/ 1	12/ 3	8/ 2
$\overline{\Delta U}_{12/34}$[d] [%]	5/ -3	8/ -4	7/ -4	5/ -4

[a] While the work $\overline{W_C}$ on the central excited molecule has plateau'd by 1 ps (see Fig. 5.4), the values of its various contributions given by Eq. 5.13 are stabilized by 2 ps, which has determined this choice for the values in the Table.
[b] Time-dependent, spatially-independent electric field excitation with a carrier frequency of 700 cm^{-1}.
[c] 1st and 2nd hydration shells.
[d] The negative sign indicates that $\overline{\Delta U}$ is negative.
[e] Molecules 1 and 2 accept H-bonds and molecules 3 and 4 donate H-bonds to the central water (see Fig. 5.1(a)). Since these are 1st hydration shell waters, the percentages given, e.g. for $\overline{W_C}_{12/34}$ in the x-axis excitation case, sum (within error bars) to the 1st hydration shell value in $\overline{W_C}_{\mathrm{1st/2nd}}$ in the x-axis column. The same relation applies to $\overline{W_R}_{12/34}$ and the 1st hydration shell value in $\overline{W_R}_{\mathrm{1st/2nd}}$ etc.

for the x-, y-, and z-axis excitations, respectively.

We now need to connect these results to the previously established (Fig. 5.4 for x-axis excitation) dominance of transfer to the rotation over that to translation of the water molecules surrounding the excited water, a feature quantified by the $\overline{W_R} = 91$ % and $\overline{W_T} = 9$ % values in Tab. 5.1, i.e. a factor of ~ 10. This dominance drops to about a factor of ~ 5 for the y- and z-excitation cases.

In any case, the results just cited do not identify *which* waters receive the energy. To answer this question, we turn to other results in Tab. 5.1. Before entering into the detailed results, it will prove useful to review several points. The first concerns the relationships of the work done *on* the central water and the work done *by* that water. We recall Eq. 5.13, here repeated for convenience,

$$W_C = -\Delta U - \Delta T_C - W_T - W_R \,. \tag{5.16}$$

When the potential energy change contribution here is small, it can be ignored. This is

the case for the total contributions in Eq. 5.16, as seen both in Fig. 5.4 at 2 ps and for the first three rows of Tab. 5.1. In addition, the reader is advised to note the summation constraints for Tab. 5.1 as indicated in the footnotes there.

The second cluster of these results, on the partitioning between the first and second shells, indicates first via $\overline{W_{C}}_{1st/2nd}$ that the 97 % energy transferred to these shells is partitioned as 75 % to the 1st shell and 22 % to the 2nd shell. From the $\overline{W_{R}}_{1st/2nd}$ and $\overline{W_{T}}_{1st/2nd}$ values we see that rotation dominates over translation in the contributing fractions 65/75 vs 9/75 in the 1st shell and 23/22 vs 1/22 (which are one and zero within error bars) in the 2nd shell. The $\overline{W_{C}}_{12/34}$ value indicates that the 75 % energy transferred to the 1st hydration shell is partitioned as 45/75 for the AH waters and 30/75 for the DH waters, i.e. the AH waters 1,2 are more effective in accepting energy from the excited water. But how is this efficiency related to which motions are involved? From the $\overline{W_{R}}_{12/34}$ and $\overline{W_{T}}_{12/34}$ values, we see by a vertical comparison that both the H-bond acceptors and donors are preferentially rotationally, rather than translationally, excited by energy transfer from the excited water molecule: For the AH waters in the ratio 32/8 and for the DH waters in the ratio 32/1. This comparison also indicates that the AH waters 1,2 are noticeably more effective than the DH waters in the minority component translational excitation.

The results just discussed can be compared with those for the transfer of the excited water's rotational kinetic energy to the translational degrees of freedom of the 1st hydration shell waters. This transfer is partitioned with $\sim$ 90 % for the water molecules accepting H-bonds, and the remaining $\sim$ 10 % for the molecules donating H-bonds (see first column of Tab. 5.1). This huge difference can be explained very simply, since any hindered rotation around the center of mass of a water molecule does not change the position of the oxygen atom significantly, whereas the positions of the hydrogen atoms are changing more dramatically. Hence, the H-bonds are distorted to a large extend for the molecules accepting H-bonds, and they have to 'translate' accordingly.

5.4.5 Rotational Excitation via an External Electric Field

Since the librational relaxation occurs on the timescale of tens of femtoseconds, an ultrashort experimental optical excitation pulse duration could certainly influence aspects of the relaxation. In order to explore this issue, we compare some of our instantaneous excitation results with a rotational excitation carried out by coupling the point charges of the central water molecule to a linear polarized time-dependent electric field with no spatial dependence. This coupling is introduced by adding the term $-\boldsymbol{\mu}\cdot\mathbf{E}(t)$ to the Hamiltonian, where $\boldsymbol{\mu}$ is the dipole moment of the central water, and $\mathbf{E}(t)$ is the time-dependent electric field. The electric field is taken to have a Gaussian shape with FWHM = 50 fs and is centered at $t = 100$ fs. The carrier frequency of the pulse is $\nu = 700$ cm^{-1}, and the intensity is $I_0 = 1.0 \cdot 10^{13}$ W/cm^2. Since the intensity is proportional to the maximum electric field amplitude squared E_0^2, the strength of the coupling term, and thereby the excitation energy, is dependent on the intensity. By a trial and error approach, we have established that for the chosen laser intensity, the excitation energy is on average $\sim$ 4.5 kcal/mol for our selected example. The 700 cm^{-1} carrier frequency of the pulse approximately corresponds to the peak in the liquid water librational frequency spectrum [83], which is shown in Fig. 5.7(b).

The work terms for this time-dependent field excitation are plotted in Fig. 5.8 and should be compared with the instantaneous excitation results in Fig. 5.4. Clearly, the time dependence of these terms during the first few hundred femtoseconds is different for the instantaneous and time-dependent excitations. This is to be expected given the different mechanisms and time scales of the short time angular momentum alteration. But their long-time behaviour is very much alike, e.g. in each case $\sim$ 90 % of the excited

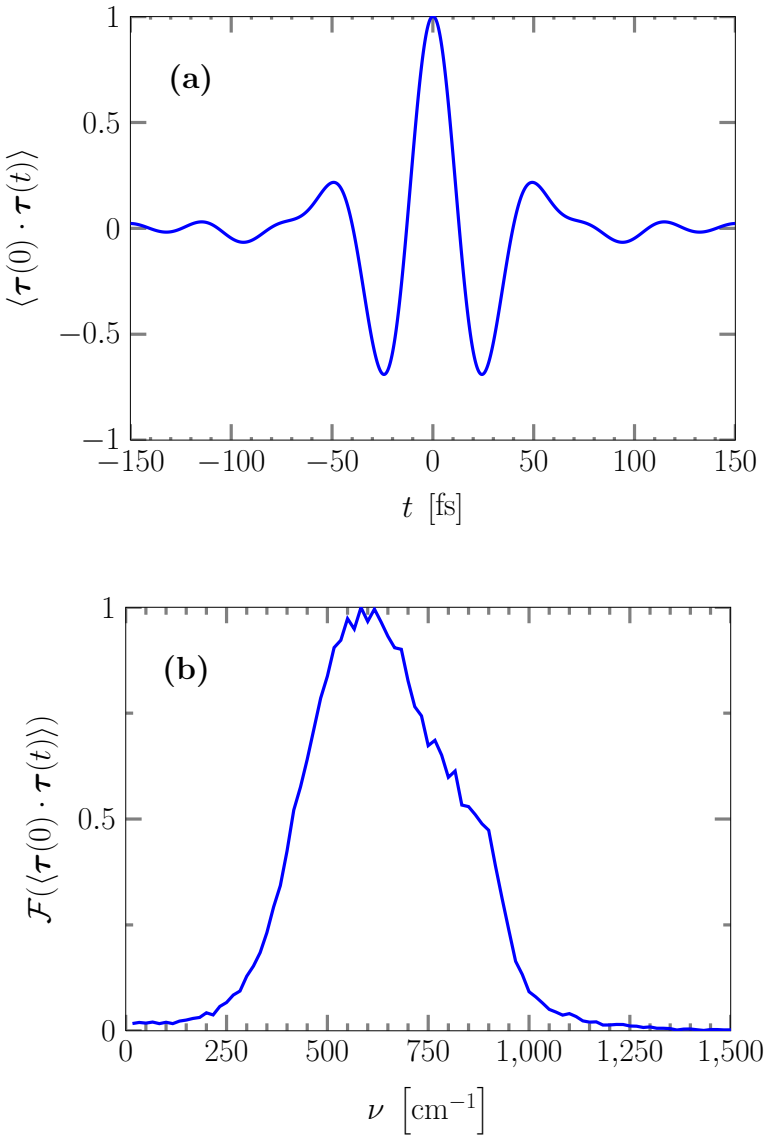

Figure 5.7: (a) Normalized equilibrium time correlation function for the torque on the central molecule. (b) Fourier transform of the normalized equilibrium time correlation function for the torque on the central water molecule. This 'librational band' has a peak at $\nu \approx 600$ cm^{-1}.

water's excess rotational kinetic energy is transferred to the rotational degrees of freedom of the surrounding solvent waters. Hence, the method of excitation does not affect the relative contributions of energy flow to translational and rotational degrees of freedom of the solvent. Indeed, the I_0 column of Tab. 5.1 shows the very close correspondence for all quantities calculated for the different excitation methods.

We have also investigated how the characteristics of the librational energy transfer depend on the frequency of the electric field by carrying out simulations with frequencies of 100 cm^{-1}, 400 cm^{-1}, 700 cm^{-1}, 1000 cm^{-1}, and 1300 cm^{-1}, while keeping the same electric field intensity. We find that the amount of energy transferred from the electric field to the central water molecule depends strongly on the frequency: $E_{100\ \text{cm}^{-1}} \approx 0.4$ kcal/mol, $E_{400\ \text{cm}^{-1}} \approx 3.4$ kcal/mol, $E_{700\ \text{cm}^{-1}} \approx 4.5$ kcal/mol, $E_{1000\ \text{cm}^{-1}} \approx 1.9$ kcal/mol, and $E_{1300\ \text{cm}^{-1}} \approx 0.3$ kcal/mol. The peaking of the absorption near 700 cm^{-1} is in agreement with the study of Yagasaki and Saito [161], who examined the IR absorption by coupling

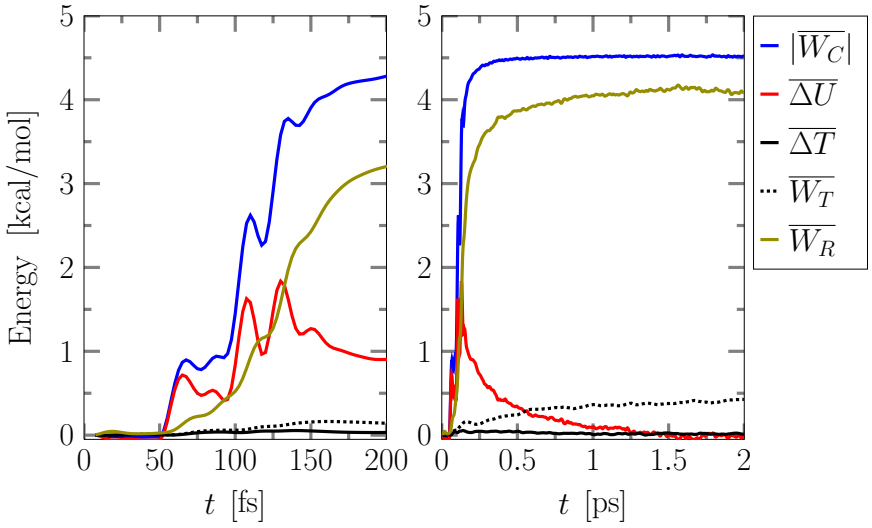

Figure 5.8: Absolute value of the average nonequilibrium work on the rotational degrees of freedom $|\overline{W_C}|$ of the central molecule, the difference in potential energy $\overline{\Delta U}$ between time 0 and t, the difference in translational kinetic energy $\overline{\Delta T_C}$ of the central water, the work on the translational $\overline{W_T}$ and the rotational degrees of freedom $\overline{W_R}$ of the water solvent for rotational excitation of the central water with a time-dependent electric field ($\nu = 700$ cm^{-1}).

the entire system to an electric field (of frequencies 500 cm^{-1}, 700 cm^{-1}, and 900 cm^{-1}) as opposed to the single water molecule coupling in the present study. The present peaking of the nonequilibrium response is understandable in terms of the frequency spectrum of the equilibrium time correlation function (TCF) of the torque on the water molecule shown in Fig. 5.7(b), which is approximately bell-shaped, peaks at $\nu \approx 600$ cm^{-1} and spans the interval $\sim$ 200-1100 cm^{-1}.

For all frequencies $\sim$ 85-91 % of the excess rotational kinetic energy is transferred to the rotational degrees of freedom of the solvent waters. This result is in good agreement with the Sec. 5.4.3 results for the energy dependence for the librational relation with instantaneous excitation. The result indicates that the dependence of the energy flow route on the electric field carrier frequency and thereby on the excitation energy is quite weak.

5.4.6 Rotational Caging and Linear Response

In our discussion in Sec. 5.4.2 of the work on the excited water molecule rotation, the average rotational kinetic energy of that molecule, and the potential energy of interaction with the remaining waters, we indicated that the pronounced short time oscillation was associated with rotational caging of the water molecule. Here, we present the origin of this statement, extending via a linear response perspective the discussion in Ingrosso *et al.* [72] to a single water molecule axis rotational excitation and in addition shedding some light on the exchange of energy between the excited and nonexcited axis rotations.

For rotational excitation about the x-axis of the water molecule, the natural linear response comparison between the nonequilibrium decay and the decay of the equilibrium fluctuations is between the normalized nonequilibrium decay

$$\overline{\delta R}(t)/\overline{\delta R}(0) = (\overline{R}(t) - \langle R \rangle)/(\overline{R}(0) - \langle R \rangle)\,, \tag{5.17}$$

and the normalized equilibrium TCF involving the fluctuations of the x-axis and the full rotational kinetic energies [72]

$$\langle \delta R_x(0) \delta R(t) \rangle / \langle \delta R_x(0) \delta R(0) \rangle \,. \tag{5.18}$$

Fig. 5.9 shows that the agreement between these two functions is excellent for 1 kcal/mol excitation (i.e. in the thermal range) and is only slightly less satisfactory, mainly beyond the first oscillation peak, for the 5 kcal/mol excitation. Fig. 5.9 also includes a comparison with the exclusively x-axis normalized TCF

$$\langle \delta R_x(0) \delta R_x(t) \rangle / \langle \delta R_x(0) \delta R_x(0) \rangle \,. \tag{5.19}$$

The first use of this last comparison is to gain an impression of the exchange of rotational kinetic energy between rotation about the x-axis and the remaining y- and z-axis. The difference between Eq. 5.18 and Eq. 5.19 in Fig. 5.9 indicates that in the equilibrium ensemble, the exchange sets in primarily just past the oscillation peak and is not negligible providing up to about a factor of two in the correlations at these longer times.

Given the good agreement between the nonequilibrium function and both of the presented equilibrium functions up to and including the neighborhood of the first oscillation peak, the second use of the comparison is that we can use the x-axis TCF in Eq. 5.19 to demonstrate the peak's origin in the rotational caging. If the statistical behaviour of the x-axis angular momentum J_x dynamics is Gaussian, then it is straightforward to show that the behaviour of the x-axis TCF in Eq. 5.19 is related to the square of the normalized TCF of J_x by [72]

$$\langle \delta R_x(0) \delta R_x(t) \rangle / \langle [\delta R_x]^2 \rangle = \langle \delta J_x^2(0) \delta J_x^2(t) \rangle / \langle [\delta J_x(0)]^2 \rangle = [\langle J_x(0) J_x(t) \rangle / \langle J_x^2 \rangle]^2 \,. \tag{5.20}$$

Fig. 5.10 shows the first minimum in the normalized J_x TCF signaling the rotational caging reversal of the sign of the initial angular momentum. The figure also shows that this reversal produces an oscillation peak in the square of the J_x TCF, which is in quite good agreement with the peak in the δR_x TCF and — most importantly — in the nonequilibrium relaxation of the rotational kinetic energy for both the 1 and 5 kcal/mol excitations. The demonstration of the same conclusion for the y- and z-axis excitations is provided in the Appendix. While the agreement clearly deteriorates subsequently due to exchange of different axes' rotational kinetic energy, there, nonetheless, remains a reasonable identification of the second, muted peak in the nonequilibrium decay with a subsequent reversal of angular momentum.

5.5 Conclusions

We have investigated the ultrafast librational relaxation of H_2O in liquid water via classical NEMD simulations and elucidated the energy flow pattern. The rotational degrees of freedom of the solvent are the primary acceptors of energy. In fact ~ 85 % of the excess rotational kinetic energy is transferred to the rotational modes, and the remaining ~ 15 % is transferred to the translational modes. These results are not affected by the chosen rotational excitation energy of 5 kcal/mol and the temperature of 300 K. Our simulations show that the same behaviour of the librational relaxation is maintained for excitation energies up to 15 kcal/mol and temperatures up to 350 K. Since the time-scale for the first period of the oscillation in the rotational energy decay corresponds to the time-scale of the reversal of the angular momentum under equilibrium conditions, the reported results also elucidate on the generic librational motion in equilibrated water.

We find that the closest solvent molecules receive most of the energy. The 1st solvent shell is the primary energy acceptor with ~ 80 % of the energy, and the 2nd solvent shell

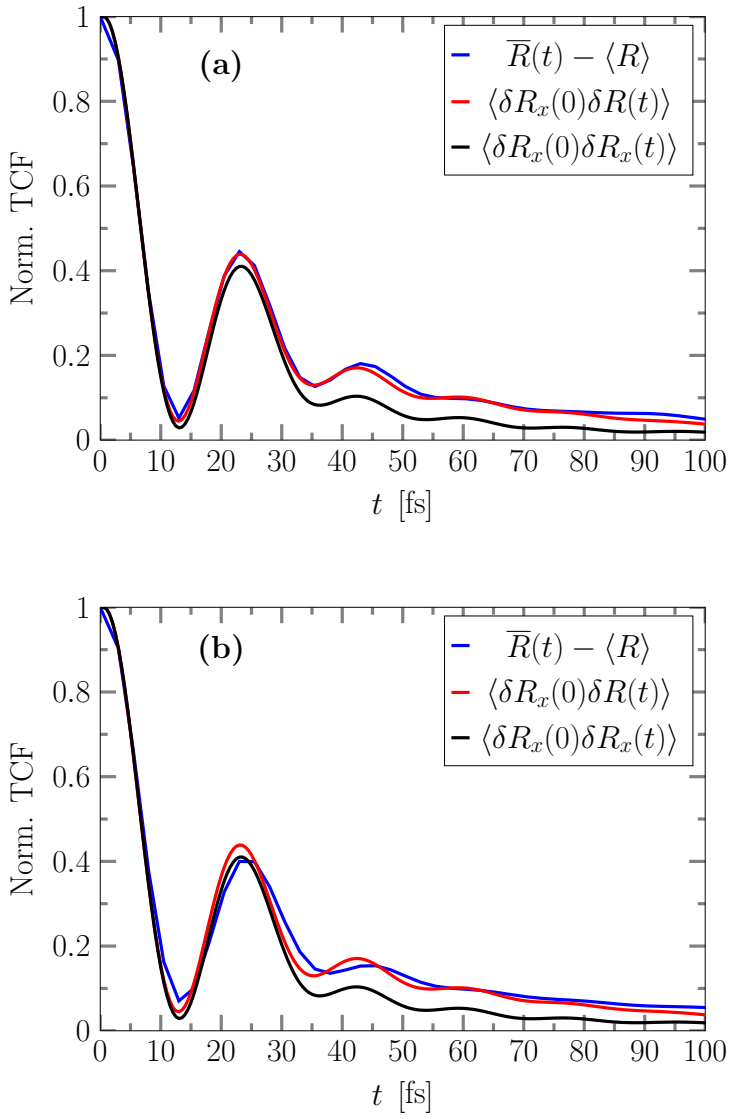

Figure 5.9: Comparison of the nonequilibrium rotational kinetic energy dissipation $\overline{R}(t) - \langle R \rangle$ for the central molecule and the equilibrium TCFs $\langle \delta R_x(0) \delta R(t) \rangle$ and $\langle \delta R_x(0) \delta R_x(t) \rangle$. The nonequilibrium function and each TCF are normalized by their respective initial values. (a) 1 kcal/mol instantaneous excitation with respect to the principal x-axis. (b) 5 kcal/mol instantaneous excitation with respect to the principal x-axis.

receives approximately the rest. These results are in good agreement with the recent bend vibrational relaxation study by Rey and Hynes.[75]

To test the validity of the simulations with an instantaneous rotational excitation, we have also carried out simulations in which the rotational excitation comes about by coupling the dipole moment of the central molecule to a time-dependent electric field. The results do not change significantly, and we conclude that the approximation of an instantaneous excitation is justified.

Yagasaki and Saito [161] suggest a cascading of energy with translation receiving energy at the end of the ladder, which is in general accord with our results. However, this description, based on a coarse-grained kinetic model, is only approximately correct. We have shown here unambiguously that indeed there is direct transfer from the excited mode

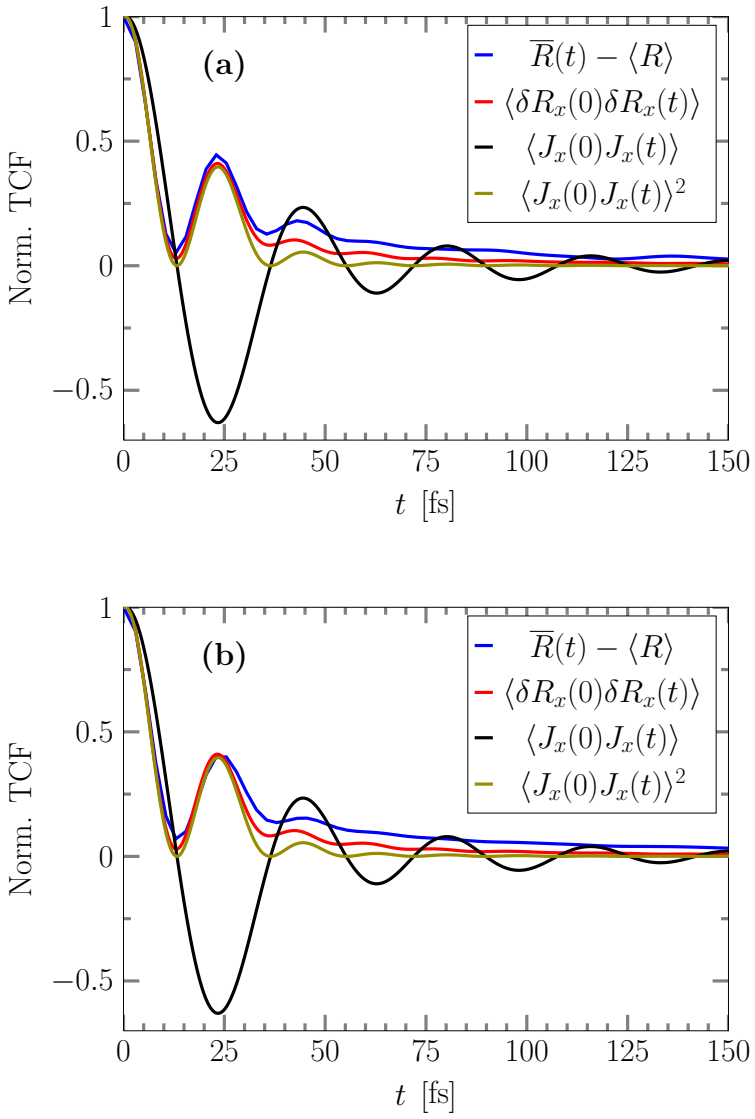

Figure 5.10: Comparison of the nonequilibrium rotational kinetic energy dissipation $\overline{R}(t) - \langle R \rangle$ for the central molecule and the equilibrium TCFs $\langle \delta R_x(0) \delta R_x(t) \rangle$, $\langle J_x(0) J_x(t) \rangle$, and $\langle J_x(0) J_x(t) \rangle^2$. The nonequilibrium function and each TCF are normalized by their respective initial values. (a) 1 kcal/mol instantaneous excitation with respect to the principal x-axis. (b) 5 kcal/mol instantaneous excitation with respect to the principal x-axis.

to translation with no need to detour through lower frequency rotations.

Chapter 6

Concluding Remarks

In this thesis work, the general topic is vibrational and rotational energy relaxation in liquids, where the time-evolution of the relaxation processes is followed via classical MD simulations. First we investigate the applicability of the classical BZ model to describe the nuclear dynamics for the photodissociation of a gas-phase Br_2 molecule. We find that the nuclear dynamics described by the BZ model is in very good agreement with quantum mechanics wave packet calculations in terms of the time-evolution of the expectation value of the nuclear position in the antibonding state, although the apparent usefulness of the BZ model is in contrast to the validity of the individual approximations involved in deriving the BZ model from a quantum mechanics treatment of gas-phase photodissociation.

In the spirit of the BZ model, the photodissociation, subsequent geminate recombination, and vibrational energy relaxation of I_2 in CCl_4 are studied by means of classical nonequilibrium MD simulations. The time-dependent vibrational energy distribution is in perfect agreement with previous experimental results obtained via ultrafast optical pump-probe spectroscopy. We compare the relaxation times and the time-dependent I-I pair distribution function to new time-resolved x-ray diffraction results, and we find a qualitative agreement in both cases. Also, we show that a good approximation to the time-dependent I-I pair distribution function can be obtained from the time-dependent vibrational energy distribution such that experimental results from time-resolved x-ray diffraction and optical spectroscopy can be compared. Furthermore, we observe some degree of vibrational coherence, which has been absent in previous simulations of vibrational energy relaxation of I_2 in liquids.

The rotational energy relaxation of a rotationally excited H_2O molecule is also studied by means of classical nonequilibrium MD simulations. We use a recent reformulation of a power and work analysis, in which a detailed molecular description of the energy flow between various degrees of freedom is possible. The water molecules are treated as rigid rotors, and we find that the rotational degrees of freedom for the surrounding solvent are the primary energy acceptors during the relaxation of the excited H_2O molecule, with a minor transfer to the translational degrees of freedom. Furthermore, we find that the relaxation process is quite local, since the ~ 25 molecules in the 1st and 2nd solvent shells primarily accept the excess energy from the rotationally excited central molecule.

6.1 Future Research

An interesting future study is classical nonequilibrium MD simulations of the vibrational energy relaxation of I_2 in CCl_4 using a power and work analysis, such that the energy pathway can be elucidated, and the locality of the relaxation process can be determined. Furthermore, the relaxation process' dependence on freezing the vibrational modes of CCl_4 in the present study can be investigated by using a flexible force field model for CCl_4 and a

power and work analysis. Also, a QM/MM description of the photodissociation, geminate recombination, and vibrational energy relaxation of I_2 in CCl_4 can provide new insights, since the electronic transitions of the iodine molecule can be described by quantum mechanics. A QM/MM treatment of the rotational energy relaxation of H_2O in liquid water is also of interest.

We have initiated a study of the rotational energy relaxation in a nonpolar liquid to establish whether there is any difference compared to that of liquid water. In Fig. 6.1 the work terms for the rotational energy relaxation of a rotationally excited CCl_4 in liquid carbon tetrachloride are plotted. Clearly, the relaxation time is much longer for CCl_4 than H_2O, in fact the rotational relaxation is not completed at 2 ps after the instantaneous excitation. Furthermore, the transfer of excess rotational kinetic energy is almost equally divided between the translational and rotational degrees of freedom of the surrounding solvent molecule. These discrepancies from the water case are somewhat expected due to the lack of strong hydrogen bonds in the CCl_4 liquid.

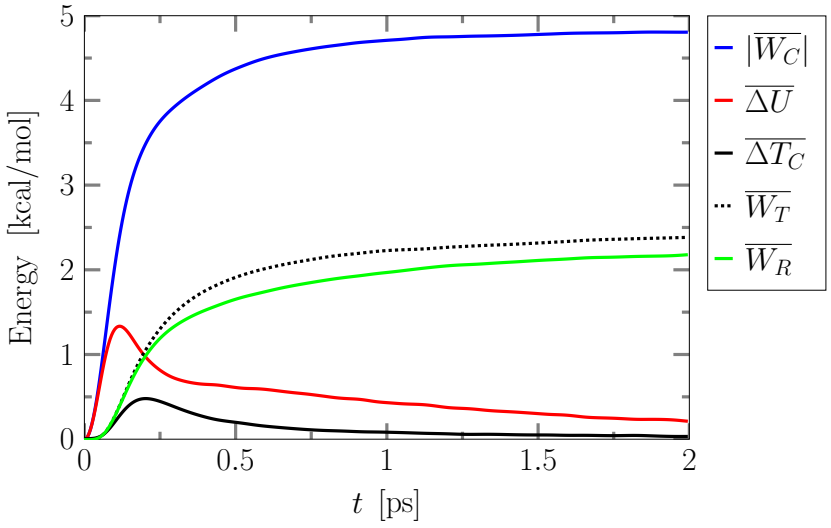

Figure 6.1: Nonequilibrium average work and energy terms for instantaneous rotational excitation of the central CCl_4 molecule. Shown are the absolute value of the work on the rotational degrees of freedom $|\overline{W_C}|$ of the central molecule, the difference in potential energy $\overline{\Delta U}$ between time 0 and t, and the difference in translational kinetic energy $\overline{\Delta T_C}$ of the central molecule, and the work on the translational $\overline{W_T}$, and the rotational degrees of freedom $\overline{W_R}$ of the surrounding CCl_4 solvent.

Appendix

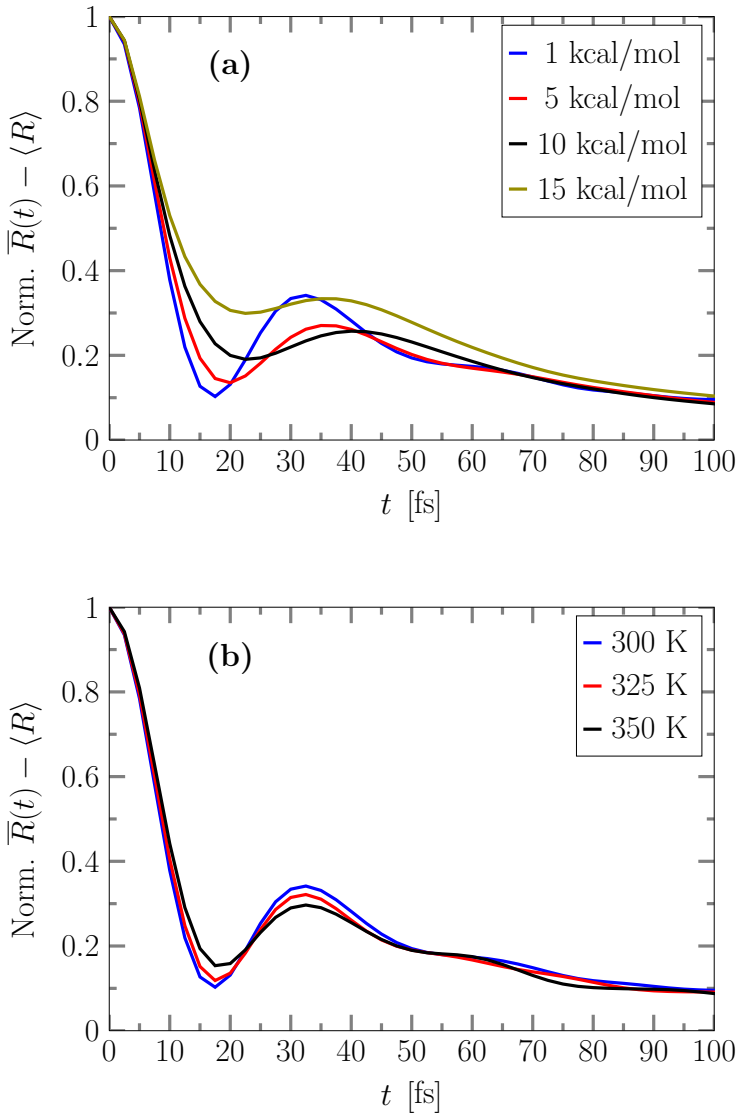

Figure A-1: (a) Normalized nonequilibrium average excess rotational kinetic energy of the central water molecule for four different excitation energies. The instantaneous excitation is with respect to the principal y-axis. (b) Normalized nonequilibrium average excess rotational kinetic energy for three different temperatures, where the 1 kcal/mol instantaneous excitation of the central water is with respect to the principal y-axis.

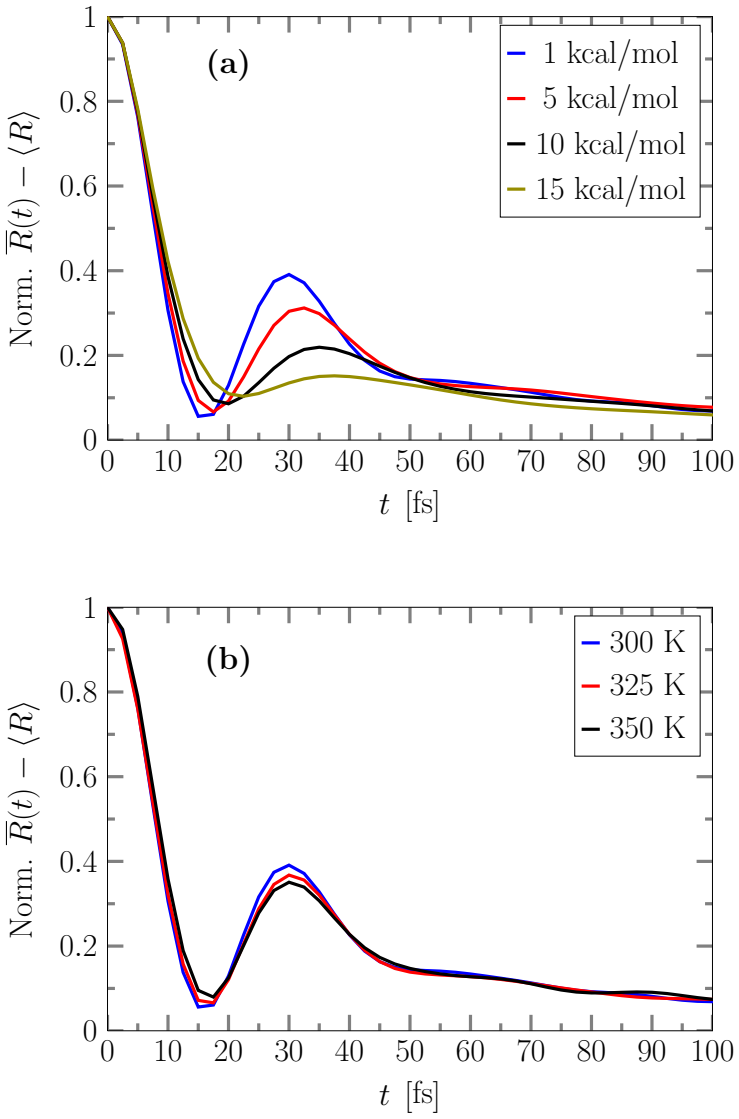

Figure A-2: (a) Normalized nonequilibrium average excess rotational kinetic energy of the central water molecule for four different excitation energies. The instantaneous excitation is with respect to the principal z-axis. (b) Normalized nonequilibrium average excess rotational kinetic energy for three different temperatures, where the 1 kcal/mol instantaneous excitation of the central water is with respect to the principal z-axis.

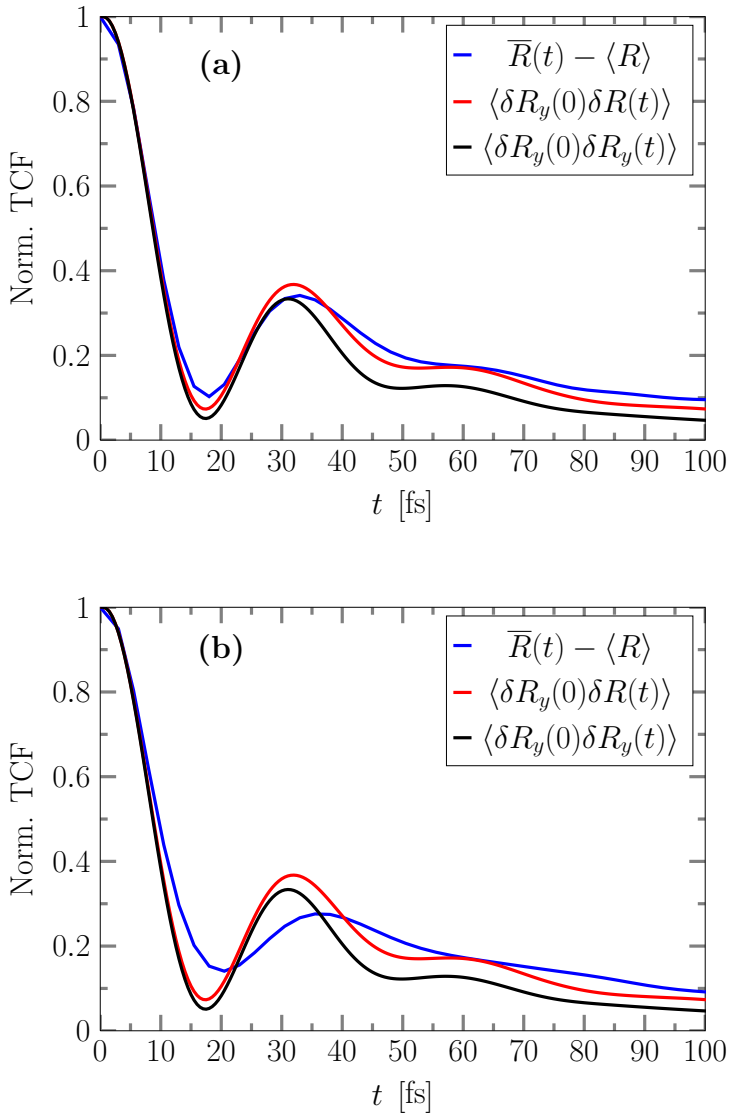

Figure A-3: Comparison of the nonequilibrium rotational kinetic energy dissipation $\overline{R}(t) - \langle R \rangle$ for the central molecule and the equilibrium TCFs $\langle \delta R_y(0) \delta R(t) \rangle$ and $\langle \delta R_y(0) \delta R_y(t) \rangle$. The nonequilibrium function and each TCF are normalized by their respective initial values. (a) 1 kcal/mol instantaneous excitation with respect to the principal y-axis. (b) 5 kcal/mol instantaneous excitation with respect to the principal y-axis.

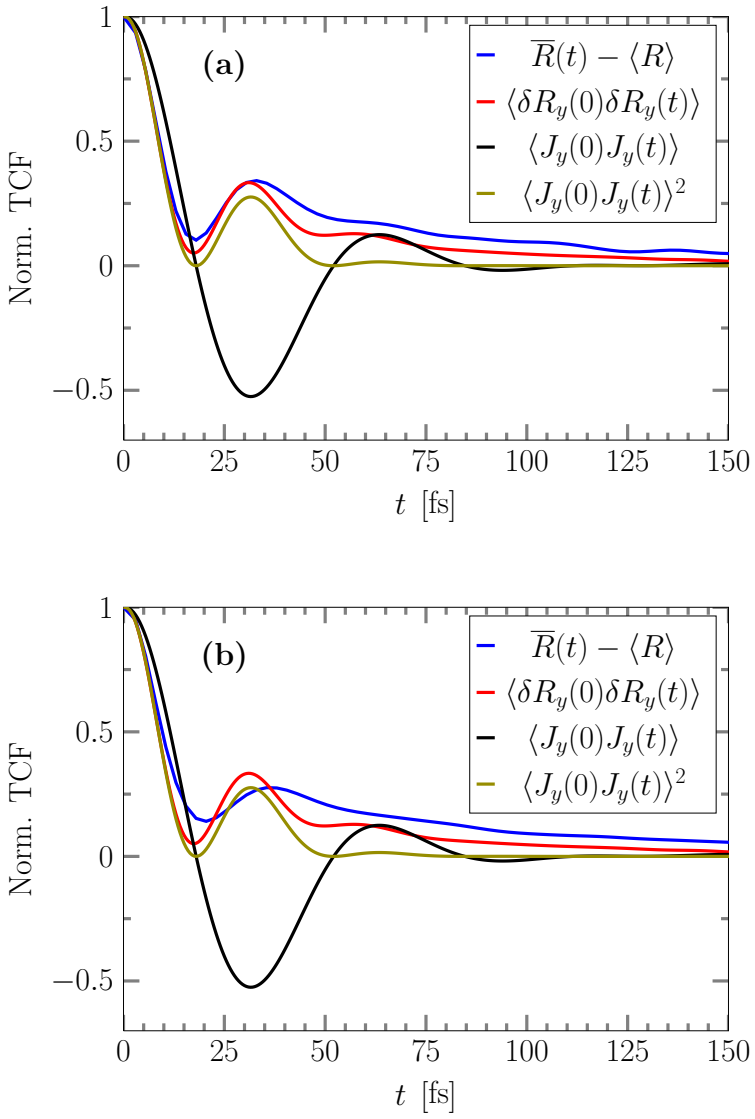

Figure A-4: Comparison of the nonequilibrium rotational kinetic energy dissipation $\overline{R}(t) - \langle R \rangle$ for the central molecule and the equilibrium TCFs $\langle \delta R_y(0) \delta R_y(t) \rangle$, $\langle J_y(0) J_y(t) \rangle$, and $\langle J_y(0) J_y(t) \rangle^2$. The nonequilibrium function and each TCF are normalized by their respective initial values. (a) 1 kcal/mol instantaneous excitation with respect to the principal y-axis. (b) 5 kcal/mol instantaneous excitation with respect to the principal y-axis.

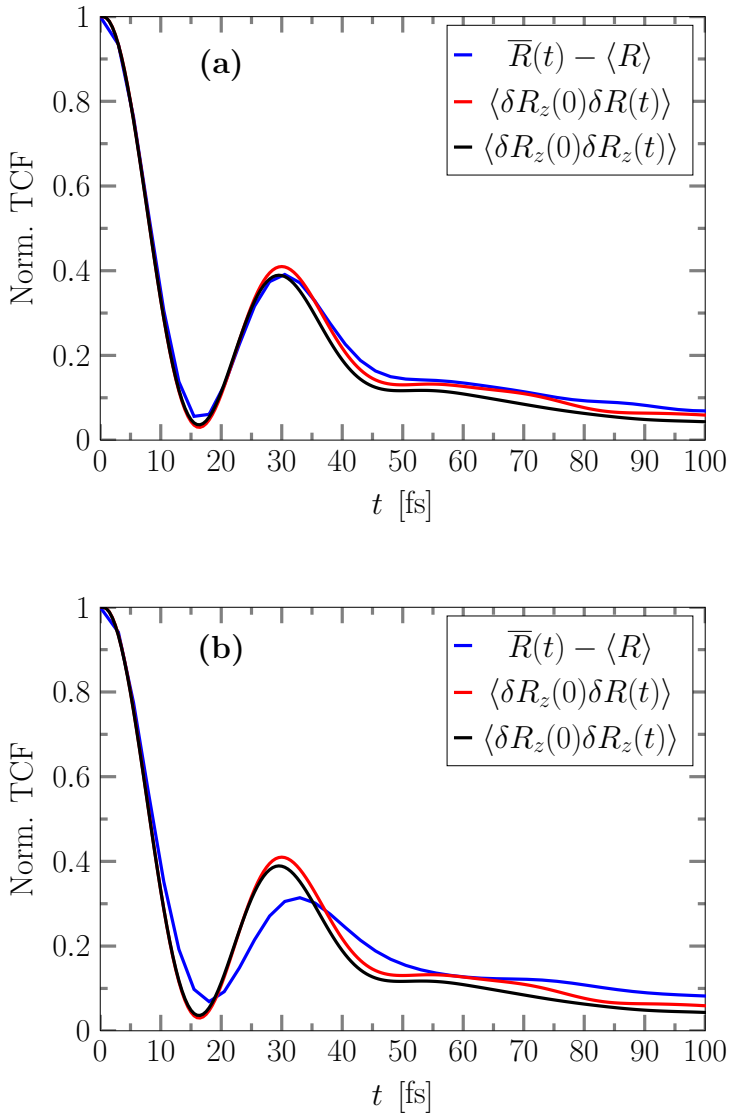

Figure A-5: Comparison of the nonequilibrium rotational kinetic energy dissipation $\overline{R}(t) - \langle R \rangle$ for the central molecule and the equilibrium TCFs $\langle \delta R_z(0) \delta R(t) \rangle$ and $\langle \delta R_z(0) \delta R_z(t) \rangle$. The nonequilibrium function and each TCf are normalized by their respective initial values. (a) 1 kcal/mol instantaneous excitation with respect to the principal z-axis. (b) 5 kcal/mol instantaneous excitation with respect to the principal z-axis.

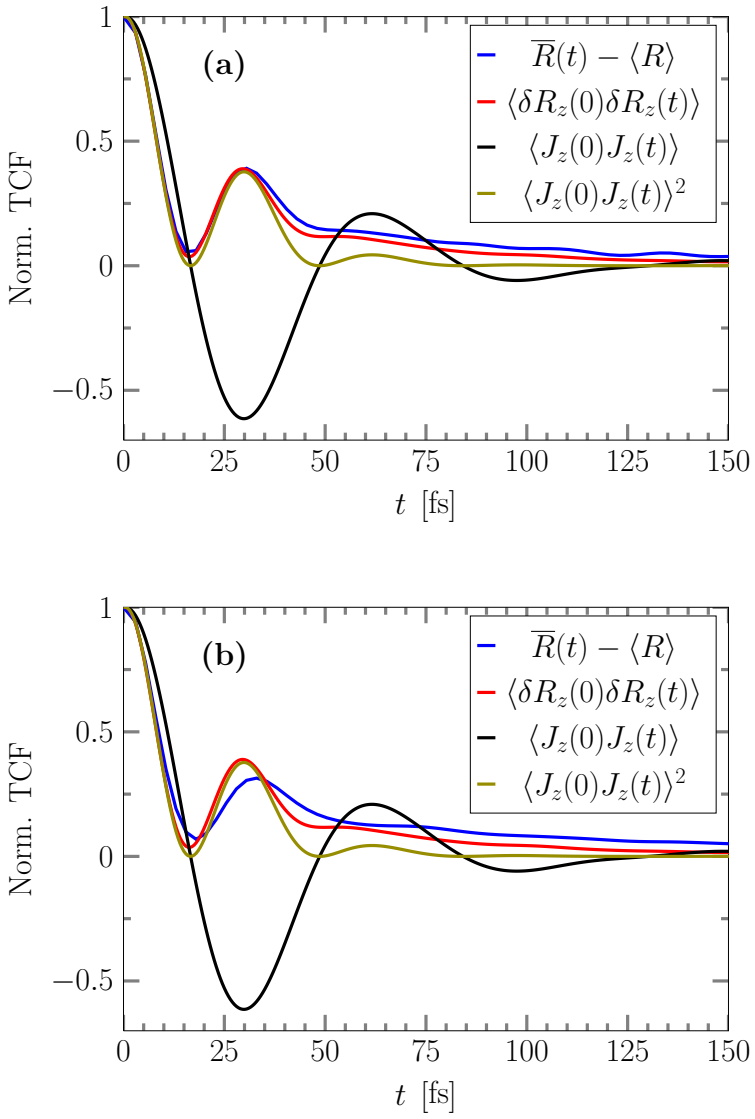

Figure A-6: Comparison of the nonequilibrium rotational kinetic energy dissipation $\overline{R}(t) - \langle R \rangle$ for the central molecule and the equilibrium TCFs $\langle \delta R_z(0) \delta R_z(t) \rangle$, $\langle J_z(0) J_z(t) \rangle$, and $\langle J_z(0) J_z(t) \rangle^2$. The nonequilibrium function and each TCF are normalized by their respective initial values. (a) 1 kcal/mol instantaneous excitation with respect to the principal z-axis. (b) 5 kcal/mol instantaneous excitation with respect to the principal z-axis.

Bibliography

[1] R. A. Marcus. Unimolecular Dissociations and Free Radical Recombination Reactions. *J. Chem. Phys.*, 20(3):359–364, 1952.

[2] J. G. Parker. Rotational and Vibrational Relaxation in Diatomic Gases. *Phys. Fluids*, 2(4):449–462, 1959.

[3] R. G. Gordon, W. Klemperer, and J. I. Steinfeld. Vibrational and Rotational Relaxation. *Annu. Rev. Phys. Chem.*, 19:215–250, 1968.

[4] P. M. Felker and A. H. Zewail. Dynamics of Intramolecular Vibrational-Energy Redistribution (IVR). I. Coherence Effects. *J. Chem. Phys.*, 82(7):2961–2974, 1985.

[5] P. M. Felker and A. H. Zewail. Dynamics of Intramolecular Vibrational-Energy Redistribution (IVR). II. Excess Energy Dependence. *J. Chem. Phys.*, 82(7):2975–2993, 1985.

[6] A. H. Zewail. Femtochemistry: Atomic-Scale Dynamics of the Chemical Bond using Ultrafast Lasers. *Angew. Chem. Int. Ed.*, 39(15):2587–2631, 2000.

[7] C. B. Harris, D. E. Smith, and D. J. Russell. Vibrational Relaxation of Diatomic Molecules in Liquids. *Chem. Rev.*, 90(3):481–488, 1990.

[8] J. C. Owrutsky, D. Raftery, and R. M. Hochstrasser. Vibrational Relaxation Dynamics in Solutions. *Annu. Rev. Phys. Chem.*, 45:519–555, 1994.

[9] R. M. Stratt and M. Maroncelli. Nonreactive Dynamics in Solution: The Emerging Molecular View of Solvation Dynamics and Vibrational Relaxation. *J. Phys. Chem.*, 100(31):12981–12996, 1996.

[10] R. D. Levine and R. B. Bernstein. *Molecular Reaction Dynamics.* Oxford University Press, 1974.

[11] J. T. Hynes. Chemical Reaction Dynamics in Solution. *Annu. Rev. Phys. Chem.*, 36:573–597, 1985.

[12] D. J. Nesbitt and R. W. Field. Vibrational Energy Flow in Highly Excited Molecules: Role of Intramolecular Vibrational Redistribution. *J. Phys. Chem.*, 100(31):12735–12756, 1996.

[13] K. F. Everitt, J. L. Skinner, and B. M. Ladanyi. Vibrational Energy Relaxation in Liquid Oxygen (Revisited) and in Liquid Nitrogen. *J. Chem. Phys.*, 116(1):179–183, 2002.

[14] A. Nitzan. *Chemical Dynamics in Condensed Phases.* Oxford University Press, 2006.

[15] J. L. Skinner. Following the Motions of Water Molecules in Aqueous Solutions. *Science*, 328:985–986, 2010.

[16] W. G. Rothschild. Molecular Motion in Liquids: Rotational and Vibrational Relaxation in Highly Polar and Strongly Associated Systems. *J. Chem. Phys.*, 57(2):991–1002, 1972.

[17] D. W. Oxtoby. Vibrational Relaxation in Liquids. *Annu. Rev. Phys. Chem.*, 32:77–101, 1981.

[18] G. A. Voth and R. M. Hochstrasser. Transition State Dynamics and Relaxation Processes in Solutions: A Frontier of Physical Chemistry. *J. Phys. Chem.*, 100(31):13034–13049, 1996.

[19] Q. Liu, J.-K. Wang, and A. H. Zewail. Femtosecond Dynamics of Dissociation and Recombination in Solvent Cages. *Nature*, 364:427–430, 1993.

[20] Z. Wang, A. Pakoulev, and D. D. Dlott. Watching Vibrational Energy Transfer in Liquids with Atomic Spatial Resolution. *Science*, 296:2201–2203, 2002.

[21] J. Aßmann, M. Kling, and B. Abel. Watching Photoinduced Chemistry and Molecular Energy Flow in Solution in Real Time. *Angew. Chem. Int. Ed.*, 42:2226–2246, 2003.

[22] A. Plech, M. Wulff, S. Bratos, F. Mirloup, R. Vuilleumier, F. Schotte, and P. A. Anfinrud. Visualizing Chemical Reactions in Solution by Picosecond X-Ray Diffraction. *Phys. Rev. Lett.*, 92(12):125505, 2004.

[23] K. J. Gaffney and H. N. Chapman. Imaging Atomic Structure and Dynamics with Ultrafast X-Ray Scattering. *Science*, 316:1444–1448, 2007.

[24] J. Troe. Atom and Radical Recombination Reactions. *Annu. Rev. Phys. Chem.*, 29:223–250, 1978.

[25] D. Levesque, J.-J. Weis, and D. W. Oxtoby. A Molecular Dynamics Simulation of Rotational and Vibrational Relaxation in Liquid HCl. *J. Chem. Phys.*, 79(2):917–925, 1983.

[26] P. Hänggi, P. Talkner, and M. Borkovec. Reaction-Rate Theory: Fifty Years after Kramers. *Rev. Mod. Phys.*, 62(2):251–341, 1990.

[27] M. Li, J. Owrutsky, M. Sarisky, J. P. Culver, A. Yodh, and R. M. Hochstrasser. Vibrational and Rotational Relaxation Times of Solvated Molecular Ions. *J. Chem. Phys.*, 98(7):5499–5507, 1993.

[28] S. Okazaki. Dynamical Approach to Vibrational Relaxation. *Adv. Chem. Phys.*, 118:191–270, 2001.

[29] R. Rey, K. B. Møller, and J. T. Hynes. Ultrafast Vibrational Population Dynamics of Water and Related Systems: A Theoretical Perspective. *Chem. Rev.*, 104(4):1915–1928, 2004.

[30] J. L. Skinner. Vibrational Energy Relaxation of Small Molecules and Ions in Liquids. *Theor. Chem. Acc.*, 128:147–155, 2011.

[31] M. P. Allen and D. J. Tildesley. *Computer Simulation of Liquids*. Oxford University Press, 1987.

[32] W. F. van Gunsteren and A. E. Mark. Validation of Molecular Dynamics Simulation. *J. Chem. Phys.*, 108(15):6109–6116, 1998.

[33] A. C. T. van Duin, S. Dasgupta, F. Lorant, and W. A. Goddard. ReaxFF: A Reactive Force Field for Hydrocarbons. *J. Phys. Chem. A*, 105(41):9396–9409, 2001.

[34] J. Franck and E. Rabinowitch. Some Remarks about Free Radicals and the Photochemistry of Solutions. *Trans. Faraday Soc.*, 30:120–130, 1934.

[35] E. Rabinowitch and W. C. Wood. Properties of Illuminated Iodine Solutions. I. Photochemical Dissociation of Iodine Molecules in Solution. *Trans. Faraday Soc.*, 32(1):547–556, 1936.

[36] E. Rabinowitch and W. C. Wood. The Collision Mechanism and the Primary Photochemical Process in Solutions. *Trans. Faraday Soc.*, 32(2):1381–1387, 1936.

[37] R. Bersohn and A. H. Zewail. Time Dependent Absorption of Fragments During Dissociation. *Ber. Bunsenges. Phys. Chem.*, 92:373–378, 1988.

[38] I. Benjamin. Photodissociation of ICN in Liquid Chloroform: Molecular Dynamics of Ground and Excited State Recombination, Cage Escape, and Hydrogen Abstraction Reaction. *J. Chem. Phys.*, 103(7):2459–2471, 1995.

[39] D. Schwarzer, J. Schroeder, and C. Schröder. Quantum Yields for the Photodissociation of Iodine in Compressed Liquids and Supercritical Fluids. *Z. Phys. Chem.*, 215(2):183–195, 2001.

[40] K. B. Møller and A. H. Zewail. Kinetics Modeling of Dynamics: The Case of Femtosecond-Activated Direct Reactions. *Chem. Phys. Lett.*, 351:281–288, 2002.

[41] M. L. Johnson and I. Benjamin. Photodissociation of ICN at the Water/Chloroform Interface. *J. Phys. Chem. A*, 113(26):7403–7411, 2009.

[42] S.-Y. Lee, W. T. Pollard, and R. A. Mathies. Quasi-Classical Models of Transition State Absorption or Emission. *Chem. Phys. Lett.*, 163(1):11–18, 1989.

[43] J. T. Hynes, R. Kapral, and G. M. Torrie. Stochastic Trajectory Simulation of Iodine Recombination in Liquids. *J. Chem. Phys.*, 72(1):177–188, 1980.

[44] T. J. Chuang, G. W. Hoffman, and K. B. Eisenthal. Picosecond Studies of the Cage Effect and Collision Induced Predissociation of Iodine in Liquids. *Chem. Phys. Lett.*, 25(2):201–205, 1974.

[45] A. L. Harris, M. Berg, and C. B. Harris. Studies of Chemical Reactivity in the Condensed Phase. I. The Dynamics of Iodine Photodissociation and Recombination on a Picosecond Time Scale and Comparison to Theories for Chemical Reactions in Solution. *J. Chem. Phys.*, 84(2):788–806, 1986.

[46] D. E. Smith and C. B. Harris. Studies of Chemical Reactivity in the Condensed Phase. III. Direct Measurement of Predissociation and Geminate Recombination Times for Iodine in Solution. *J. Chem. Phys.*, 87(5):2709–2715, 1987.

[47] A. L. Harris, J. K. Brown, and C. B. Harris. The Nature of Simple Photodissociation Reactions in Liquids on Ultrafast Time Scales. *Annu. Rev. Phys. Chem.*, 39:341–366, 1988.

[48] S. Bratos, F. Mirloup, R. Vuilleumier, M. Wulff, and A. Plech. X-Ray 'Filming' of Atomic Motions in Chemical Reactions. *Chem. Phys.*, 304:245–251, 2004.

[49] M. E. Paige, D. J. Russell, and C. B. Harris. Studies of Chemical Reactivity in the Condensed Phase. II. Vibrational Relaxation of Iodine in Liquid Xenon following Geminate Recombination. *J. Chem. Phys.*, 85(6):3699–3700, 1986.

[50] M. E. Paige and C. B. Harris. Ultrafast Studies of Chemical Reactions in Liquids: Validity of Gas Phase Vibrational Relaxation Models and Density Dependence of Bound Electronic State Lifetimes. *Chem. Phys.*, 149:37–62, 1990.

[51] E. D. Potter, Q. Liu, and A. H. Zewail. Femtosecond Reaction Dynamics in Macroclusters. Effect of Solvation on Wave-Packet Motion. *Chem. Phys. Lett.*, 200(6):605–614, 1992.

[52] R. Zadoyan, Z. Li, P. Ashjian, C. C. Martens, and V. A. Apkarian. Femtosecond Dynamics of Coherent Photodissociation-Recombination of I_2 Isolated in Matrix Ar. *Chem. Phys. Lett.*, 218:504–514, 1994.

[53] R. Zadoyan, Z. Li, C. C. Martens, and V. A. Apkarian. The Breaking and Remaking of a Bond: Caging of I_2 in Solid Kr. *J. Chem. Phys.*, 101(8):6648–6657, 1994.

[54] W. Wang, K. A. Nelson, L. Xiao, and D. F. Coker. Molecular Dynamics Simulation Studies of Solvent Cage Effects on Photodissociation in Condensed Phases. *J. Chem. Phys.*, 101(11):9663–9671, 1994.

[55] J.-K. Wang, Q. Liu, and A. H. Zewail. Solvation Ultrafast Dynamics of Reactions. 9. Femtosecond Studies of Dissociation and Recombination of Iodine in Argon Clusters. *J. Phys. Chem.*, 99(29):11309–11320, 1995.

[56] W. H. Wong and G. Burns. Trajectory Studies of Atomic Recombination Reactions. IV. Recombination of Iodine Atoms. *J. Chem. Phys.*, 58(10):4459–4467, 1973.

[57] J. N. Murrell, A. J. Stace, and R. Dammel. Computer Simulation of the Cage Effect in the Photodissociation of Iodine. *J. Chem. Soc. Faraday Trans. II*, 74:1532–1539, 1978.

[58] J. P. Bergsma, M. H. Coladonato, P. M. Edelsten, J. D. Kahn, K. R. Wilson, and D. R. Fredkin. Transient X-Ray Scattering Calculated from Molecular Dynamics. *J. Chem. Phys.*, 84(11):6151–6160, 1986.

[59] J. K. Brown, C. B. Harris, and J. C. Tully. Studies of Chemical Reactivity in the Condensed Phase. IV. Density Dependent Molecular Dynamics Simulations of Vibrational Relaxation in Simple Liquids. *J. Chem. Phys.*, 89(11):6687–6696, 1988.

[60] Q. Liu, J.-K. Wang, and A. H. Zewail. Solvation Ultrafast Dynamics of Reactions. 10. Molecular Dynamics Studies of Dissociation, Recombination, and Coherence. *J. Phys. Chem.*, 99(29):11321–11332, 1995.

[61] A. Plech, R. Randler, M. Wulff, F. Mirloup, and R. Vuilleumier. Determination of Structure in Liquid Solutions — Implications for Picosecond Photoexcitation Studies. *J. Phys.: Condens. Matter*, 15:137–143, 2003.

[62] M. Wulff, S. Bratos, A. Plech, R. Vuilleumier, F. Mirloup, M. Lorenc, Q. Kong, and H. Ihee. Recombination of Photodissociated Iodine: A Time-Resolved X-Ray Diffraction Study. *J. Chem. Phys.*, 124:034501, 2006.

[63] N. E. Henriksen and K. B. Møller. On the Theory of Time-Resolved X-ray Diffraction. *J. Phys. Chem. B*, 112(2):558–567, 2008.

[64] L. Giannessi, M. Artioli, M. Bellaveglia, F. Briquez, E. Chiadroni, A. Cianchi, M. Couprie, G. Dattoli, E. Di Palma, G. Di Pirro, M. Ferrario, D. Filippetto, F. Frassetto, G. Gatti, M. Labat, G. Marcus, A. Mostacci, A. Petralia, V. Petrillo, L. Poletto, M. Quattromini, J. Rau, J. Rosenzweig, E. Sabia, M. Serluca, I. Spassovsky, and V. Surrenti. High-Order-Harmonic Generation and Superradiance in a Seeded Free-Electron Laser. *Phys. Rev. Lett.*, 108:164801, 2012.

[65] R. M. Whitnell, K. R. Wilson, and J. T. Hynes. Fast Vibrational Relaxation for a Dipolar Molecule in a Polar Solvent. *J. Phys. Chem.*, 94(24):8625–8628, 1990.

[66] R. M. Whitnell, K. R. Wilson, and J. T. Hynes. Vibrational Relaxation of a Dipolar Molecule in Water. *J. Chem. Phys.*, 96(7):5354–5369, 1992.

[67] R. Rey and J. T. Hynes. Vibrational Energy Relaxation of HOD in Liquid D_2O. *J. Chem. Phys.*, 104(6):2356–2368, 1996.

[68] J. C. Deàk, S. T. Rhea, L. K. Iwaki, and D. D. Dlott. Vibrational Energy Relaxation and Spectral Diffusion in Water and Deuterated Water. *J. Phys. Chem. A*, 104(21):4866–4875, 2000.

[69] C. P. Lawrence and J. L. Skinner. Vibrational Spectroscopy of HOD in Liquid D_2O. I. Vibrational Energy Relaxation. *J. Chem. Phys.*, 117(12):5827–5838, 2002.

[70] A. Pakoulev, Z. Wang, and D. D. Dlott. Vibrational Relaxation and Spectral Evolution following Ultrafast OH Stretch Excitation of Water. *Chem. Phys. Lett.*, 371:594–600, 2003.

[71] J. Lindner, D. Cringus, M. S. Pshenichnikov, and P. Vöhringer. Anharmonic Bend-Stretch Coupling in Neat Liquid Water. *Chem. Phys.*, 341:326–335, 2007.

[72] F. Ingrosso, R. Rey, T. Elsaesser, and J. T. Hynes. Ultrafast Energy Transfer from the Intramolecular Bending Vibration to Librations in Liquid Water. *J. Phys. Chem. A*, 113(24):6657–6665, 2009.

[73] R. Rey, F. Ingrosso, T. Elsaesser, and J. T. Hynes. Pathways for H_2O Bend Vibrational Relaxation in Liquid Water. *J. Phys. Chem. A*, 113(31):8949–8962, 2009.

[74] S. Ashihara, S. Fujioka, and K. Shibuya. Temperature Dependence of Vibrational Relaxation of the OH Bending Excitation in Liquid H_2O. *Chem. Phys. Lett.*, 502:57–62, 2011.

[75] R. Rey and J. T. Hynes. Tracking Energy Transfer from Excited to Accepting Modes: Application to Water Bend Vibrational Relaxation. *Phys. Chem. Chem. Phys.*, 14:6332–6342, 2012.

[76] F. H. Stillinger. Water Revisited. *Science*, 209:451–457, 1980.

[77] B. D. Bursulaya, D. A. Zichi, and H. J. Kim. Molecular Dynamics Simulation Study of Polarizable Solute Solvation in Water. 1. Equilibrium Solvent Structure and Solute Rotational Dynamics. *J. Phys. Chem.*, 100(4):1392–1405, 1996.

[78] F. N. Keutsch, R. S. Fellers, M. G. Brown, M. R. Viant, P. B. Petersen, and R. J. Saykally. Hydrogen Bond Breaking Dynamics of the Water Trimer in the Translational and Librational Band Region of Liquid Water. *J. Am. Chem. Soc.*, 123:5938–5941, 2001.

[79] C. J. Fecko, J. D. Eaves, J. J. Loparo, A. Tokmakoff, and P. L. Geissler. Ultrafast Hydrogen-Bond Dynamics in the Infrared Spectroscopy of Water. *Science*, 301:1698–1702, 2003.

[80] D. Laage and J. T. Hynes. On the Molecular Mechanism of Water Reorientation. *J. Phys. Chem. B*, 112(45):14230–14242, 2008.

[81] N. Huse, S. Ashihara, E. T. J. Nibbering, and T. Elsaesser. Ultrafast Vibrational Relaxation of OH Bending and Librational Excitations in Liquid H_2O. *Chem. Phys. Lett.*, 404:389–393, 2005.

[82] S. Ashihara, N. Huse, A. Espagne, E. T. J. Nibbering, and T. Elsaesser. Vibrational Couplings and Ultrafast Relaxation of the OH Bending Mode in Liquid H_2O. *Chem. Phys. Lett.*, 424:66–70, 2006.

[83] S. Ashihara, N. Huse, A. Espagne, E. T. J. Nibbering, and T. Elsaesser. Ultrafast Structural Dynamics of Water Induced by Dissipation of Vibrational Energy. *J. Phys. Chem. A*, 111(5):743–746, 2007.

[84] B. M. Garraway and K.-A. Suominen. Wave-Packet Dynamics: New Physics and Chemistry in Femto-Time. *Rep. Prog. Phys.*, 58:365–419, 1995.

[85] G. A. Worth and L. S. Cederbaum. Beyond Born-Oppenheimer: Molecular Dynamics Through a Conical Intersection. *Annu. Rev. Phys. Chem.*, 55:127–158, 2004.

[86] J. Manz, M. Oppel, and G. K. Paramonov. Quasi-Coherent Molecular Vibrations with Energies above the Dissociation Threshold in the Ground Electronic State. *J. Phys. Chem. A*, 102(23):4271–4276, 1998.

[87] H.-O. Kreiss and J. Oliger. Comparison of Accurate Methods for the Integration of Hyperbolic Equations. *Tellus*, 3:199–215, 1972.

[88] D. Kosloff and R. Kosloff. A Fourier Method Solution for the Time Dependent Schrödinger Equation as a Tool in Molecular Dynamics. *J. Comput. Phys.*, 52:35–53, 1983.

[89] J. W. Cooley and J. W. Tukey. An Algorithm for the Machine Calculation of Complex Fourier Series. *Math. Comput.*, 19(90):297–301, 1965.

[90] R. Kosloff. Time-Dependent Quantum-Mechanical Methods for Molecular Dynamics. *J. Phys. Chem.*, 92(8):2087–2100, 1988.

[91] J. J. Sakurai. *Modern Quantum Mechanics*. Addison Wesley Longman, 1994.

[92] M. D. Feit, J. A. Fleck, and A. Steiger. Solution of the Schrödinger Equation by a Spectral Method. *J. Comput. Phys.*, 47:412–433, 1982.

[93] H. Yoshida. Construction of Higher Order Symplectic Integrators. *Phys. Lett. A*, 150:262–268, 1990.

[94] M. Braun, C. Meier, and V. Engel. Nanosecond Wave-Packet Propagation with the Split-Operator Technique. *Comput. Phys. Commun.*, 93:152–158, 1996.

[95] P. M. Morse. Diatomic Molecules According to the Wave Mechanics. II. Vibrational Levels. *Phys. Rev.*, 34:57–64, 1929.

[96] R. Kosloff and H. Tal-Ezer. A Direct Relaxation Method for Calculating Eigenfunctions and Eigenvalues of the Schrödinger Equation on a Grid. *Chem. Phys. Lett.*, 127:223–230, 1986.

[97] A. Messiah. *Quantum Mechanics*. Dover Publications, 1999.

[98] A. K. Tiwari, K. B. Møller, and N. E. Henriksen. Controlling the Spreading of Wave Packets of a Dissociating Molecule. *Chem. Phys. Lett.*, 450:6–11, 2007.

[99] L. Verlet. Computer 'Experiments' on Classical Fluids. I. Thermodynamical Properties of Lennard-Jones Molecules. *Phys. Rev.*, 159(1):98–103, 1967.

[100] W. C. Swope, H. C. Andersen, P. H. Berens, and K. R. Wilson. A Computer Simulation Method for the Calculation of Equilibrium Constants for the Formation of Physical Clusters of Molecules: Application to Small Water Clusters. *J. Chem. Phys.*, 76(1):637–649, 1982.

[101] P. H. Berens, D. H. J. Mackay, G. M. White, and K. R. Wilson. Thermodynamics and Quantum Corrections from Molecular Dynamics for Liquid Water. *J. Chem. Phys.*, 79(5):2375–2389, 1983.

[102] H. C. Andersen. Rattle: A 'Velocity' Version of the Shake Algorithm for Molecular Dynamics Calculations. *J. Comput. Phys.*, 52:24–34, 1983.

[103] D. J. Evans and S. Murad. Singularity Free Algorithm for Molecular Dynamics Simulation of Rigid Polyatomics. *Mol. Phys.*, 34(2):327–331, 1977.

[104] W. W. Wood and F. R. Parker. Monte Carlo Equation of State of Molecules Interacting with the Lennard-Jones Potential. I. A Supercritical Isotherm at about Twice the Critical Temperature. *J. Chem. Phys.*, 27(3):720–733, 1957.

[105] N. Metropolis, A. W. Rosenbluth, M. N. Rosenbluth, A. H. Teller, and E. Teller. Equation of State Calculations by Fast Computing Machines. *J. Chem. Phys.*, 21(6):1087–1092, 1953.

[106] D. A. McQuarrie. *Statistical Mechanics*. University Science Books, 2000.

[107] G. E. P. Box and M. E. Muller. A Note on the Generation of Random Normal Deviates. *Ann. Mat. Stat.*, 29(2):610–611, 1958.

[108] S. W. de Leeuw, J. W. Perram, and E. R. Smith. Simulation of Electrostatic Systems in Periodic Boundary Conditions. I. Lattice Sums and Dielectric Constants. *Proc. R. Soc. Lond. A*, 373:27–56, 1980.

[109] D. M. Heyes. Electrostatic Potentials and Fields in Infinite Point Charge Lattices. *J. Chem. Phys.*, 74(3):1924–1929, 1981.

[110] A. Y. Toukmaji and J. A. Board Jr. Ewald Summation Techniques in Perspective: A Survey. *Comput. Phys. Commun.*, 95:73–92, 1996.

[111] M. J. L. Sangster and M. Dixon. Interionic Potentials in Alkali Halides and Their use in Simulations of the Molten Salts. *Adv. Phys.*, 25(3):247–342, 1976.

[112] H. C. Andersen. Molecular Dynamics Simulations at Constant Pressure and/or Temperature. *J. Chem. Phys.*, 72(4):2384–2393, 1980.

[113] S. Nose. A Molecular Dynamics Method for Simulations in the Canonical Ensemble. *Mol. Phys.*, 52(2):255–268, 1984.

[114] W. G. Hoover. Canonical Dynamics: Equilibrium Phase-Space Distributions. *Phys. Rev. A*, 31(3):1695–1697, 1985.

[115] A. Rahman. Correlations in the Motion of Atoms in Liquid Argon. *Phys. Rev.*, 136(2A):405–411, 1964.

[116] P. Mark and L. Nilsson. Structure and Dynamics of the TIP3P, SPC, and SPC/E Water Models at 298 K. *J. Phys. Chem. A*, 105(43):9954–9960, 2001.

[117] A. H. Zewail. Femtochemistry: Atomic-Scale Dynamics of the Chemical Bond. *J. Phys. Chem. A*, 104(24):5660–5694, 2000.

[118] M. Dantus, M. J. Rosker, and A. H. Zewail. Real-Time Femtosecond Probing of 'Transition States' in Chemical Reactions. *J. Chem. Phys.*, 87(4):2395–2397, 1987.

[119] M. J. Rosker, M. Dantus, and A. H. Zewail. Femtosecond Clocking of the Chemical Bond. *Science*, 241:1200–1202, 1988.

[120] M. J. Rosker, M. Dantus, and A. H. Zewail. Femtosecond Real-Time Probing of Reactions. I. The Technique. *J. Chem. Phys.*, 89(10):6113–6127, 1988.

[121] M. Dantus, M. J. Rosker, and A. H. Zewail. Femtosecond Real-Time Probing of Reactions. II. The Dissociation Reaction of ICN. *J. Chem. Phys.*, 89(10):6128–6140, 1988.

[122] R. B. Bernstein and A. H. Zewail. Femtosecond Real-Time Probing of Reactions. III. Inversion to the Potential from Femtosecond Transition-State Spectroscopy Experiments. *J. Chem. Phys.*, 90(2):829–842, 1989.

[123] T. S. Rose, M. J. Rosker, and A. H. Zewail. Femtosecond Real-Time Probing of Reactions. IV. The Reactions of Alkali Halides. *J. Chem. Phys.*, 91(12):7415–7436, 1989.

[124] I. Benjamin and K. R. Wilson. Proposed Experimental Probes of Chemical Reaction Molecular Dynamics in Solution: ICN Photodissociation. *J. Chem. Phys.*, 90(8):4176–4197, 1989.

[125] Y. Yan, R. M. Whitnell, K. R. Wilson, and A. H. Zewail. Femtosecond Chemical Dynamics in Solution. Wavepacket Evolution and Caging of I_2. *Chem. Phys. Lett.*, 193(5):402–412, 1992.

[126] N. Winter and I. Benjamin. Photodissociation of ICN at the Liquid/Vapor Interface of Water. *J. Chem. Phys.*, 121(5):2253–2263, 2004.

[127] A. L. Thompson and T. J. Martínez. Time-Resolved Photoelectron Spectroscopy from First Principles: Excited State Dynamics of Benzene. *Faraday Discuss.*, 150:293–311, 2011.

[128] H. Tao, T. K. Allison, T. W. Wright, A. M. Stooke, C. Khurmi, J. van Tilborg, Y. Liu, R. W. Falcone, A. Belkacem, and T. J. Martínez. Ultrafast Internal Conversion in Ethylene. I. The Excited State Lifetime. *J. Chem. Phys.*, 134:244306, 2011.

[129] R. M. Whitnell, K. R. Wilson, Y. Yan, and A. H. Zewail. Classical Theory of Ultrafast Pump-Probe Spectroscopy: Applications to I_2 Photodissociation in Ar Solution. *J. Mol. Liq.*, 61:153–165, 1994.

[130] S. Mukamel. *Principles of Nonlinear Optical Spectroscopy.* Oxford University Press, 1995.

[131] Z. Li, J.-Y. Fang, and C. C. Martens. Simulation of Ultrafast Dynamics and Pump-Probe Spectroscopy using Classical Trajectories. *J. Chem. Phys.*, 104(18):6919–6929, 1996.

[132] V. A. Ermoshin and V. Engel. Femtosecond Pump-Probe Fluorescence Signals from Classical Trajectories: Comparison with Wave-Packet Calculations. *Eur. Phys. J. D*, 15:413–422, 2001.

[133] D. J. Tannor. *Introduction to Quantum Mechanics – A Time-Dependent Perspective.* University Science Books, 2007.

[134] C. Manescu, J. L. Krause, K. B. Møller, and N. E. Henriksen. Suppressing the Spreading of Continuum Wave Packets via Chirped Laser Pulses. *J. Phys. Chem. A*, 108(41):8840–8847, 2004.

[135] M. Lax. The Franck-Condon Principle and Its Application to Crystals. *J. Chem. Phys.*, 20(11):1752–1760, 1952.

[136] N. E. Henriksen and V. Engel. Femtosecond Pump-Probe Spectroscopy: A Theoretical Analysis of Transient Signals and Their Relation to Nuclear Wave-Packet Motion. *Int. Rev. Phys. Chem.*, 20(2):93–126, 2001.

[137] M. D. Pattengill. Classical Model Studies of Polyatomic Direct Photofragmentation. *Chem. Phys.*, 68:73–81, 1982.

[138] M. D. Pattengill. Classical Trajectory Study of Three-Body Direct Photofragmentation of $Cd(CH_3)_2$. Comparison of Sampling Methods. *Chem. Phys.*, 75:59–66, 1983.

[139] E. J. Heller. Time-Dependent Approach to Semiclassical Dynamics. *J. Chem. Phys.*, 62(4):1544–1555, 1975.

[140] G. Hertzberg. *Molecular Spectra and Molecular Structure.* D. Van Nostrand Company, 1955.

[141] R. J. Le Roy, R. G. Macdonald, and G. Burns. Diatom Potential Curves and Transition Moment Functions from Continuum Absorption Coefficients: Br_2. *J. Chem. Phys.*, 65(4):1485–1500, 1976.

[142] B. H. Bransden and C. J. Joachain. *Introduction to Quantum Mechanics.* Longman Scientific & Technical, 1989.

[143] N. A. Abul-Haj and D. F. Kelley. Geminate Recombination and Relaxation of Molecular Iodine. *J. Chem. Phys.*, 84(3):1335–1344, 1986.

[144] D. L. Bunker and B. S. Jacobson. Photolytic Cage Effect. Monte Carlo Experiments. *J. Am. Chem. Soc.*, 94:1843–1848, 1972.

[145] J.-C. Soetens, G. Jansen, and C. Millot. Molecular Dynamics Simulation of Liquid CCl_4 with a New Polarizable Potential Model. *Mol. Phys.*, 96(7):1003–1012, 1999.

[146] D. J. Nesbitt and J. T. Hynes. Vibrational-Translational Energy Transfer from Highly Excited Anharmonic Oscillators. *Chem. Phys. Lett.*, 82(2):252–254, 1981.

[147] D. J. Nesbitt and J. T. Hynes. Slow Vibrational Relaxation in Picosecond Iodine Recombination in Liquids. *J. Chem. Phys.*, 77(4):2130–2143, 1982.

[148] E. M. Duffy, D. L. Severance, and W. L. Jorgensen. Solvent Effects on the Barrier to Isomerization for a Tertiary Amide from Ab Initio and Monte Carlo Calculations. *J. Am. Chem. Soc.*, 114(19):7535–7542, 1992.

[149] A. J. Stace and J. N. Murrell. Molecular Dynamics and Chemical Reactivity: A Computer Study of Iodine Atom Recombination under High Pressure Conditions. *Mol. Phys.*, 33(1):1–24, 1977.

[150] J. Tellinghuisen. Potentials for Weakly Bound States in I_2 from Diffuse Spectra and Predissociation Data. *J. Chem. Phys.*, 82(9):4012–4016, 1985.

[151] Q. Kong, J. H. Lee, M. L. Russo, T. K. Kim, M. Lorenc, M. Cammarata, S. Bratos, T. Buslaps, V. Honkimaki, H. Ihee, and M. Wulff. Photolysis of Br_2 in CCl_4 Studied by Time-Resolved X-Ray Scattering. *Acta Cryst.*, A66:252–260, 2010.

[152] R. P. Feynman. *Statistical Mechanics.* Addison-Wesley Publishing Company, 1972.

[153] J. Lindner, P. Vöhringer, M. S. Pshenichnikov, D. Cringus, D. A. Wiersma, and M. Mostovoy. Vibrational Relaxation of Pure Liquid Water. *Chem. Phys. Lett.*, 421:329–333, 2006.

[154] B. J. Gertner, R. M. Whitnell, K. R. Wilson, and J. T. Hynes. Activation to the Transition State: Reactant and Solvent Energy Flow for a Model S_N2 Reaction in Water. *J. Am. Chem. Soc.*, 113(1):74–87, 1991.

[155] C. Heidelbach, J. Schroeder, D. Schwarzer, and V. S. Vikhrenko. Mode Specificity of Vibrational Energy Relaxation of Azulene in CO_2 at Low and High Density. *Chem. Phys. Lett.*, 291:333–340, 1998.

[156] V. S. Vikhrenko, C. Heidelbach, D. Schwarzer, V. B. Nemtsov, and J. Schroeder. Molecular Dynamics Simulation of Vibrational Energy Relaxation of Highly Excited Molecules in Fluids. I. General Considerations. *J. Chem. Phys.*, 110(11):5273–5285, 1999.

[157] A. Kandratsenka, J. Schroeder, D. Schwarzer, and V. S. Vikhrenko. Nonequilibrium Molecular Dynamics Simulations of Vibrational Energy Relaxation of HOD in D_2O. *J. Chem. Phys.*, 130:174507, 2009.

[158] T. Yagasaki and S. Saito. Ultrafast Intermolecular Dynamics of Liquid Water: A Theoretical Study on Two-Dimensional Infrared Spectroscopy. *J. Chem. Phys.*, 128:154521, 2008.

[159] T. Yagasaki, J. Ono, and S. Saito. Ultrafast Energy Relaxation and Anisotropy Decay of the Librational Motion in Liquid Water: A Molecular Dynamics Study. *J. Chem. Phys.*, 131:164511, 2009.

[160] T. Yagasaki and S. Saito. Molecular Dynamics Simulation of Nonlinear Spectroscopies of Intermolecular Motions in Liquid Water. *Accounts Chem. Res.*, 42(9):1250–1258, 2009.

[161] T. Yagasaki and S. Saito. A Novel Method for Analyzing Energy Relaxation in Condensed Phases using Nonequilibrium Molecular Dynamics Simulations: Application to the Energy Relaxation of Intermolecular Motions in Liquid Water. *J. Chem. Phys.*, 134:184503, 2011.

[162] J. B. Marion and S. T. Thornton. *Classical Dynamics of Particles and Systems.* Harcourt Brace Jovanovich, 1988.

[163] H. Goldstein, C. Poole, and J. Safko. *Classical Mechanics.* Addison Wesley, 2002.

[164] D. A. McQuarrie. *Mathmatical Methods for Scientists and Engineers.* University Science Books, 2003.

[165] H. J. C. Berendsen, J. R. Grigera, and T. P. Straatsma. The Missing Term in Effective Pair Potentials. *J. Phys. Chem.*, 91(24):6269–6271, 1987.

[166] G. S. Kell. Density, Thermal Expansivity, and Compressibility of Liquid Water from 0°C to 150°C: Correlations and Tables for Atmospheric Pressure and Saturation Reviewed and Expressed on 1968 Temperature Scale. *J. Chem. Eng. Data*, 20(1):97–105, 1975.

[167] M. Abramowitz and I. A. Stegun. *Handbook of Mathematical Functions.* Dover Publications, 1972.

[168] Y. Maréchal. The Molecular Structure of Liquid Water Delivered by Absorption Spectroscopy in the Whole IR Region Completed with Thermodynamics dDta. *J. Mol. Struct.*, 1004:146–155, 2011.